Assessing aViation emission Impact on local Air quality at airports: TOwards Regulation - AVIATOR

Grant Agreement number: 814801

D5.3

Parameterizations of physical exhaust dynamics and comparison between model results and measurements

Delivery Date:	April 2021 (M22)	Start date of project:	01/06/2019
Date of submission:	July 2023 (M49)	Duration:	36+12 months

LEAD BENEFICIARY FOR THIS DELIVERABLE	
Name:	ONERA
Contact Person:	Dr. Etienne Terrenoire
Address:	ONERA - Université Paris Saclay - 8, Chemin de la Hunière - F-91123 Palaiseau
Phone:	+33 1 80 38 60 33
E-mail:	etienne.terrenoire@onera.fr

Authors:	Mathieu Muller, Ulf Janicke, Etienne Terrenoire		
Participants:	ONERA, JC		
Work Package:	WP5		
Dissemination level:	PU (public access)	Nature:	Report
Version:	1.0	Number of Pages:	84

This project has received funding from the European Union's Horizon 2020 research and innovation programme under Grant Agreement No 814801.

REVIEWED AND SIGNED OFF BY			
ROLE	DATE	NAME	SIGNATURE
DELIVERABLE LEADER	July 2023	Mathieu Muller	
WP LEADER	July 2023	Etienne Terrenoire	
PROJECT DIRECTOR	July 2023	Jesús Javier Fernández Orío	FERNANDEZ ORIO JESUS JAVIER | 02527272D Firmado digitalmente por FERNANDEZ ORIO JESUS JAVIER | 02527272D Fecha: 2023.07.21 11:19:23 +02'00'

REVISION HISTORY			
VERSION	DATE	AUTHOR / REVIEWER	NOTES
1.0	10/11/21	Mathieu Muller	First draft
1.1	02/05/21	Mathieu Muller	Second draft
1.2	24/05/21	Mathieu Muller/Ulf Janicke /Etienne Terrenoire	Minor revision
1.3	14/07/23	Etienne Terrenoire	Final version

EXECUTIVE SUMMARY

This deliverable provides simulations of a single aircraft engine's plume dynamics using the CFD code CEDRE (PART 1) and the LASPORT code (part 2). In PART 1, an introduction to CEDRE is first proposed and the model setup is then described. Secondly, a description of the specific meshing adaptation methodology used for the simulations, the strategy to proceed simulations is detailed and the results are compared to measurements collected during the experimental campaign that took place in Ciudad Real in the summer 2021. Two main configurations are simulated including a single modern Trent engine at rest using four different thrusts and a full aircraft architecture during landing and take-off phases. Finally, an enhanced parametrisation for the wingtip vortices descent is described for LASPORT based on the CEDRE results. Part 2 details the simulations performed using the air quality model LASPORT. The model is first briefly introduced and secondly the modelled results are presented and compared with both the experimental data sets and finally the CEDRE outputs.

TABLE OF CONTENTS

LIST OF TABLES

LIST OF FIGURES

LIST OF ABBREVIATIONS

In this deliverable, a number of abbreviations are used.

C1	Modern Trent engine without the plane configuration
C2	A350 with 2 modern Trent engines in landing configuration
C3	A350 with 2 modern Trent engines in climbing configuration
CAD	Computer-Aided Design
CEDRE	Calculs d'Ecoulements Diphasiques Réactifs pour l'Energétique
CFD	Computational Fluid Dynamics
ICAO	International Civil Aviation Organization

LIST OF SYMBOLS

Symbol	Commentary	Unit
α	Thermal diffusivity	m^2/s
α_{aa}	Angle of attack	rad
α_r	Temperature exponent in Arrhenius law	
Γ	Circulation	m^2/s
δ	Kronecker delta	
μ	Dynamical viscosity	kg/m/s
ρ	Density	kg/m^3
ρ_a	Ambient density	kg/m^3
τ	Dilution	
ϕ	Ratio of specific thrusts	
ψ	Bypass Ratio	
ω	Specific rate of dissipation	s^{-1}
$\vec{\omega}$	Vortex vector	s^{-1}
$\dot{\omega}_k$	mass transfer rate of the kth species	$kg/m^3/s$
A	Area	m^2
A_r	Pre-exponential factor in Arrhenius law	cm^3/s
b	Span of the aircraft	m
c	Complexity used for adaptation process	
c_p	Gas mixture specific heat capacity at constant pressure	J/K
D_k	Diffusion	m^2/s
e_t	Gas mixture total energy	J/kg
F	Thrust	kN
F_{max}	Maximum Thrust	kN
g	Gravity constant	m/s^2
h_t	Gas mixture total enthalpy	J/kg
i	Index for the momentum equation component	
j	Index used to specify the component	
k	Index for the species	
K	Turbulent kinetic energy	m^2/s^2
K_a	Ambient turbulent kinetic energy	m^2/s^2
k_f	Forward rate constant	cm^3/s

L_x	Length of the outer box	m
L_y	Width of the outer box	m
L_z	Height of the outer box	m
M	Mach number	
$\dot{m}$	Mass flow	kg/s
$m_{aircraft}$	Aircraft mass	kg
n	Exponent of the dilution law	
p	Pressure	Pa
P_a	Ambient pressure	Pa
P_k	Partial pressure of the species k	Pa
R	Universal gas constant	J/K/mol
RH	Relative Humidity	
S^d	Deviator strain-rate tensor	s^{-1}
t	Time	s
T	Static temperature	K
T_a	Ambient temperature	K
T_r	Relative temperature	
T^{tot}	Total temperature	K
u	Velocity	m/s
u_0	Head speed	m/s
V_a	Ambient velocity	m/s
V_r	Relative velocity	
V_s	Secondary velocity	m/s
V_t	Velocity used as adaptation parameter	m/s
x	Axial direction	m
X_k	Molar Fraction of the kth species	
y	Transverse direction	m
Y_k	Mass Fraction of the kth species	
z	Vertical direction	m

PARAMETERIZATIONS OF PHYSICAL EXHAUST DYNAMICS AND COMPARISON BETWEEN MODEL RESULTS AND MEASUREMENTS

1. Introduction

Modelling the dispersion of aircraft engine exhaust plumes provides a crucial basis for a local air quality assessment both spatially and temporally. This is an essential complement to measurements which are restricted to relatively few locations and which do not allow the assessment of future trends. In this deliverable specific attention is given to the chemistry and microphysics as well as the dynamics of the engine exhaust plume. These will be address using two different models: CEDRE (PART 1) and LASPORT (PART 2). They will provide an enhanced understanding of processes, which are crucial for describing the impact of aircraft exhaust emissions on air quality in and around airports. Finally, a comprehensive comparison of the modelling results with the AVIATOR measurement campaigns (WP 3 and 4) is presented and discussed.

PART 1: CFD MODELLING USING CEDRE

1. Methodology

1.1. Computational Fluid Dynamics

To simulate the jet behind the modern Trent engine, 3D simulations are carried out using the compressible Navier-Stokes solver with multi-species CHARME integrated in the CEDRE numerical code. This code is using numerical methods based on cell-centered finite-volume approach on unstructured grids.

1.1.1. Fluid flow model

The differential Navier-Stokes equations used in CEDRE 0 are the k mass conservation equations, the 3 momentum conservation equations and the energy conservation equation:

$$\frac{\partial}{\partial t}(\bar{\rho}\tilde{Y}_k) + \frac{\partial}{\partial x_j}(\bar{\rho}\tilde{u}_j\tilde{Y}_k) = \frac{\partial}{\partial x_j}\left(\bar{\rho}D_k\frac{\partial\tilde{Y}_k}{\partial x_j} - \widetilde{\bar{\rho}u_j''Y_k''}\right) + \bar{\dot{\omega}}_k, \quad (1)$$

$$\frac{\partial}{\partial t}(\bar{\rho}\tilde{u}_i) + \frac{\partial}{\partial x_j}(\bar{\rho}\tilde{u}_j\tilde{u}_i) = -\frac{\partial\bar{p}}{\partial x_i} - \bar{\rho}g\delta_{i3} + \frac{\partial}{\partial x_j}(\mu\widetilde{S_{ij}^d} - \widetilde{\bar{\rho}u_j''u_i''}), \quad (2)$$

$$\frac{\partial}{\partial t}(\bar{\rho}\tilde{e}_t) + \frac{\partial}{\partial x_j}(\bar{\rho}\tilde{u}_j\tilde{h}_t) = \frac{\partial}{\partial x_j}\left(\bar{\rho}c_p\alpha\frac{\partial\bar{T}}{\partial x_j} + \sum_k\left(\bar{\rho}\tilde{h}_tD_k\frac{\partial\tilde{Y}_k}{\partial x_j} - \bar{\rho}\tilde{h}_t\widetilde{u_j''Y_k''}\right) - \widetilde{\bar{\rho}u_j''T''} + 2\mu\widetilde{S_{ij}^d} - \widetilde{\bar{\rho}u_j''u_i''}\tilde{u}_i\right), \quad (3)$$

with ρ the density, Y_k the mass fraction of the kth species , u the velocity, x the coordinates, D_k the diffusion coefficient for the kth species in the gas mixture, $\dot{\omega}_k$ their mass transfer rate, p the pressure, g the gravity, δ the kronecher symbol, μ the dynamical viscosity of the gas mixture, S^d the deviator strain-rate tensor, e_t the gas mixture total energy, h_t the gas mixture total enthalpy, c_p the gas mixture specific heat capacity at constant pressure, α the thermal diffusivity

and T the gas mixture static temperature. The index j is used to specify the components, i to characterize the momentum equation component, and k to identify the species. The Favre average, corresponding to a density-weighted and time average decomposition, is used in those equations. All variables Φ are thus decomposed in a mean part $\overline{\Phi}$ and a fluctuating part Φ'':

$$\Phi = \widetilde{\Phi} + \Phi'', \tag{4}$$

with $\widetilde{\Phi} = \frac{\overline{\rho\Phi}}{\overline{\rho}}$.

In both momentum and energy equations, the Reynolds stress tensor $\widetilde{u_j'' u_i''}$ appears and needs to be modeled. In this study, the Boussinesq hypothesis and the two-equations $K - \omega$ with SST correction from Menter [2][3] are used to calculate the Reynolds stress tensor.

1.1.2. Gas phase chemistry

A gas-phase reaction scheme based on [4][5] and already used in previous studies [6][7][8][9] is implemented in CEDRE. This scheme, resumed in Table 1, consists of 23 species and 60 reactions, including NO_x, SO_x, and HO_x chemistry, which is important to characterize the air quality. Each reaction follows the Arrhenius equation in which the forward rate constant k_f by:

$$k_f = A_r \left(\frac{T}{T_{ref}}\right)^{\alpha_r} \exp\left(-\frac{T_{act}}{T}\right), \tag{5}$$

with A_r the pre-exponential factor, α_r the temperature exponent, T_{act} the activation temperature, T_{ref} the reference temperature. In Table 1, the values presented correspond to a reference temperature of 298 K and M in the reactions corresponds to a third component. It is important to note that for reactions 42 to 60, an equivalent Arrhenius law is derived from the Troe laws presented in [4] in which a third component M is needed.

Table 1. Gas-phase reaction scheme

n°	Reaction	A_r(cm³/s)	α_r	T_{act} (K)
1	$O + O_3 = 2O_2$	1.21E-11	0	2125
2	$H + O_3 = OH + O_2$	1.15E-10	0	436
3	$H + OH = O + H_2$	6.86E-14	2.8	1950
4	$H + HO_2 = OH + OH$	2.80E-10	0	440
5	$H + HO_2 = H_2 + O_2$	6.90E-11	0	636.9
6	$H + HO_2 = H_2O + O$	3.85E-11	0.46	677.9
7	$OH + O = H + O_2$	1.83E-11	0	-173.3
8	$OH + O_3 = HO_2 + O_2$	1.90E-12	0	1000
9	$OH + H_2 = H_2O + H$	1.27E-12	1.64	1589
10	$OH + OH = H_2O + O$	5.39E-13	1.54	-355.7
11	$OH + HO_2 = H_2O + O_2$	5.09E-11	0	-72.6
12	$OH + H_2O_2 = H_2O + HO_2$	3.10E-12	0.47	179.8
13	$HO_2 + O = OH + O_2$	2.71E-11	0	224
14	$HO_2 + O_3 = OH + 2O_2$	1.40E-14	0	600
15	$HO_2 + HO_2 = H_2O_2 + O_2$	2.20E-13	0	-600

16	$H_2O_2 + O = OH + HO_2$	2.33E-11	0	2814
17	$H_2O_2 + H = OH + H_2O$	1.70E-11	0	1800
18	$H_2O_2 + H = HO_2 + H_2$	1.77E-11	0	2890
19	$NO + O_3 = NO_2 + O_2$	2.14E-12	0	1408
20	$NO + HO_2 = NO_2 + OH$	3.70E-12	0	-240
21	$NO + NO_3 = NO_2 + NO_2$	1.80E-11	0	-110
22	$NO_2 + O = NO + O_2$	6.50E-12	0	-120
23	$NO_2 + O_3 = NO_3 + O_2$	1.20E-13	0	2450
24	$H + NO_2 = OH + NO$	1.40E-10	0	0
25	$NO_2 + NO_3 = NO + O_2 + NO_2$	1.91E-13	0	1696
26	$NO_3 + O = NO_2 + O_2$	1.00E-11	0	0
27	$OH + NO_3 = HO_2 + NO_2$	2.30E-11	0	0
28	$HNO_2 + O = OH + NO_2$	2.00E-11	0	3000
29	$HNO_2 + H = NO_2 + H_2$	2.00E-11	0	3700
30	$HNO_2 + OH = H_2O + NO_3$	1.80E-11	0	390
31	$HNO_3 + O = OH + NO_3$	3.00E-17	0	0
32	$HNO_3 + OH = H_2O + NO_3$	4.02E-14	0	-317.7
33	$SO + O_2 = SO_2 + O$	1.55E-13	0	2288
34	$SO + O_3 = SO_2 + O_2$	4.30E-12	0	1148
35	$SO + OH = SO_2 + H$	8.59E-11	0	0
36	$SO + NO_2 = SO_2 + NO$	1.40E-11	0	0
37	$SO_2 + O3 = O2 + SO_3$	3.00E-12	0	7000
38	$SO_3 + O = O2 + SO_2$	3.17E-11	0	4455
39	$SO_3 + H_2O = H_2SO_4$	1.20E-15	0	0
40	$HSO_3 + O_2 = HO_2 + SO_3$	1.23E-12	0	316.8
41	$CO + OH = CO_2 + H$	1.18E-13	0.98	-94
42	$O + O = O_2$	5.20E-35	0	-900
43	$O + O_2 = O_3$	4.09E-12	-0.0442129	188.154
44	$H + O = OH$	4.36E-32	-1	0
45	$H + O_2 = HO_2$	7.22E-11	-0.0111266	0.132145
46	$H + H = H_2$	2.16E-07	-1.48184	189.417
47	$H + OH = H_2O$	2.63E-10	-0.0172568	76.153
48	$OH + OH = H_2O_2$	1.48E-11	-0.00236827	0.125168
49	$HO_2 + HO_2 = H_2O_2 + O_2$	2.00E-13	-0.00621038	-602.83
50	$NO + O = NO_2$	2.94E-11	0.284489	1.92499

51	$OH + NO = HNO_2$	5.04E-12	-0.00630535	-159.181
52	$NO_2 + O = NO_3$	2.62E-11	-0.0198225	29.769
53	$OH + NO_2 = HNO_3$	1.83E-12	-0.00987939	-584.496
54	$NO_2 + NO_3 = N_2O_5$	1.99E-12	0.191491	1.18797
55	$N_2O_5 = NO_2 + NO_3$	9.71E-07	-9.74E-05	9369.78
56	$HNO_2 = OH + NO$	1.79E-02	-1.24028	25012.15
57	$HNO_3 = OH + NO_2$	3.51E-03	-0.0100234	24269.7
58	$SO_2 + O = SO_3$	1.63E-09	-0.264953	184.637
59	$SO_2 + OH = HSO_3$	1.97E-12	-0.00258083	-0.77504
60	$CO + O = CO_2$	2.60E-14	0.00486928	1456.92

1.2. Mesh adaptation procedure

The aim of this study is to investigate the aerodynamics and chemistry in the plume behind a modern Trent engine. Taking into account many processes of different characteristic length and time in thus needed, which implies a mesh adapted to the case simulated by CFD. To avoid large computational time, the mesh needs to be optimised: refined in the area of interests, where detailed physical must be captured and coarse elsewhere. To distinguish those zones, a mesh adaptation technique using Feflo.a [10] is performed. This software uses a surface and volume anisotropic re-meshing based on a prescribed Riemannian metric field. The mesh adaptation aims to reduce the interpolation error in the field, which means the difference between calculated and exact solutions. The algorithm for steady simulations is described by the following steps:

1. Discretization of the field by generating an initial coarse mesh ;
2. Computation of the flow field on the mesh ;
3. Estimation of the metric-based error ;
4. Modification of the mesh with respect to these metric fields ;
5. Projection of the surface mesh onto the true geometry using the CAD data ;
6. Interpolation of the flow solution on the new adapted mesh ;
7. Go back to step 2.

2. Configuration 1: Modern Trent engine

2.1. Engine configuration

To study the hot and turbulent exhaust of aircraft engines, a realistic configuration is needed. A modern Trent engine CAD is presented on the Figure 1. For this configuration, the aim is to study the plume behind the engine for a plane at rest. Therefore, the CAD of the whole plane is then not needed. The CAD contains the engine linked by a pylon to a part of the wing from the Airbus A350. It is interesting to note that the bypass nozzle contains two vertical structures which can have an impact on the exhaust flow.

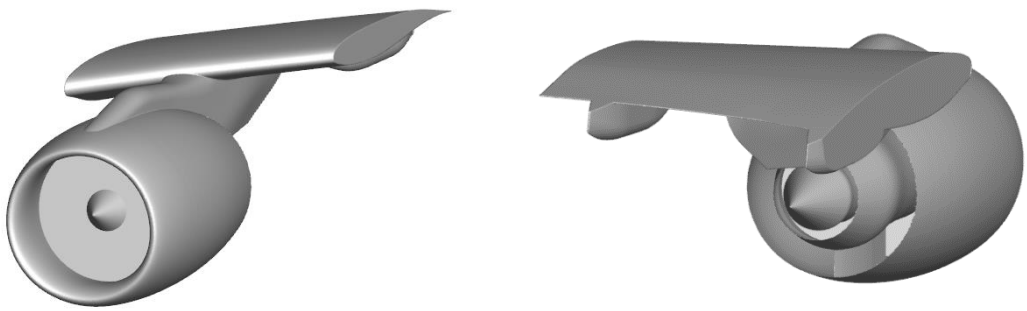

Figure 1. CAD of the modern Trent engine

2.2. Computational domain

The computational domain is defined by a box containing the engine geometry. To limit the effects of the boundary on the flow, the boundaries of the box are set far from the engine. The extension of the domain is around 10 spans before and on each side of the engine and 20 spans behind the engine. The engine is 2 m above the ground and the height of the box is set to 20 spans. The Table 2 presents the computational domain dimensions for the simulations carried out for this configuration. The span b of the corresponding plane is close to 58 m.

Table 2. Computational domain dimensions

L_x	$[-10b, 20b]$
L_y	$[-10b, 10b]$
L_z	$[0, 20b]$

2.3. Boundary conditions

A reference case is defined for the ambient atmosphere: $T_a = 288.15\ \mathrm{K}$, $P_a = 101325\ \mathrm{Pa}$. The wind velocity is set to $3\ \mathrm{m/s}$ to avoid instabilities during the CFD simulation. The Table 3 sums up the boundary conditions imposed in the limit of the computational domains. Slip conditions are imposed on the side and the top of the box. Pressure condition is imposed at the outlet. Temperature and velocity conditions are imposed at the inlet, and the ground is a wall condition.

Table 3. Computational domain dimensions

Boundary	Position	Condition
Inlet	$x = -10b$	Velocity and temperature imposed
Outlet	$x = 20b$	Pressure imposed
Left	$y = -10b$	Slip
Right	$y = 10b$	Slip
Ground	$z = 0b$	Wall
Top	$z = 20b$	Slip

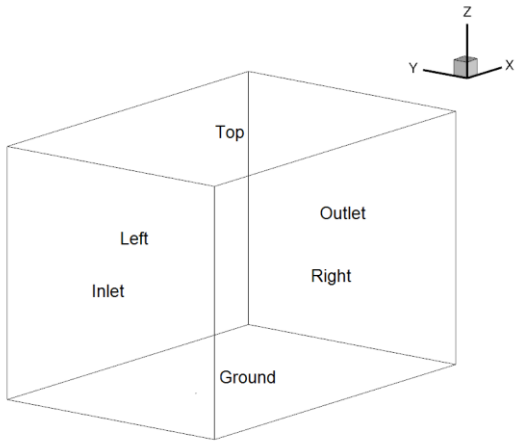

Figure 2. Boundary conditions for computational domain

For the engine, a wall condition is imposed except for the fan entry for which a pressure condition is applied and for the bypass and core exits for which a total temperature and surface mass flow are applied. The Figure 3 illustrates the boundary conditions for the engine.

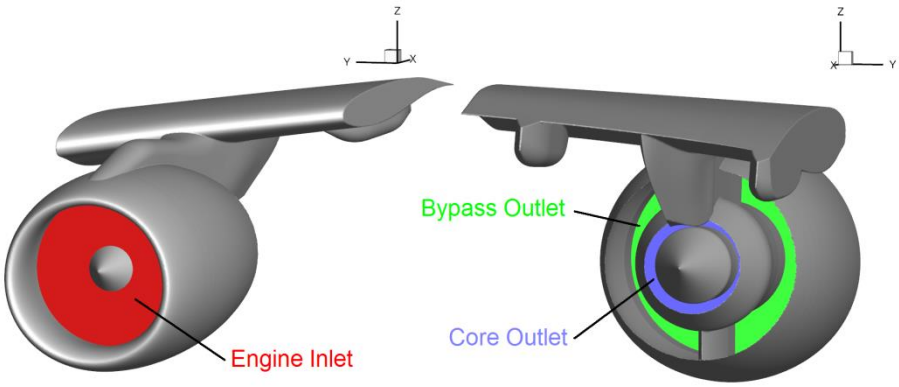

Figure 3. Boundary conditions for the engine

The Table 4 describes the initial conditions for the gas species in mass fraction for the ambient air and the core outlet. For the bypass outlet, same conditions of gas species are specified than for the ambient air. For the core, the mass fractions are taken from [7][11]. For the species in the ambient atmosphere and at the bypass outlet, mean values of molar fractions and associated references are summarized in the Table 4.

Table 4. Gas species composition as molar fractions at core exit and in ambient atmosphere

k	Molecular Name	Exhaust Core	Ambient Air	References for species in ambient air
1	O	0.00	0.00	/
2	O_2	0.135	0.21	/
3	O_3	0.00	$4.0\ 10^{-8}$	[12][13][14][15][16][17]
4	H	0.00	0.00	/
5	H_2	0.00	$5.0\ 10^{-10}$	[18]
6	OH	$1.0\ 10^{-5}$	$1.0\ 10^{-13}$	[19][20][21]
7	HO_2	0.00	$1.0\ 10^{-11}$	[20]
8	H_2O	$3.5\ 10^{-2}$	$7.5\ 10^{-3}$	/

9	H_2O_2	0.00	$5.0\ 10^{-10}$	[22]
10	NO	$6.6\ 10^{-5}$	$1.0\ 10^{-8}$	[14][16]
11	NO_2	$6.6\ 10^{-6}$	$2.0\ 10^{-8}$	[13][14][16][17]
12	NO_3	0.00	$1.0\ 10^{-11}$	[12][13][14]
13	N_2O_5	0.00	$5.0\ 10^{-10}$	[13]
14	HNO_2	0.00	0.00	/
15	HNO_3	0.00	$1.0\ 10^{-9}$	[15]
16	CO	$2.96\ 10^{-5}$	$1.0\ 10^{-5}$	[23]
17	CO_2	$3.14\ 10^{-2}$	$4.0\ 10^{-4}$	[24]
18	SO	0.00	0.00	/
19	SO_2	$5.8\ 10^{-6}$	$1.0\ 10^{-8}$	[15][17]
20	SO_3	0.00	0.00	/
21	HSO_3	0.00	0.00	/
22	HSO_4	0.00	0.00	/
23	N_2	$1-\sum_{k=1}^{22} X_k$	$1-\sum_{k=1}^{22} X_k$	/

2.4. Results

2.4.1. Grid mesh optimization

In this section, the different steps of the grid mesh optimization are presented to show the progressive refinement of the mesh in the plume. In previous studies [6][8][9], the parameter V_s used for optimization is defined by:

$$V_s = \sqrt{V_y^2 + V_z^2}, \tag{6}$$

With V_y and V_z the velocity components in the plan orthogonal to the aircraft trajectory. This parameter seems promising for capturing the jet/vortex interaction but inappropriate for this configuration. Indeed, as the engine is not moving and no wing tip vortex is therefore generated. To characterize the plume of an engine without upwind velocity, the parameter must take into account V_x. A new parameter is proposed in this study to generalize the mesh adaptation for the three configurations. This parameter is defined by:

$$V_t = \sqrt{\sum_j \left(V_j - V_{j,a}\right)^2 + \max(|K - K_a|, K_a)}, \tag{7}$$

with $V_{j,a}$ the j component of the upwind velocity and K_a the turbulent kinetic energy of the ambient atmosphere. This parameter takes into account two terms. The first one characterizes the velocity regarding the upwind flow. The second measures the impact of the turbulent kinetic energy in the plume compared to the ambient one.

The grid mesh optimization is stopped when the simulation results do not depend on the mesh refinement. On the Table 5 are resumed the mesh characteristics for each step of the mesh adaptation for the 7% thrust case.

Table 5. Grid mesh characteristics for the 7% thrust case

Grid Mesh	Number of tetrahedrons
1	7,746,308
2	3,082,375
3	3,225,822
4	3,310,601
5	3,368,440

As an example, the Figure 6 illustrates lateral cuts for each step for the case of a 7 % thrust engine. After the first step, the mesh is refined in the region of the plume and is coarse elsewhere, particularly at the box boundaries, resulting to a decrease of the number of tetrahedrons. Each following step modifies behind the engine the repartition of the tetrahedrons and increases slightly their number. The mesh in the plume close to the engine is more and more detailed each time a mesh optimization is realised. After four steps, the mesh seems converged which can be verified by extracting datas from the field.

a)

b)

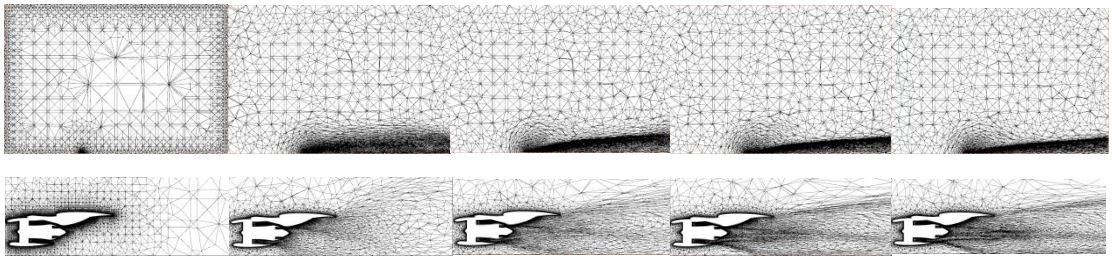

Figure 4. Side cut of meshes 1 to 5 (left to right) for the 7% thrust case: (a) global mesh; (b) zoom on the engine

Figure 5 presents the axial profiles of relative temperature T_r and relative velocity V_r for each mesh, defined by:

$$T_r = \frac{T - T_a}{T_{max} - T_a} \; ; \; V_r = \frac{\|\vec{V}\| - \|\vec{V_a}\|}{\|\vec{V}\|_{max} - \|\vec{V_a}\|},$$

with $T_a = 288.15$ K and $\|\vec{V_a}\| = 3$ m/s for this configuration. The index max refers to the maximal value along the extracted streamlines from the CFD simulation. The axial origin is put just behind the nozzle. For both parameters, the profiles are quasi identical when extracted from simulations with the meshes 4 and 5. The conclusion of this study is that there is no need to pursue the mesh optimization after three steps. For all other cases presented in this section, three steps of mesh adaptation are realized, which is enough even for the 100 % thrust case, as illustrated in the Figure 6, where the meshes 4 and 5 are equivalent.

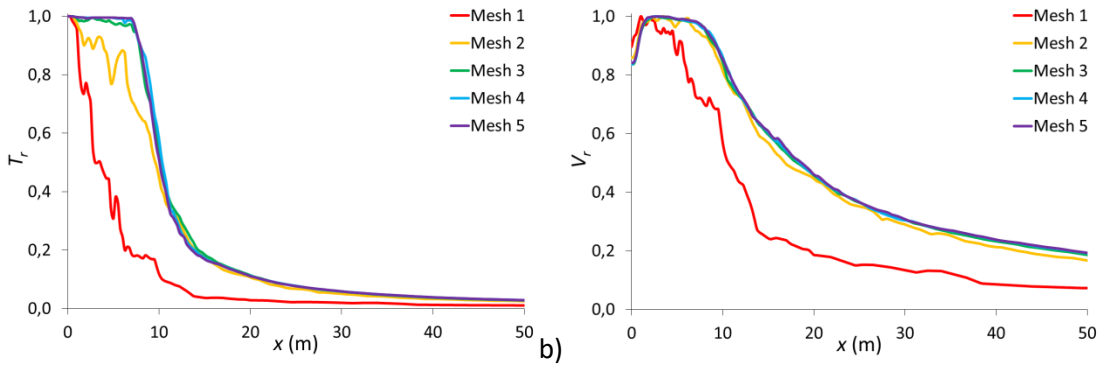

a) b)

Figure 5. Profiles extracted in the center of the plume for the five meshes: (a) relative temperature (*Tr*) and (b) relative velocity (*Vr*)

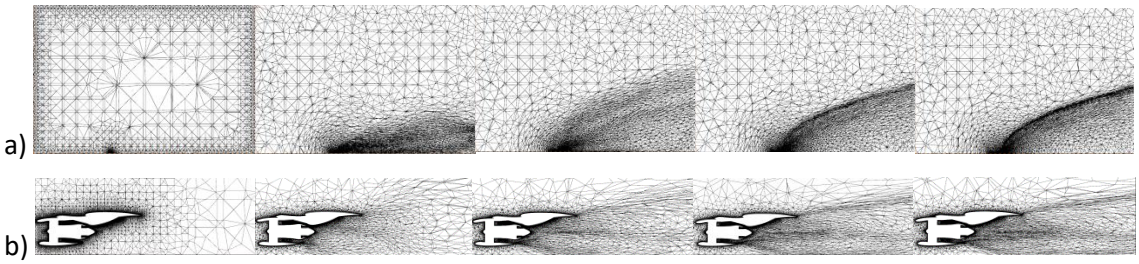

Figure 6. Side cut of meshes 1 to 5 (left to right) for the 100% thrust case: (a) global mesh; (b) zoom on the engine

2.4.2. Parametric studies

To initialize the CEDRE simulations, boundary conditions for the engine needs to be specified. The modern Trent engine characteristics are obtained from the ICAO database: maximum thrust F_{max} and bypass ratio ψ. The engine geometry is defined directly in the CAD. From this CAD, different areas can be extracted as illustrated in the Figure 7. Those data are resumed in Table 6.

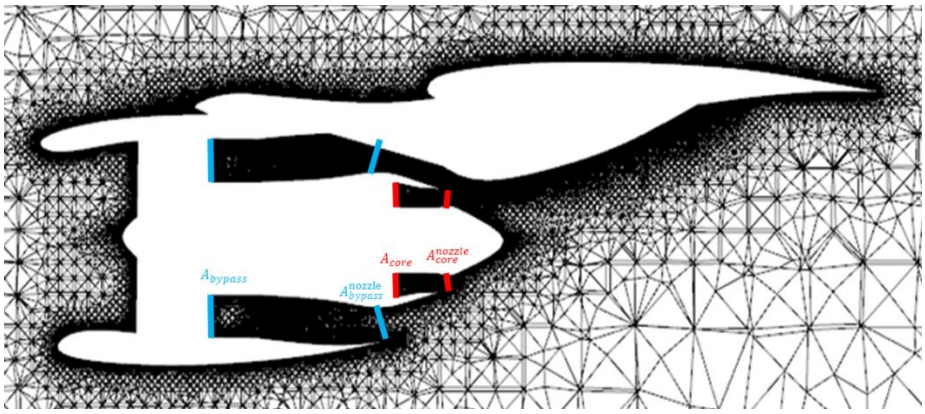

Figure 7. Illustration of the outflow cross sections (m²) used for the study

Table 6. Modern Trent engine characteristics

F_{max} (kN)	ψ	A_{core} (m^2)	A_{bypass} (m^2)	A_{core}^{nozzle} (m^2)	A_{bypass}^{nozzle} (m^2)
436.7	8.1	1.39	4.27	0.65	3.45

The bypass ratio ψ is defined by:

$$\psi = \frac{\dot{m}_{bypass}}{\dot{m}_{core}} = \frac{\rho_{bypass}^{nozzle} u_{bypass}^{nozzle} A_{bypass}^{nozzle}}{\rho_{core}^{nozzle} u_{core}^{nozzle} A_{core}^{nozzle}}, \tag{8}$$

with $\dot{m}$ the mass flow, ρ the density and u the velocity. Assuming ideal expansion in the nozzle, ambient conditions can be assumed for the bypass: $P_{bypass}^{nozzle} = P_a$ and $T_{bypass}^{nozzle} = T_a$. For the core, one can assume the same hypothesis for the pressure: $P_{core}^{nozzle} = P_a$. The temperature at the core nozzle is then directly linked to the temperature at the bypass nozzle using equation (8) and ideal gas law:

$$T_{core}^{nozzle} = \psi \frac{A_{core}^{nozzle}}{A_{bypass}^{nozzle}} \frac{u_{core}^{nozzle}}{u_{bypass}^{nozzle}} T_{bypass}^{nozzle} \tag{9}$$

Neglecting major pressure differences between core flow and environment, the uninstalled thrust is given by:

$$F = F_{bypass} + F_{core} = \dot{m}_{bypass}\left(u_{bypass}^{nozzle} - u_0\right) + \dot{m}_{core}\left(u_{core}^{nozzle} - u_0\right), \quad (10)$$

with the head speed u_0.

The ratio of specific thrust $F_{bypass}/\dot{m}_{bypass}$ over specific thrust $F_{core}/\dot{m}_{core}$ is:

$$\phi = \frac{u_{core}^{nozzle} - u_0}{u_{bypass}^{nozzle} - u_0} \quad (11)$$

The equations (9), (10) and (11) can be used to determine u_{core}^{nozzle}, u_{bypass}^{nozzle} and T_{core}^{nozzle} if the ratio ϕ is known. A parametric study on ϕ is then needed to see its impact on the flow.

2.4.2.1. Study on ϕ

Four values of ϕ have been tested on the adapted mesh for the 100 % thrust case. Total temperature T^{tot} and mass flow $\dot{m}$ for both core and bypass are calculated and used for the initialization of the CEDRE simulation. Those values are summarized in Table 7.

Table 7. Boundary conditions for the engine as a function of ϕ

ϕ	1.0	1.2	1.5	2.0
$\dot{m}_{core}$	159	157	155	151
$\dot{m}_{bypass}$	1288	1274	1254	1223
T_{core}^{tot}	486	592	755	1040
T_{bypass}^{tot}	334	333	332	330

The parameter ϕ has a strong impact on the total temperature at the core. The mass flows at both exits are almost constant, as the total temperature at the bypass. As presented in Table 8, the velocity of the flow at the bypass nozzle is almost constant with ϕ whereas the velocity at the core nozzle increases strongly with ϕ, resulting to a Mach number at the core nozzle close to 1 for $\phi = 2$.

Table 8. Velocities at the nozzles as a function of ϕ

ϕ	1.0	1.2	1.5	2.0
u_{core}^{nozzle}	305	362	444	576
u_{bypass}^{nozzle}	305	301	297	289

The dilution τ, defined by:

$$\tau = \frac{1}{T_r} = \frac{T_{max} - T_a}{T - T_a}, \quad (12)$$

is one of the characteristic parameter of the plume. In the Figure 8 are represented the dilution profiles extracted in the centre of the plume for the four ϕ values. After a transition zone close to the engine ($x < 30$m) and a fast increase of the dilution to $\tau = 10$, a similar trend is observed for all ϕ. The higher ϕ, the higher the dilution τ, which is explained by a higher T_{max}.

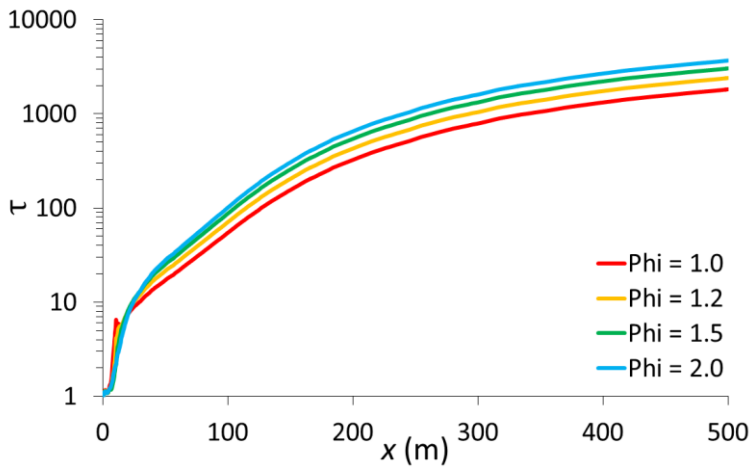

Figure 8. Dilution versus distance behind the engine. Profiles extracted in the center of the plume

Figure 9 represents the temperature (left) and velocity (right) radial profiles at different positions behind the engine (a, b and c) for the four different ϕ. For $x = 0$ m, the temperature is close to ambient except for the zone corresponding to the core, where high temperature is observed. The transition zone between core temperature and ambient temperature is narrow ($\Delta y = 0.2$ m). The velocity profiles present three constant zones: the ambient zone ($|\Delta y| > 1.5$ m), the bypass zone ($0.5\ m < |\Delta y| < 1$ m), and the core zone ($|\Delta y| < 0.5$ m). For $\phi > 1.2$, local maxima are observed corresponding to the core exit. For $x = 20$ m, the radial length of the plume is close to 8 m illustrating its spreading due to convection and diffusion. The maximum velocity is now at the center of the plume and the shape of the profile is close to a Gaussian because of the mixing of bypass and core flows. The velocity profiles are close for all ϕ whereas the impact of this parameter is still apparent on the temperature. For $x = 50$m, the spreading of the plume continues. For the highest ϕ, the temperature in the center of the plume is still 20K higher than the ambient value and the velocity is close to 80 m/s.

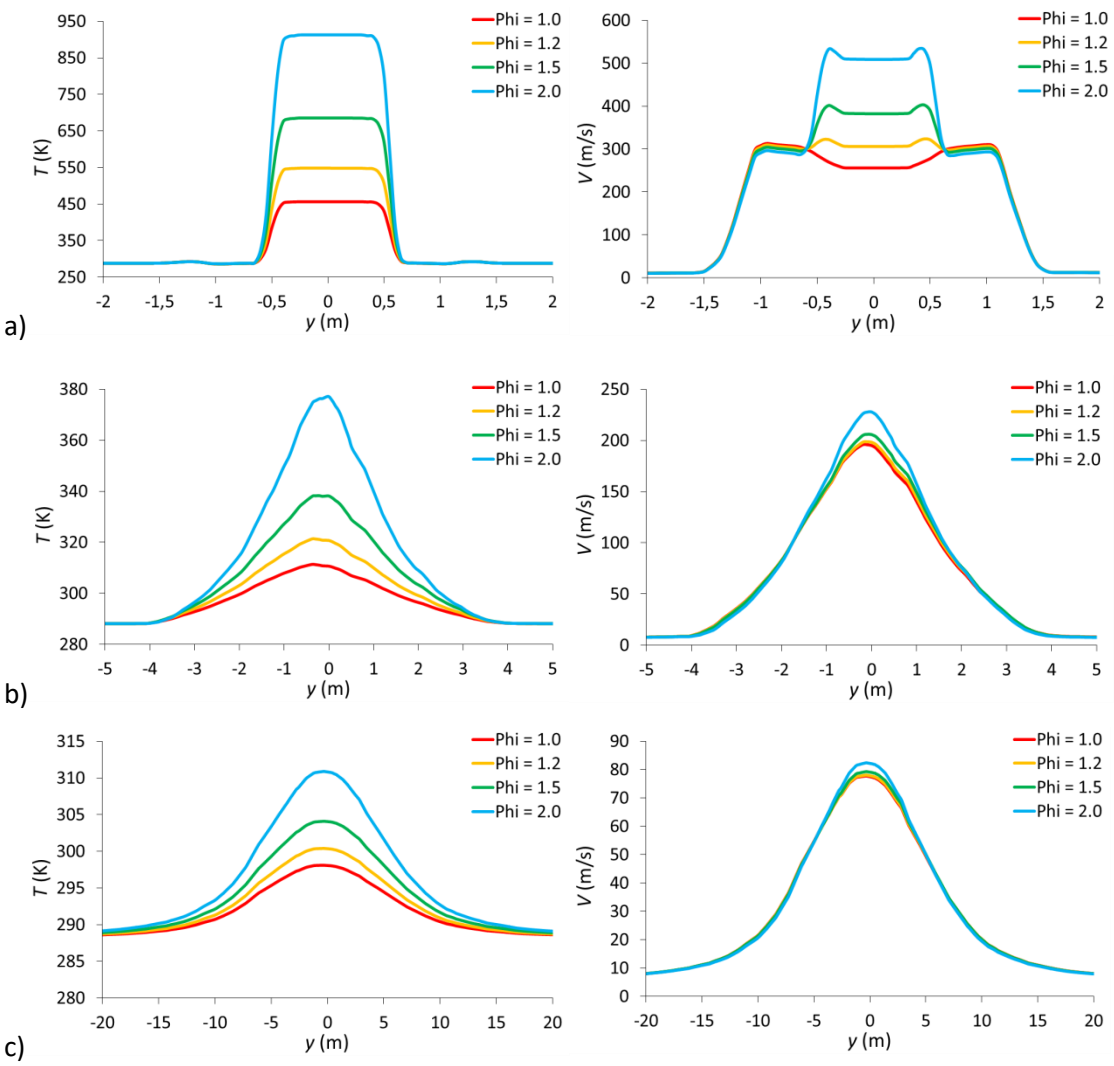

Figure 9. Temperature (left) and velocity (right) radial profiles: (a) $x = 0$ m, (b) $x = 20$ m, (c) $x = 50$ m

The parameter ϕ has a strong effect on the core temperature and velocity, which affects the plume mixing and maximum values. On the other hand, the spreading is not affected by this parameter as the bypass flow is equivalent for all ϕ. To conclude this parametric study, we chose $\phi = 1.5$ because the total temperature for the core corresponds to a value close to the one calculated for a similar engine in Asoliman et al.[25].

2.4.2.2. Study on thrust

Four values of thrust regarding the maximum thrust are tested, corresponding to different regimes of the LTO cycle: idle (7 %), landing (30 %), climbing (85 %) and take-off (100 %). Table 9 summarized the boundary conditions used in CEDRE for the four different regimes.

Table 9. Boundary conditions for the engine as a function of thrust

F/F_{max}	0.07	0.30	0.85	1.00
$\dot{m}_{core}$ (kg/m²/s)	42	85	143	155
$\dot{m}_{bypass}$ (kg/m²/s)	337	690	1157	1254
T_{core}^{tot} (K)	658	685	740	755
T_{bypass}^{tot} (K)	291	301	325	332

2.4.2.3. Aerodynamics

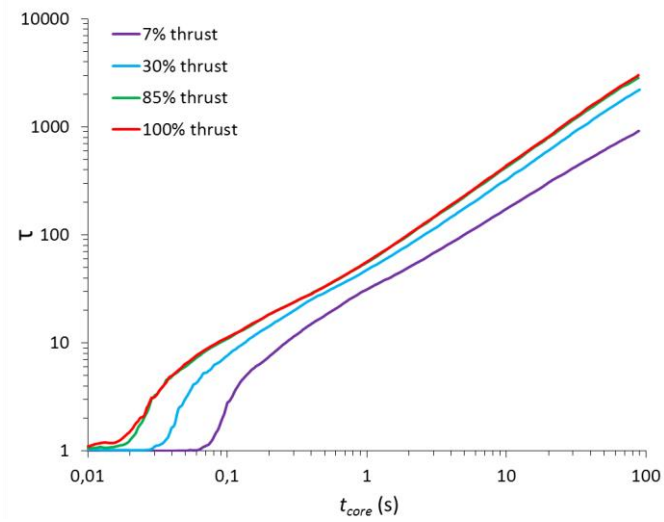

Figure 10. Dilution versus distance behind the engine for the 4 regimes. Profiles extracted in the center of the plume

Figure 10 represents the dilution profiles extracted at the centre of the plume for the four different thrust regimes. The physical time from the point of view of the exhaust flow t_{core} is defined by:

$$t_{core} = \int_0^x \frac{1}{V_{core}(x)} dx. \tag{13}$$

In all cases, 90 s after which the aircraft have passed correspond to a position 500 m behind the same plane. As the flow gets far from the engine, the dilution increases. Three steps can be observed for the evolution of the dilution. First, the dilution remains quasi constant for a short time corresponding to the direct exit of the engine. For higher thrusts, the exit velocity gets higher as the shear stress with the ambient flow. Note that, the duration during which the dilution is constant is shorter as the thrust increases. Then, a fast increase of dilution is observed in all cases and finally, a last zone is observed where the dilution increases as a power of the physical core time:

$$\tau \sim t_{core}^n. \tag{14}$$

with $n \approx 0.74$ for the 7 % thrust case and $n \approx 0.84$ for the other regimes. Finally, the global dilution is higher as the thrust increases.

For strong thrust, the temperature and the velocity at the core nozzle are higher, and the mixing stronger, which is illustrated in Figure 11 where temperature side cut for the four thrusts are presented. For 7 % thrust, the plume is elongated, and a 1 K difference from the ambient temperature is still observed 250 m behind the engine. For stronger thrust, a lower plume length is observed. The plume height increases with the thrust because of a stronger mixing. The same trend is observed for the velocity field (see Figure 12). Interestingly, even at 30 % thrust, the flow around the engine is also accelerated due to strong velocity at the engine exit.

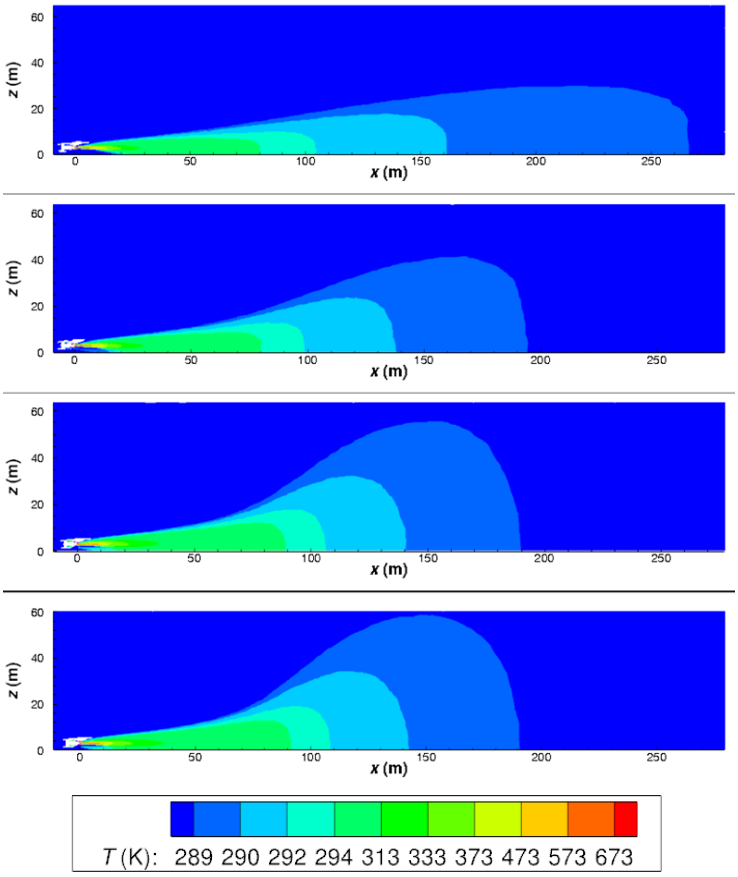

Figure 11. Temperature side cut for the four thrusts. From up to bottom: 7 %, 30 %, 85 % and 100 %

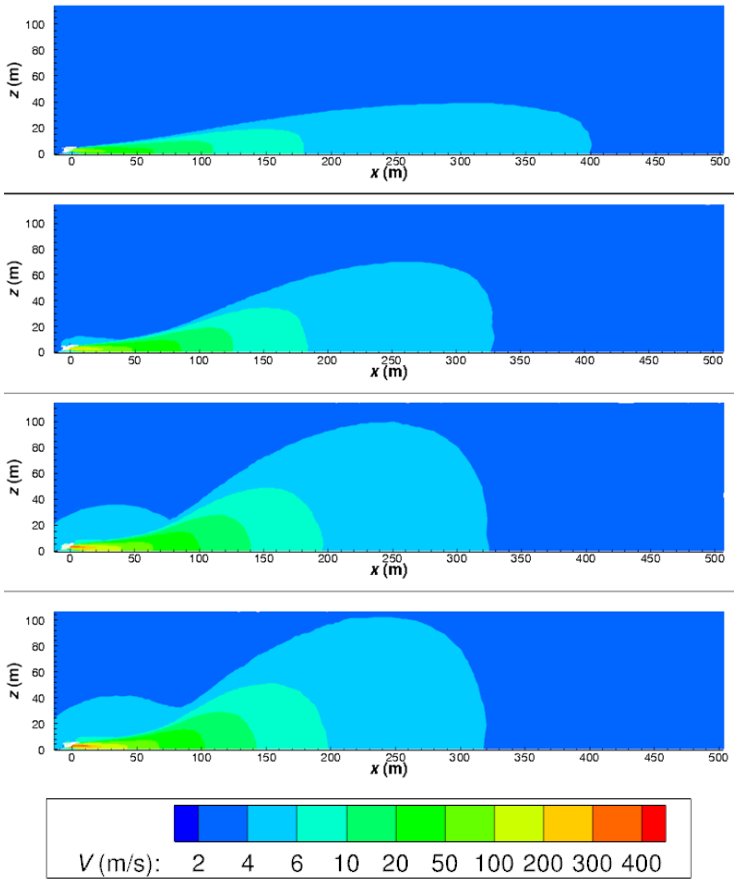

Figure 12. Velocity side cut for the four thrusts. From up to bottom: 7 %, 30 %, 85 % and 100 %

In the Figure 13 are represented temperature cuts from above for the four thrust regimes. As for side cuts, the plume is longer and narrower for the 7 % thrust than for other cases. This effect is also noticeable for the velocity field, as illustrated in the Figure 14.

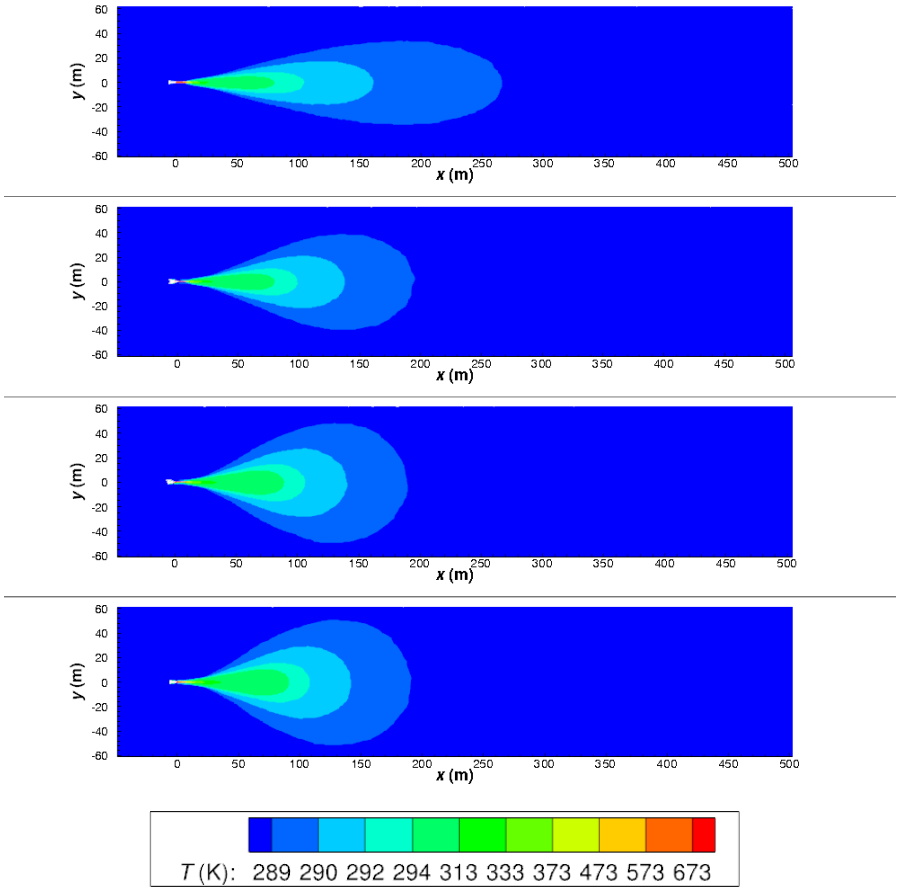

Figure 13. Temperature cut from above for the four thrusts. From up to bottom: 7 %, 30 %, 85 % and 100 %

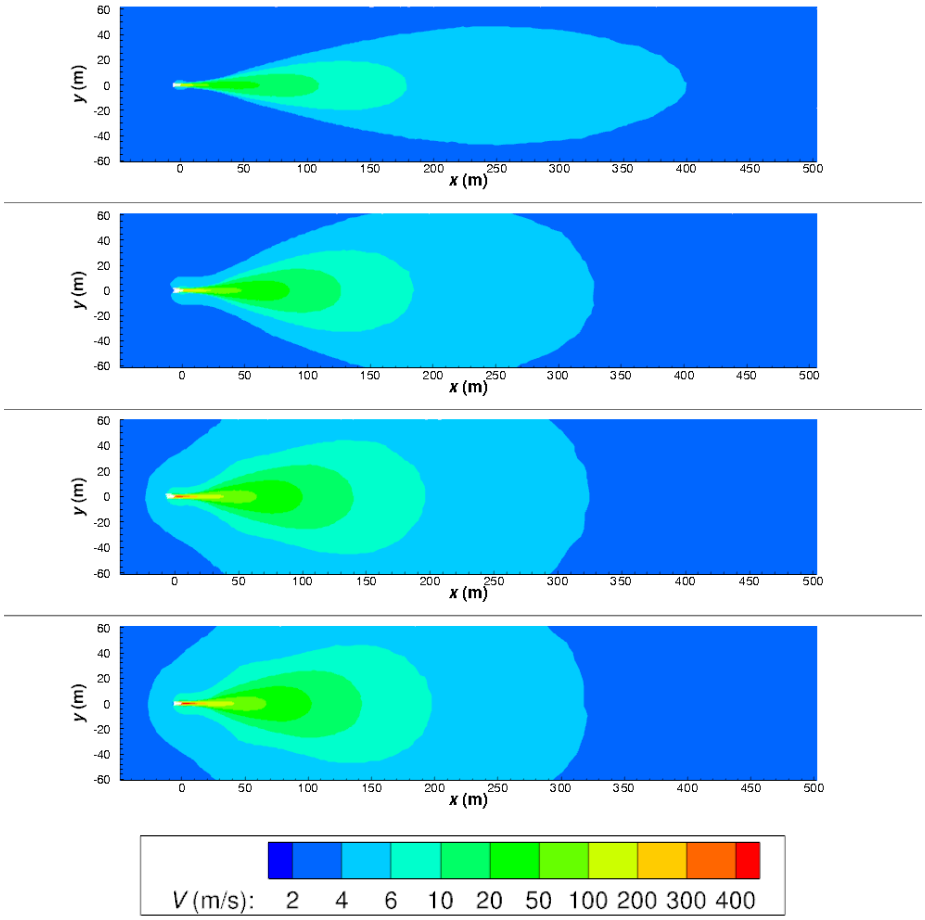

Figure 14. Velocity above cut for the four thrusts. From up to bottom: 7 %, 30 %, 85 % and 100 %

2.4.2.4. Chemical

Figure 15 to Figure 17 represent respectively NO_2, SO_2 and H_2SO_4 molar fraction side cuts for the four thrusts. As for the velocity and the temperature field, the exhaust species are transported further from the engine when the thrust is lower. When the thrust increases, those species tend to be transported to greater heights. A zoom at the engine is presented in the Figure 18 to Figure 20. Both NO_2 and SO_2 are quickly consumed, as their molar fraction is divided by 50 after 20 m. For all the species presented, their concentration fields are equivalent for all thrusts despite the difference of mass flow. In Figure 20, one can notice that H_2SO_4 is produced in the core nozzle before its actual exhaust.

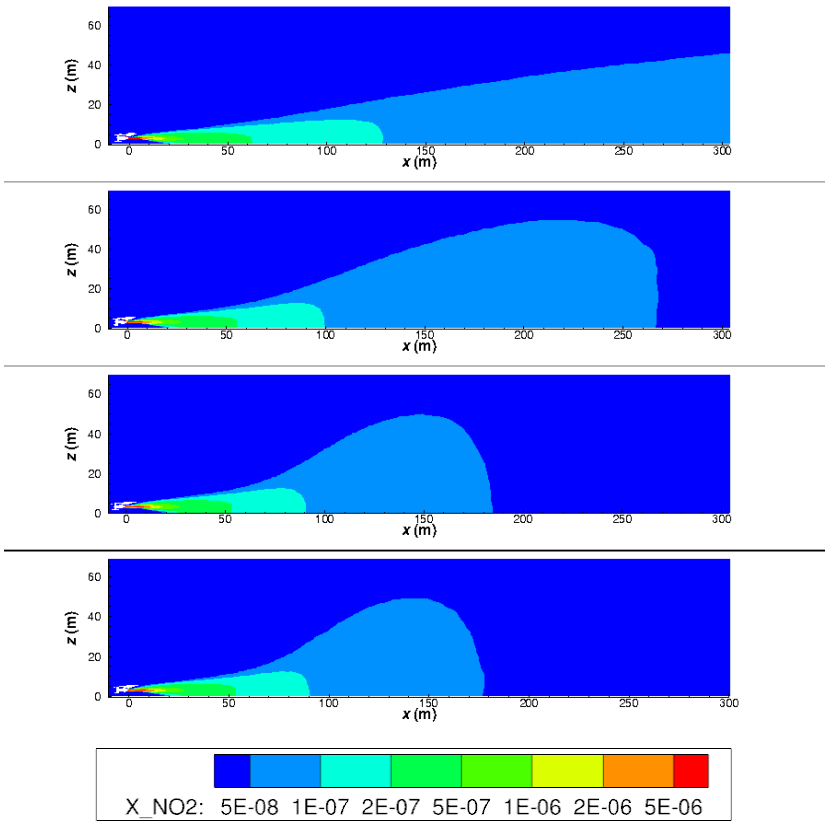

Figure 15. NO_2 molar fraction side cut for the four thrusts. From up to bottom: 7 %, 30 %, 85 % and 100 %

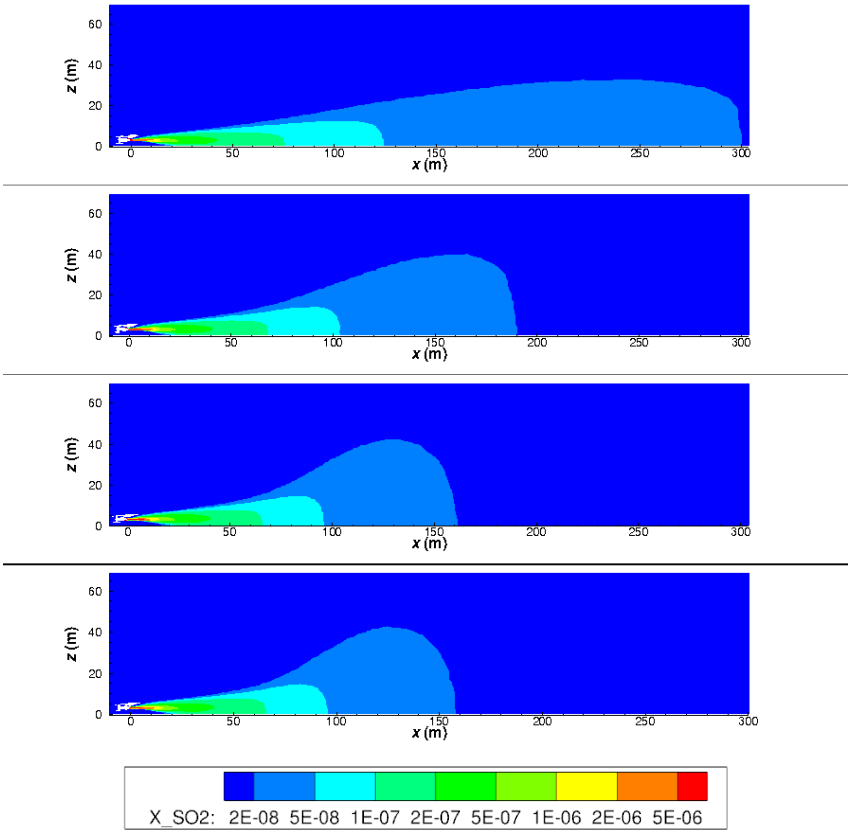

Figure 16. SO_2 molar fraction side cut for the four thrusts. From up to bottom: 7 %, 30 %, 85 % and 100 %

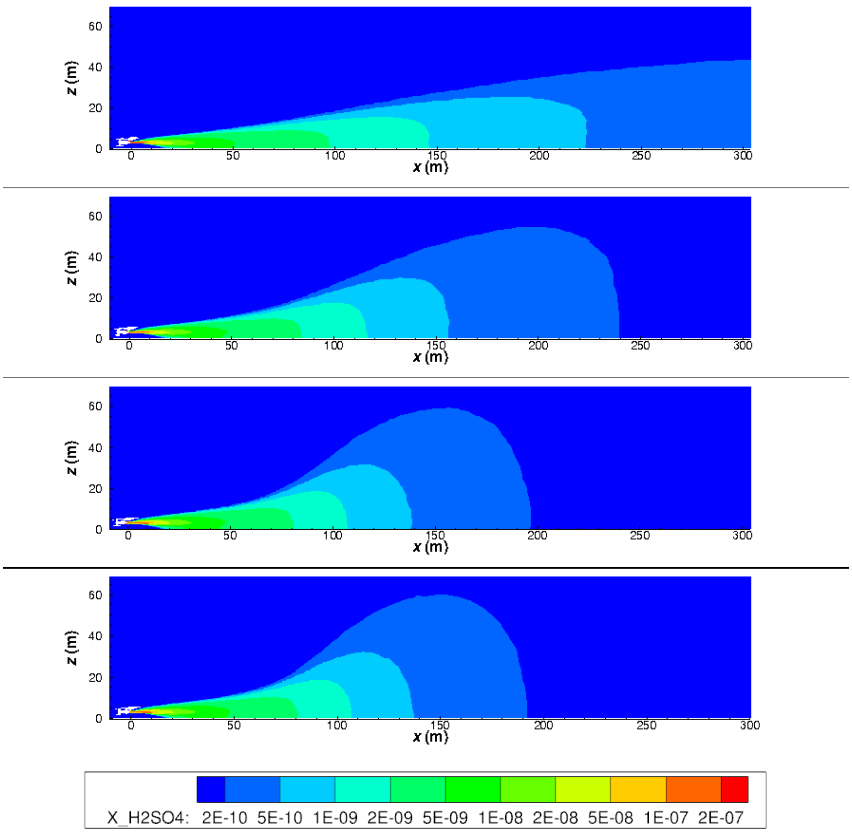

Figure 17. H_2SO_4 molar fraction side cut for the four thrusts. From up to bottom: 7%, 30%, 85% and 100%

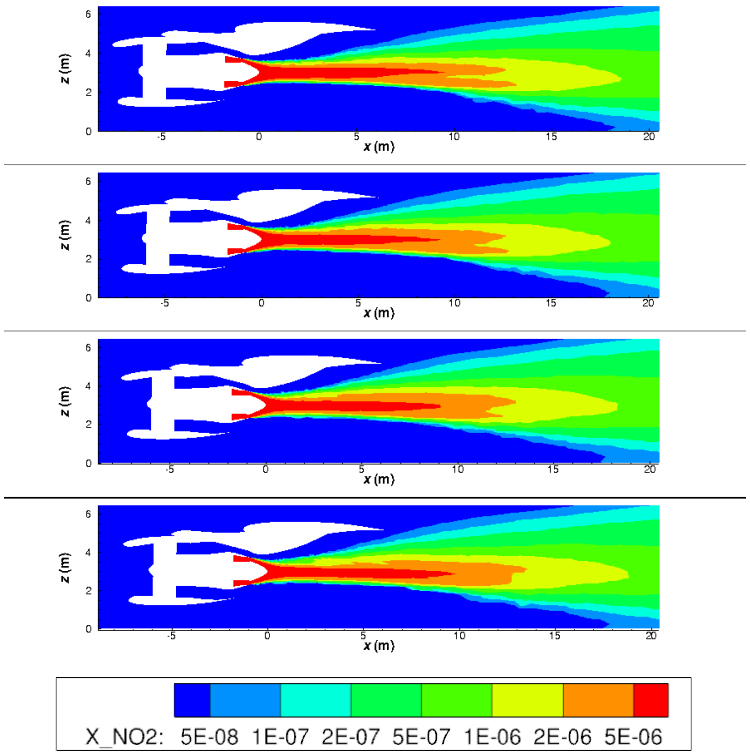

Figure 18. NO_2 molar fraction side cut for the four thrusts. Zoom on the engine. From up to bottom: 7 %, 30 %, 85 % and 100 %

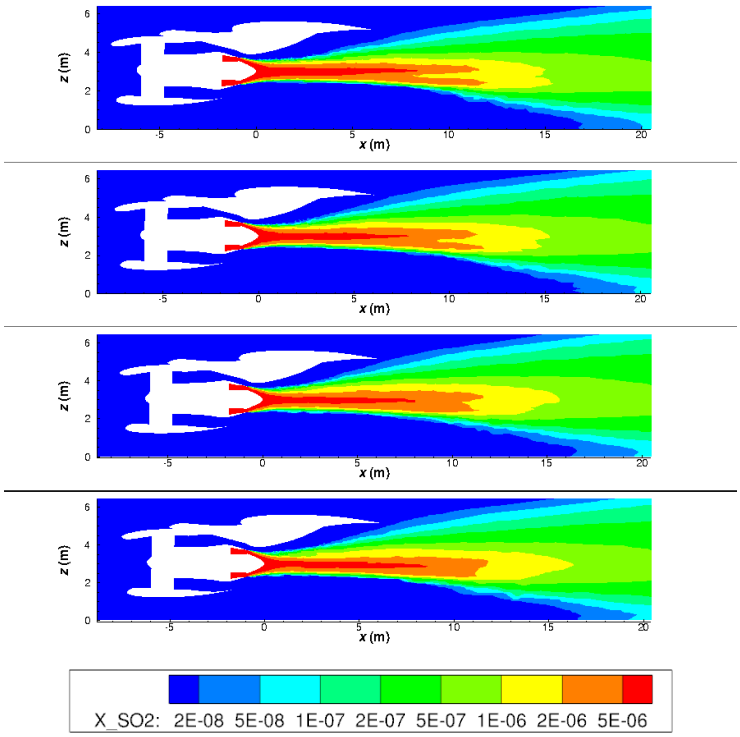

Figure 19. SO_2 molar fraction side cut for the four thrusts. Zoom on the engine. From up to bottom: 7 %, 30 %, 85 % and 100 %

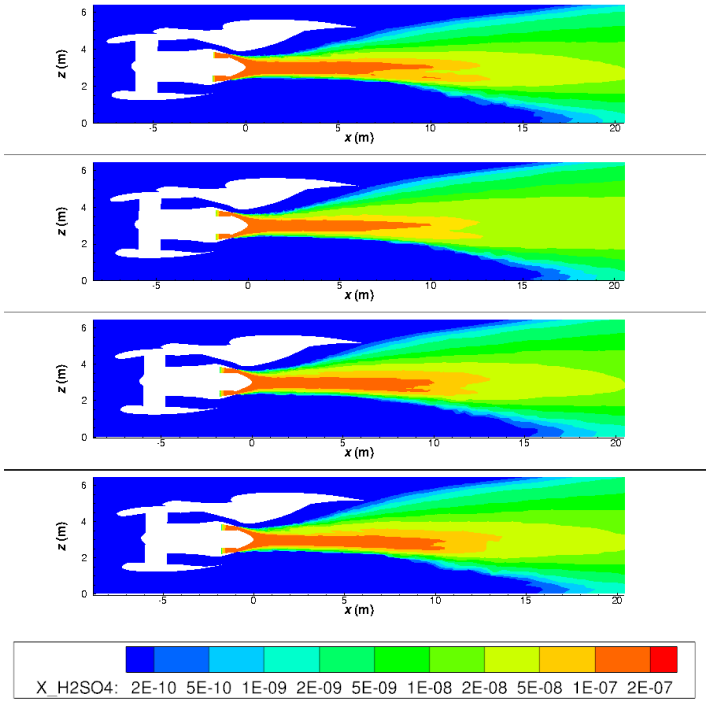

Figure 20. H_2SO_4 molar fraction side cut for the four thrusts. Zoom on the engine. From up to bottom: 7 %, 30 %, 85 % and 100 %

The Figure 22 presents the sulfur species and the relative temperature T_r along a streamline from the core exit to the outlet of the box for the four thrusts (illustrated in the Figure 21). For all thrusts, the H_2SO_4 is produced for $x < 1\mathrm{m}$ which correspond to the core nozzle. In this phase, the temperature remains constant. H_2SO_4 is then transported and its molar fraction remains constant 10 m behind the engine. SO_3 and SO_2 are slightly produced in the first part of the nozzle ($x < 3$ cm) but then SO_3 is strongly consumed to produce H_2SO_4 as illustrated in the Figure 23

for the 100 % case. For $x > 10$ m, the molar fraction of those species decreases due to diffusion and dispersion thought mixing with the ambient air. A decrease of temperature is observed 1m after the exit when the core flow gets out from the nozzle. At this point (1m after the engine's exit), the temperature drop is stronger for higher thrusts from 2 % for 7 % thrust to 23 % for 100 % thrust.

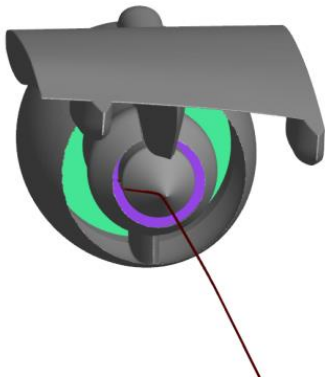

Figure 21. Illustration of the streamline used to study the species evolution at the core exhaust

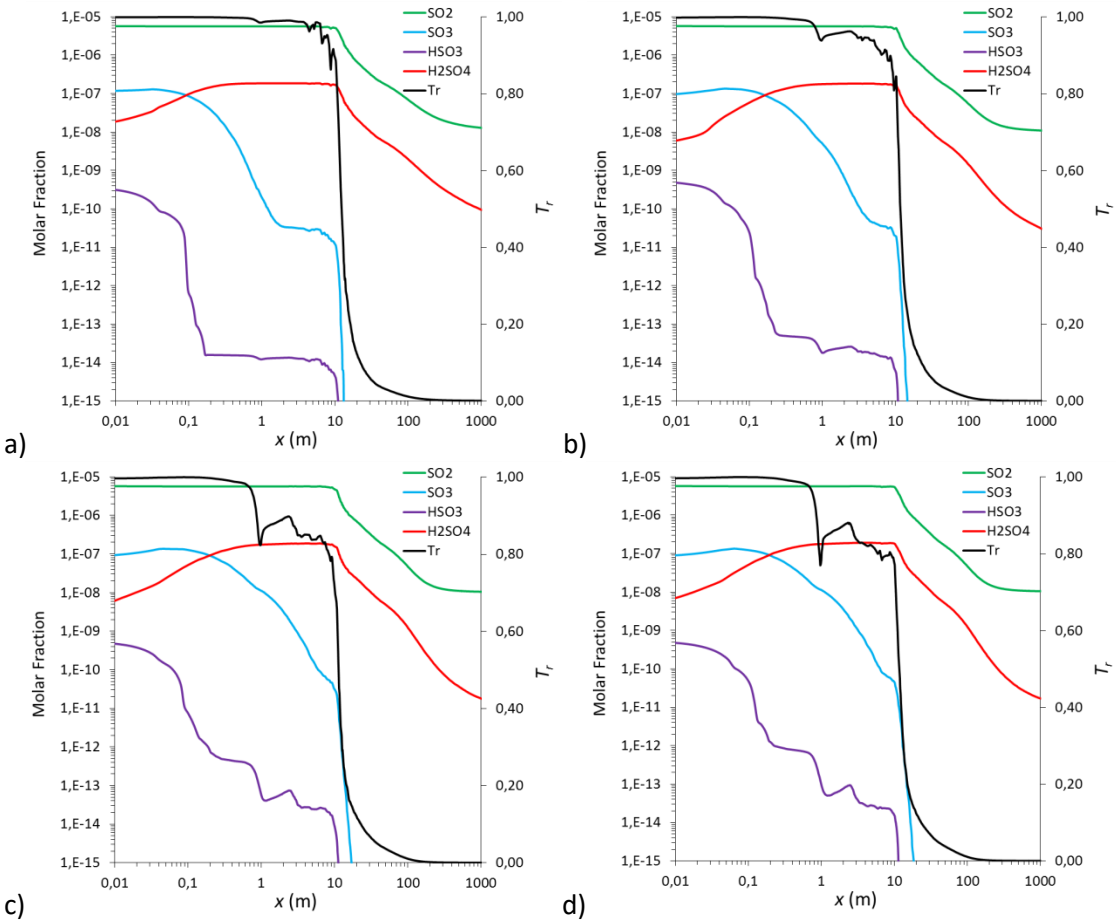

Figure 22. Molar fraction of the sulfur species and temperature along a streamline from the core nozzle to the box outlet for the four thrusts: a) 7 %, b) 30 %, c) 85 % and d) 100 %

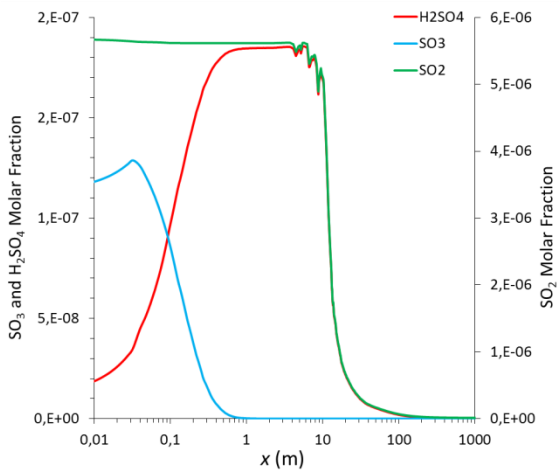

Figure 23. Molar fraction of the SO_2, SO_3 and H_2SO_4 along a streamline for 100 % thrust

To explain the temperature trend in the nozzle the Figure 24 presents the relative velocity, the relative temperature and the relative total temperature along the same streamline for the 100 % thrust case. At the nozzle exit ($x = 1$ m), the flow accelerates due to a quick change of local geometry. As the total temperature remains constant in this area, the static temperature decreases.

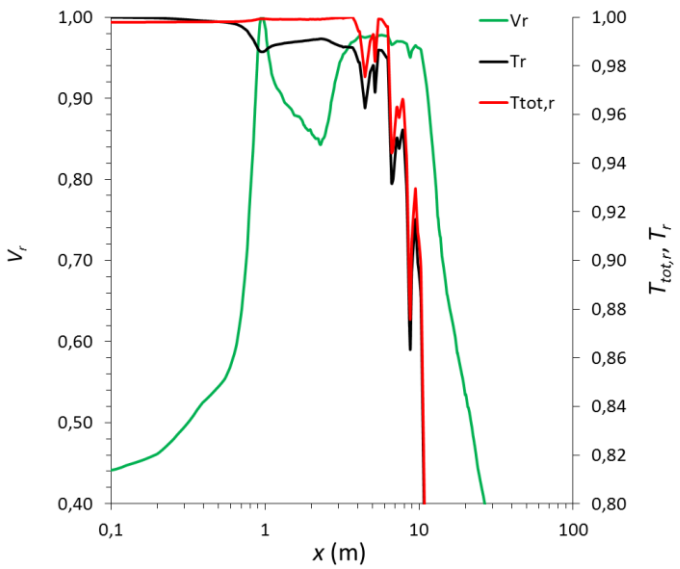

Figure 24. Relative velocity, relative temperature and relative total temperature along a streamline for the 100 % thrust case

The Figure 25 presents the evolution of several nitrogenous species molar fraction along the streamline presented in Figure 21 for the four thrusts. In all cases, NO_3 is consumed in the nozzle to produce NO_2, HNO_2 and HNO_3. At the core exit ($x = 1$m), the consumption of NO_3 is limited due to the temperature decrease. The evolution of the species far from the engine ($x > 10$ m) is then driven by the diffusion.

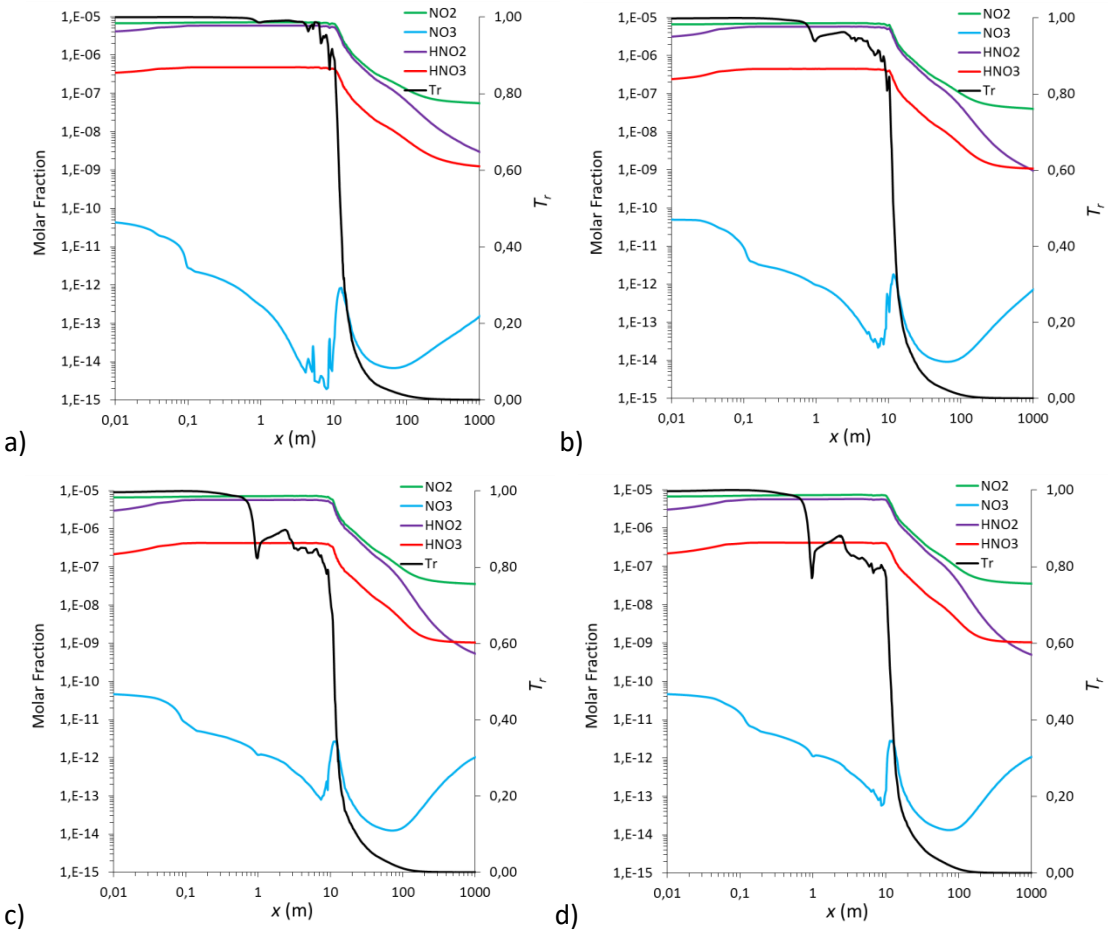

Figure 25. Molar fraction of several nitrogenous species and temperature along a streamline from the core nozzle to the box outlet for the four thrusts: a) 7 %, b) 30 %, c) 85 % and d) 100 %

2.4.2.5. Impact of ambient temperature

The previous simulations were performed for an ambient temperature of $T_a = 288.15\ K$. In Aviator project, measure campaigns are performed for different seasons (winter and summer) at Ciudad Real in Spain. The aim of this study is to evaluate the impact of the ambient temperature on the plume behind the engine. Simulations with two different ambient temperatures corresponding to the two seasons are performed: $T_a = 278.15\ K$ for winter conditions and $T_a = 303.15\ K$ for summer. For all simulations, the idle configuration is used (7% of maximum thrust). The same ambient chemical composition for all ambient temperatures is used to simplify the comparison. As the temperature is different for all cases but not the composition, the relative humidity is then impacted. The Rankine formula gives the saturated vapor pressure over water in atmosphere:

$$P_{H_2O}^{sat}\ [\mathrm{atm}] = \exp\left(13.7 - \frac{5120}{T\ [\mathrm{K}]}\right). \tag{15}$$

with P_{H_2O} the partial pressure of water. The Dalton's law gives the molar fraction of water:

$$X_{H_2O} = \frac{P_{H_2O}}{P_a}. \tag{16}$$

As $P_a = 1atm$, the relative humidity RH is then defined by:

$$RH = \frac{P_{H_2O}}{P_{H_2O}^{sat}} = \frac{X_{H_2O}}{\exp\left(13.7 - \frac{5120}{T}\right)}. \tag{17}$$

Characteristics of the atmosphere for all simulations are resumed in Table 10. The relative humidity calculated for winter and summer are close to the actual mean value presented in [26].

Table 10. Characteristics of the atmosphere

Case	Reference	Winter	Summer
T (K)	288	278	303
P (Pa)	101325		
X_{H_2O}	7.5 10^{-3}		
$P_{H_2O}^{sat}$ (Pa)	1.71 10^{-2}	9.03 10^{-3}	4.12 10^{-2}
RH	44%	83%	18%

2.4.2.6. Aerodynamics

Figure 26 represents the temperature and dilution profiles along the same streamline than in the previous study for the three ambient temperatures. For all cases, the temperature remains close to constant 7m behind the engine, which is illustrated by the constant dilution $\tau = 1$, and quickly drops for $x > 7$m. As the temperature at the bypass nozzle is assumed to be the ambient one (which is verified in the simulation) and the temperature at the core nozzle is directly linked to the temperature at the bypass nozzle by equation (9), the increase of ambient temperature impacts the core temperature. Therefore, the exhaust temperature increases with the ambient temperature. However, the dilution is identical for all ambient temperatures. The same trends can be observed in the radial profiles presented in the Figure 27.

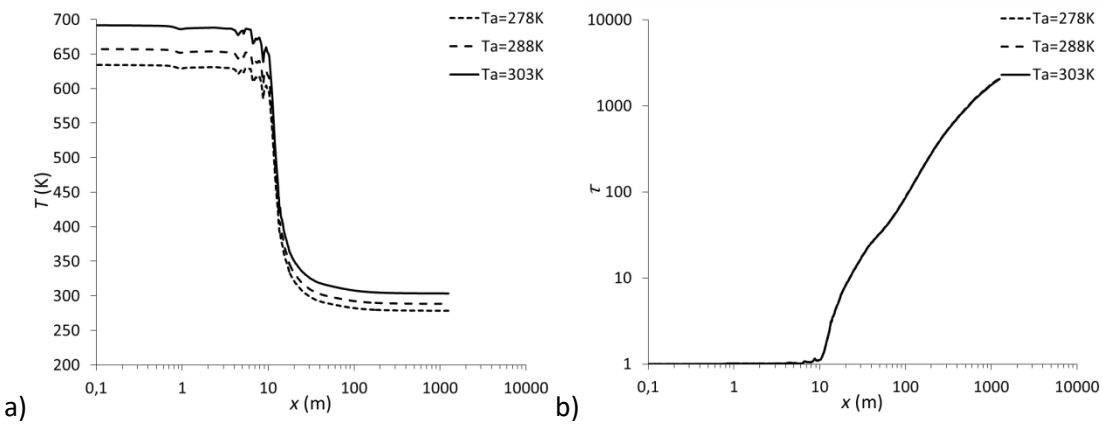

Figure 26. Temperature (a) and dilution (b) along a streamline for the 3 ambient temperatures. Profiles extracted in the center of the plume

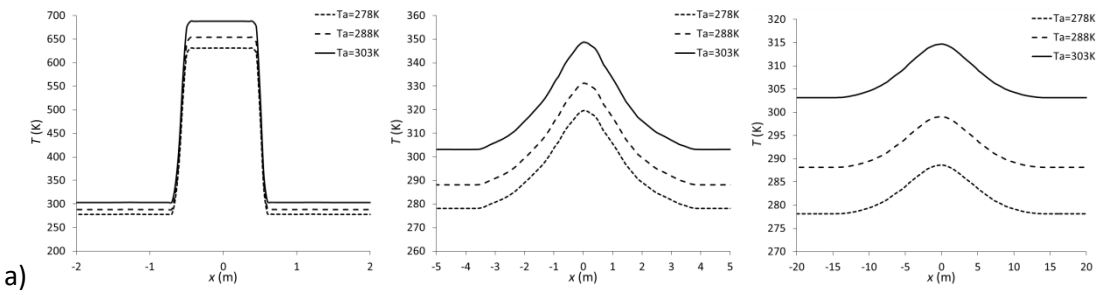

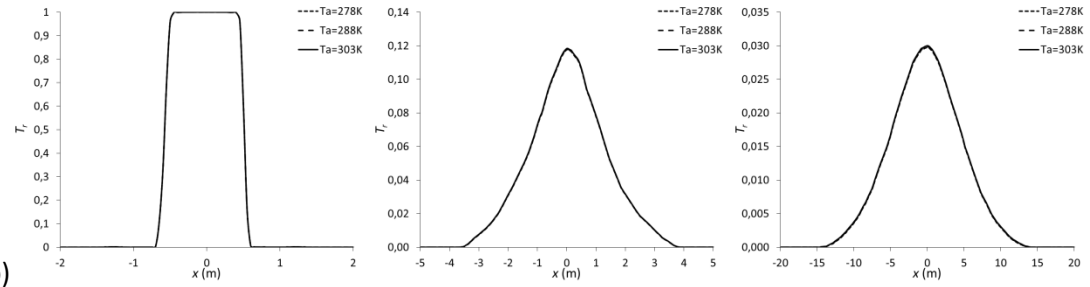

b)

Figure 27. Temperature (a) and relative temperature (b) radial profiles at three positions behind the engine. From left to right: $x = 0\ m$, $x = 20\ m$ and $x = 50\ m$

In the Figure 28 are represented the velocity and the relative velocity profiles extracted along a streamline for the three ambient temperatures. For all cases, the same trend is observed. For $x < 1$ m, the core flow accelerates in the nozzle. A deceleration is then observed for $1\ \mathrm{m} < x < 2.3$ m, due to a modification of the direction of the flow as illustrated in the Figure 21. Another acceleration to reach a plateau is observed when all the streamlines follow the same direction for $2.3\ \mathrm{m} < x < 10$ m. Finally, the velocity decreases for $x > 10$ m. The difference in ambient temperature as a slight impact on the velocity but the relative velocity is equivalent in all cases, as for the relative temperature.

The impact of ambient temperature on exit velocities can be explained by the relations presented in 2.4.2. By combining the relations (8), (10) and (11), a quadratic equation for u_{core}^{nozzle} is obtained:

$$F = \frac{A_{bypass}^{nozzle}\rho_{bypass}^{nozzle}}{\psi\phi}\left(1+\frac{\psi}{\phi}\right)\left(u_{core}^{nozzle} - (1-\phi)u_0\right)\left(u_{core}^{nozzle} - u_0\right), \tag{18}$$

whose solution is:

$$u_{core}^{nozzle} = u_0\left(1-\frac{\phi}{2}\right) + \sqrt{\left(\frac{\phi u_0}{2}\right)^2 + \frac{F\psi\phi}{A_{bypass}^{nozzle}\rho_{bypass}^{nozzle}(1+\psi/\phi)}}. \tag{19}$$

In this solution, all the parameters are temperature independent except the bypass nozzle density. The core nozzle velocity increases then with the ambient temperature due to the bypass nozzle temperature decrease.

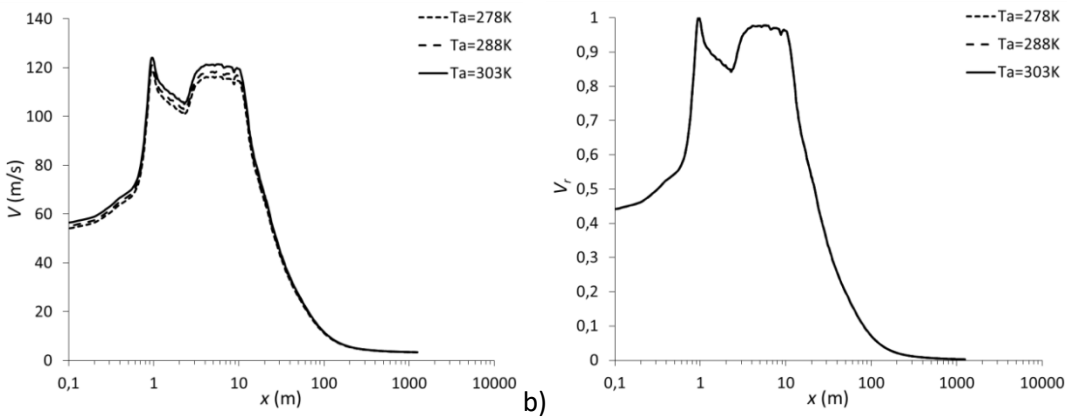

a) b)

Figure 28. Velocity (a) and relative velocity (b) versus distance behind the engine for the three ambient temperatures. Profiles extracted in the center of the plume

In the Figure 29 are presented the velocity and relative velocity radial profiles at three positions behind the engine. For $x = 0\ m$, the velocity peaks correspond to the core exit and the plateau close to $y = \pm 1\ m$ corresponds to the bypass exit. The difference of ambient temperature has

only a slight impact on the velocity radial profile at the exit, and this effect decreases as the flow get far from the engine.

The local maximum of relative velocity decreases slower than the local maximum of relative temperature, which can be observed by comparing Figure 27 (b) and Figure 29 (b). Therefore, the temperature is diffusing faster than the velocity. The modification of ambient temperature has no impact on the relative velocity profiles, as for the relative temperature profiles.

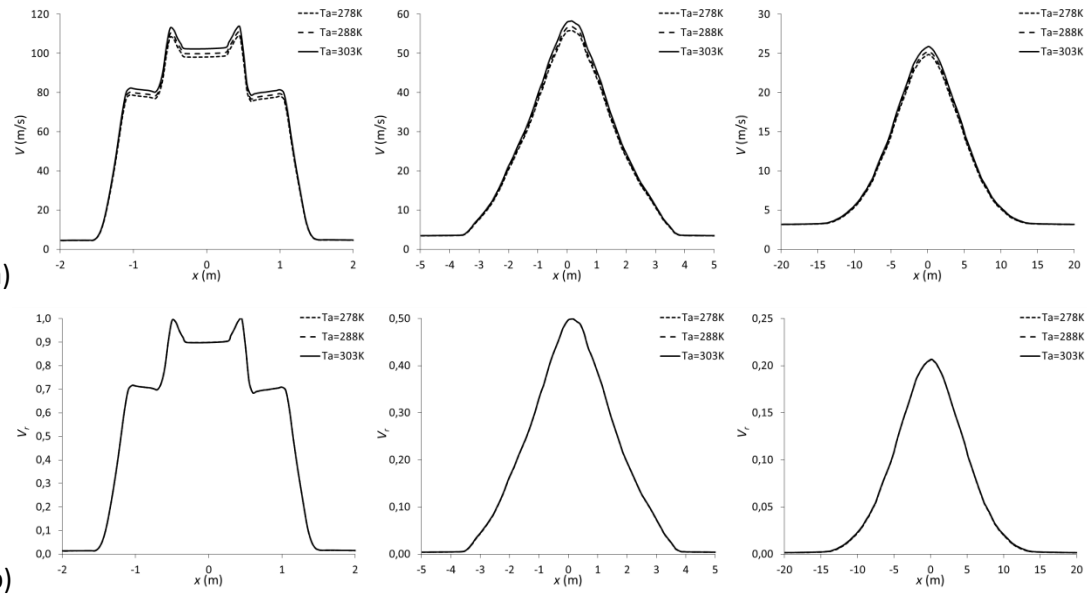

Figure 29. Velocity (a) and relative velocity (b) radial profiles at three positions behind the engine. From left to right: $x = 0\ m$, $x = 20\ m$ and $x = 50\ m$

2.4.2.7. Chemical

In the Figure 30 are presented the molar fraction profiles along a streamline for SO_3, H_2SO_4, NO_2 and NO_3. For $x < 1$ m, the molar fractions of all the presented species are higher due to a greater production as the temperature increases. After the decrease of temperature for $x > 10$ m, the impact of ambient temperature becomes negligible, which is illustrated as an example in the radial profiles presented in the Figure 31.

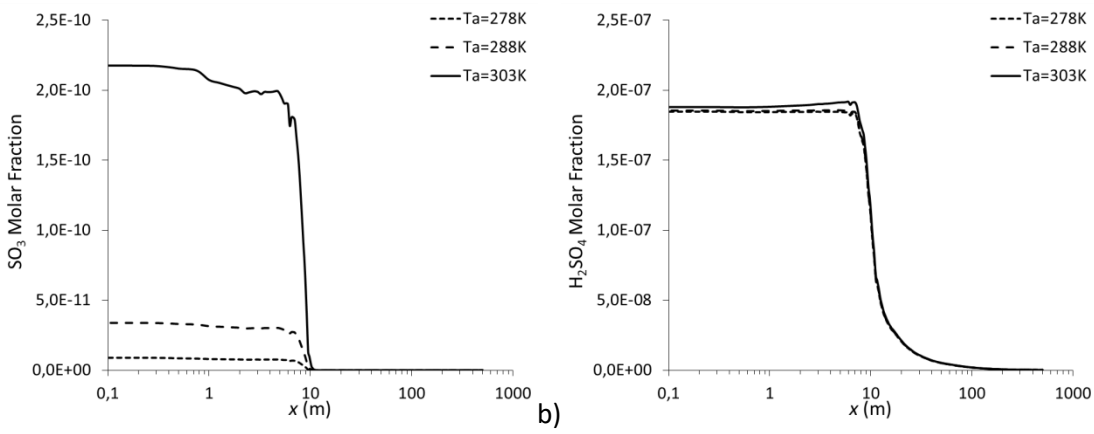

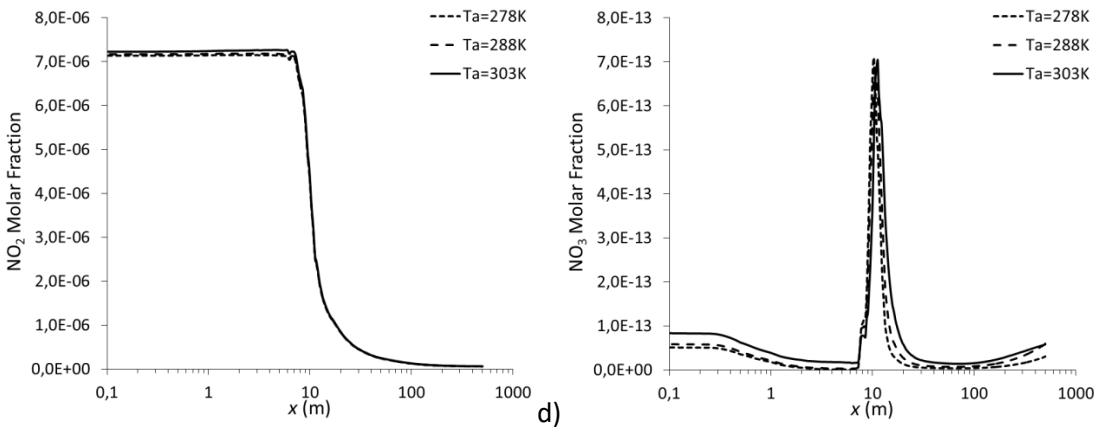

Figure 30. Molar fraction profile along a streamline: a) SO_3, b) H_2SO_4, c) NO_2 and d) NO_3

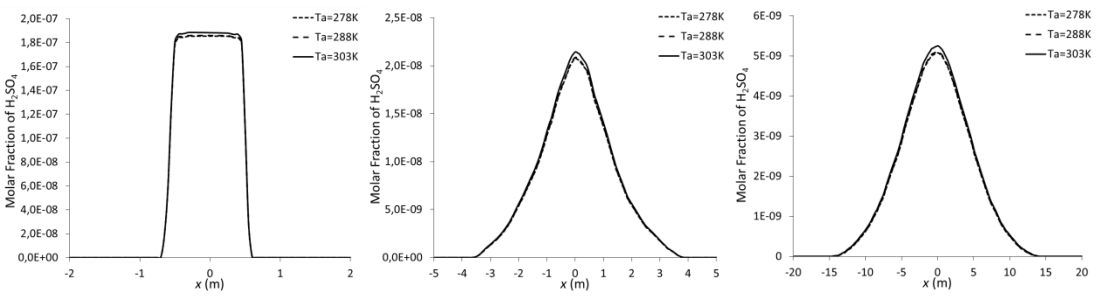

Figure 31. Molar fraction of H_2SO_4 radial profiles at three positions behind the engine. From left to right: $x = 0\ m$, $x = 20\ m$ and $x = 50\ m$

2.5. Comparison between numerical results and experimental data

2.5.1. Comparison of engine exit data

For this study, the boundary conditions for the engine exit has been determined with analytical models and assumptions which are detailed in section 2.4.2, resulting to choices for temperature, mass flow, velocities and species mass fraction. A comparison of measured temperature during the Aviator campaign and the modeled temperature is presented in the Table 11. It is important to note that different engines were used between the experimental campaign and as CAD for the CEDRE simulations. Indeed, for the RANS simulations, the engine used was the modern Trent engine whereas the engines used for the campaign were the Trent 500 (temperature range is due to the multiple measurements performed for a given thrust). Another point to underline is that for the CEDRE simulations, the high thrusts were set to 85 % and 100 % of maximum thrust, which could not be attained during the campaign, where a maximum of 80 % could be obtained. The modeled temperature at the engine exit is close to the measured one for low thrusts but is 10 % lower for 80 % thrust. The range of temperature measured for 7 % thrust is quite large due to different fuel and ambient conditions.

Table 11. Measured (WP3) and modeled (WP5) temperature at the engine core exit for different thrusts

Thrust	$T_{engine\ exit\ WP3}\ (K)$	$T_{engine\ exit\ WP5}\ (K)$
7 %	665 – 725	657
30 %	678 – 684	680
80 %	804 – 808	731

2.5.2. Comparison of data in the plume

As a common variable, the CO_2 concentration is used to compare the Dilution Factor (DF) from both modelled and measured values. It is defined as followed:

$$DF = \frac{X_{CO_2,engine\ exit} - X_{CO_2,ambient}}{X_{CO_2} - X_{CO_2,ambient}}, \tag{20}$$

This quantity varies between 1 at the engine exit and infinity when the exhaust flow is infinitely diluted with the ambient conditions. The dilution factor versus distance behind the engine for the different thrusts is presented in the Figure 32. The dilution factor obtained from the Aviator experimental campaign is also plotted for comparison. Globally, good trends are observed between model and experimental data 50 m behind the engine. For 7 % thrust, the CFD model gives comparable results compared with the experimental data for all distances. For higher thrusts, the model overestimates the dilution factor for distances higher than 50 m. With the CFD model, the dilution factor far from the engine increases with the thrust, which is coherent with the large spread horizontal and vertical spread observed from Figure 11 to Figure 17. At the contrary, the dilution factor observed from the experimental data decreases when the thrust increases, which means that the species are transported at larger distances with high thrust. Those contradictory tendencies may be explained by the differences between the engine exhaust conditions that were applied to the CFD model. Indeed, the large spread of the plume obtained with the CFD simulations can be due to the values taken for the engine velocities and turbulence both at secondary and primary outlet, which may not be representative of what happened during the campaign. This is a source of motivation for later projects to have stronger interactions between modelers and manufacturors in the aim to have robust experimental data as initial data for the CFD simulations.

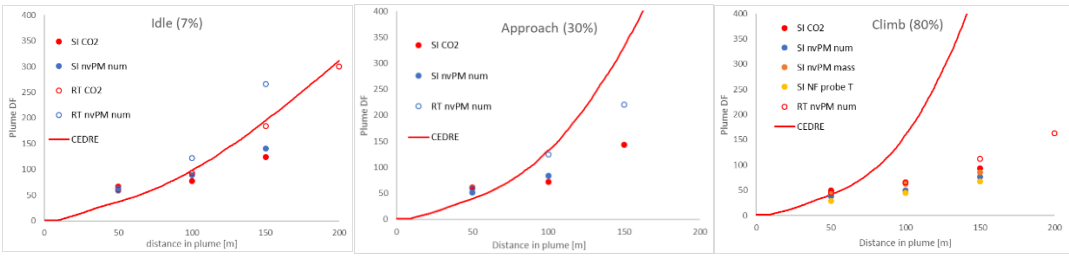

Figure 32. Dilution factor versus distance behind the engine (m) for 7 %, 30 % and 80 % thrust

The velocity in the plume for different engine's thrust and distances is presented in Figure 33. The values obtained for the velocities seem globally in the same order of magnitude with the CFD simulations regarding the experimental campaign for distances higher than 50 m. For 25m, the CFD simulation provides higher velocities ($v > 100$ m/s for 30 % and 85 % thrust than those observed during the campaign. However, the data for winter jet-A at 25 m seems really low, which can be due to a deviation of the plume due to strong side wind.

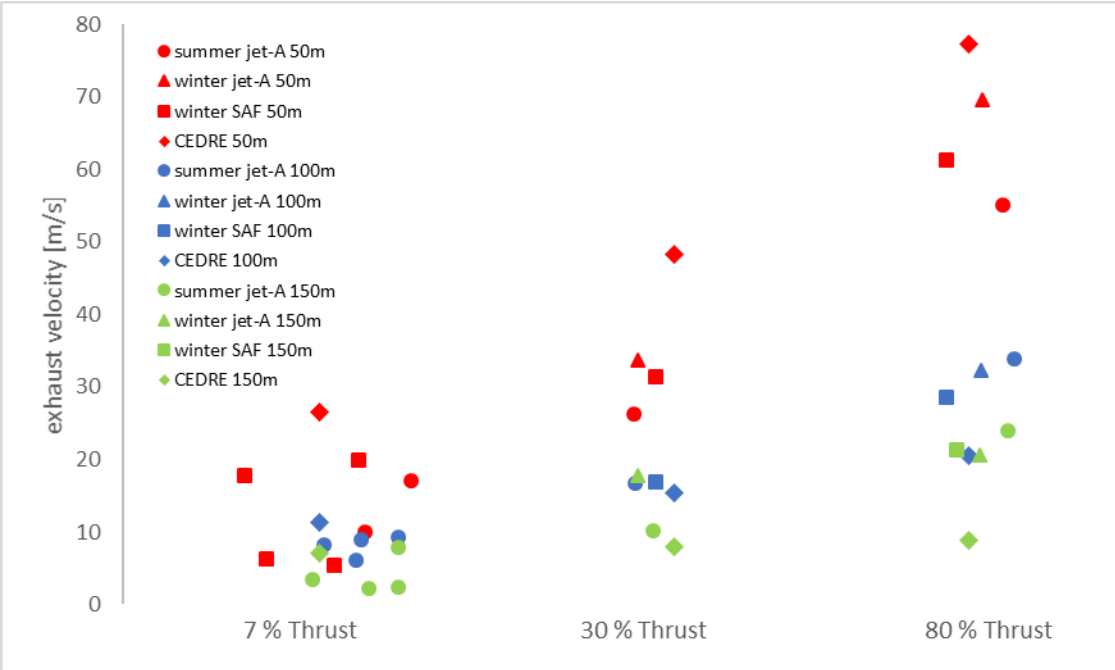

Figure 33. Exhaust velocity (m/s) versus percentage of the full thrust (%) for different distances behind the engine

2.5.3. Sensibility of ambient wind speed

For all simulations that were presented until here, the wind speed was set up to 3 m/s in the direction of the engine. Another simulation was performed for the 30% thrust case by increasing the wind speed velocity to 5 m/s to study the impact on the dilution law. A comparison of dilution factor versus distance behind the engine for 30 % thrust is presented in Figure 34. The increase of the wind speed slightly impacts the two quantities which remain higher at larger distance from the engine, reducing the difference with the experimental data. However, the gap between CEDRE simulation results and the experimental data set remains of the same order of magnitude. Thus, the discrepancies between CFD results and the experimental data that are observed for strong thrusts should principally come from the different characteristics of the two specific exhaust flow (modern Trent engine vs old Trent engine).

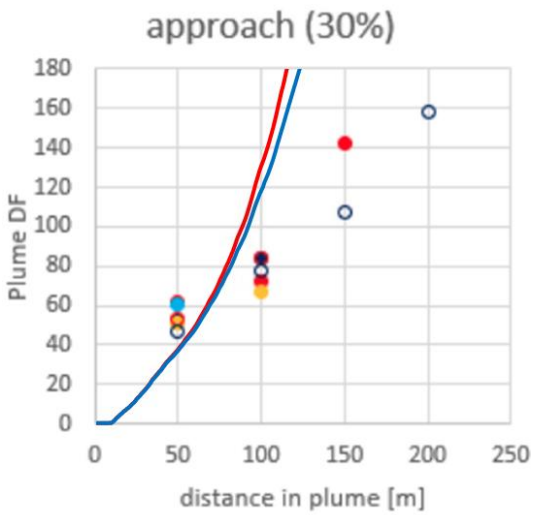

Figure 34. Plume Dilution Factor (DF) versus distance behind the engine (m) for approach conditions (30 % thrust) with different wind speed set as ambient conditions for the CFD model: 3 m/s (red line) and 5 m/s (blue line)

3. Configuration 2 and 3: A350

3.1. Aircraft configuration

To study the hot and turbulent exhaust of aircraft engines, a realistic configuration is needed. The A350 CAD is presented on the Figure 35. For this configuration, the aim is to study the plume behind the plane during the approach (configuration 2) and the climbing (configuration 3) regimes. The CAD contains the plane and the two modern Trent engines.

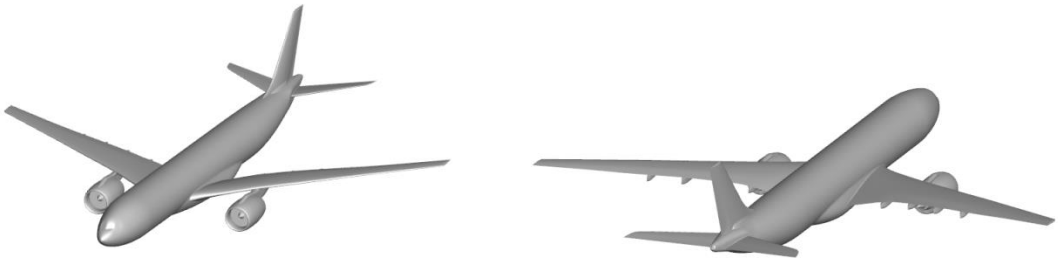

Figure 35. CAD of the A350 equipped with 2 modern Trent engines

3.2. Computational domain

The computational domain is defined by a box containing the engine geometry. To limit the effects of the boundary on the flow, the boundaries of the box are set far from the aircraft. The extension of the domain is around 10 spans before the plane and 15 spans behind the plane. The left, right, top and bottom boundaries are set to 11 spans from the aircraft. For those configurations, the box is oriented in the same direction than the plane. Table 12 presents the computational domain dimensions for the simulations carried out for the C1 configuration. The span b of the corresponding plane is close to 58 m.

Table 12. Computational domain dimensions

L_x	$[-10b, 15b]$
L_y	$[-11b, 11b]$
L_z	$[-11b, 11b]$

3.3. Boundary and initial conditions

For both configurations, the original idea was to study the plume when the plane is 200 m high. But the approach and climbing steps are unsteady phenomena as the aircraft is moving from the ground. Those conditions cannot be properly simulated with RANS steady simulations, so the conditions have been changed to be able to perform simulations to the detriment of some characteristics of those configurations. The ground does not appear as a physical wall in the computational domain, which means that the simulation cannot reproduce the eventual interaction between the plume and the ground. The plume will then develop freely behind the aircraft and its characteristic time can be calculated. The properties of the ambient atmosphere are fixed ($T_a = 288.15$ K, $P_a = 101325$ Pa) assuming that those conditions remain constant regarding the simulated plume dilution, which will be verified later. The Figure 36 illustrates the transformation of the configuration 3 for the simulation.

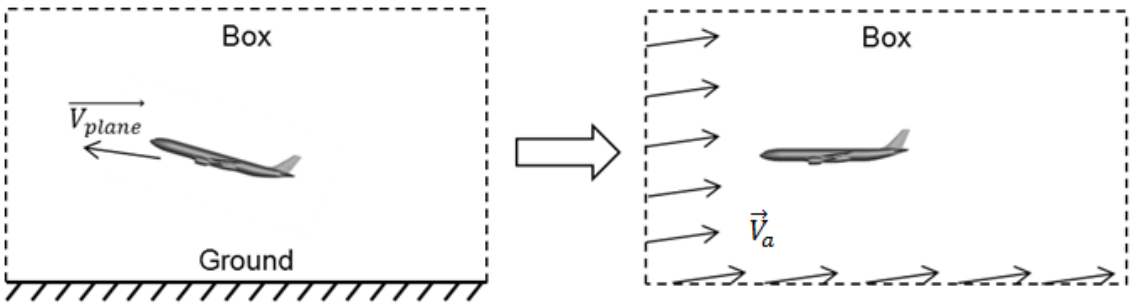

Figure 36. Illustration of the transformation for the climbing configuration case (side view)

Table 13 sums up the boundary conditions imposed in the limit of the computational domains. Slip conditions are imposed on the side and the top of the box. Pressure condition is imposed at the outlet and the top of the box due to the direction of the upwind flow. Temperature and velocity conditions are imposed at the inlet and at the bottom, as illustrated in Figure 36. For the approach, the velocity of the upwind flow is set to 70 m/s and the angle of attack α_{aa} to 6°. For the climbing configuration, the velocity of the upwind flow is set to 110 m/s and the angle of attack α_{aa} to 8°.

Table 13. Computational domain boundary conditions

Boundary	Position	Condition
Inlet	$x = -10b$	Velocity and temperature imposed
Outlet	$x = 15b$	Pressure imposed
Left	$y = -11b$	Slip
Right	$y = 11b$	Slip
Bottom	$z = -11b$	Velocity and temperature imposed
Top	$z = 11b$	Pressure imposed

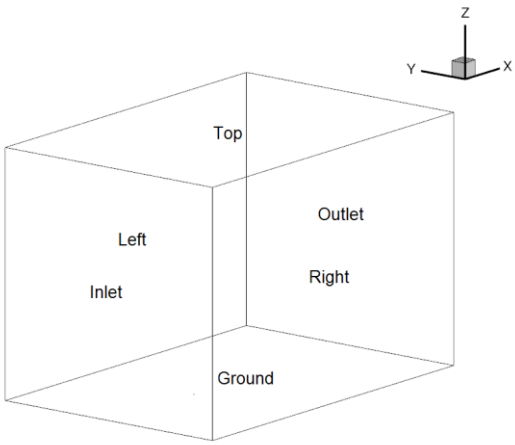

Figure 37. Boundary conditions for computational domain

For the plane and the engines, a wall condition is imposed except for the fan entry for which a pressure condition is applied and for the bypass and core exits for which a total temperature and surface mass flow are applied. For exhaust and ambient atmosphere, the same chemical composition than presented for the engine only configuration (configuration 1) are specified.

To calculate the conditions for the core and the bypass, as for the configuration 1, an assumption is needed on the parameter ϕ. In this study, we assume that the core temperature for configuration 2 and 3 is the same than for configuration 1 at equivalent thrust (30 % for configuration 2 and 85 % for configuration 3). This assumption leads to $\phi = 1.714$ for configuration 2 and $\phi = 1.645$ for configuration 3. Table 14 summarized the CEDRE parameters for the landing and climbing configurations.

Table 14. CEDRE parameters for the configurations 2 and 3

Configuration	Landing (C2)	Climbing (C3)
u_a (m/s)	70	110
F/F_{max}	30 %	85 %
T_{core}^{tot} (K)	685	740
T_{bypass}^{tot} (K)	308	343
$\dot{m}_{core}$ (kg/m²/s)	75	124
$\dot{m}_{bypass}$ (kg/m²/s)	197	327

3.4. Results

3.4.1. Grid mesh optimization

In this section, the different steps of the grid mesh optimization are presented to show the progressive refinement of the mesh in the plume and in the zone defined by the wing tip vortex. As in the paragraph 2.4.1 for configuration 1, V_t is used as the refinement parameter.

The interaction between the wing and the upwind flow is more complex than for configuration 1 due to the production of a wake vortex sheet which can interact with the exhaust flow. Thus, the refinement methodology must be adapted to be able to precisely characterize those phenomena. For the configuration 1, the complexity was set to 32000 and 4 adaptation steps were made. For the configurations 2 and 3, the same number of adaptation steps is performed to get a converged mesh for increasing complexity, from $c = 32000$ to $c = 100000$. The maximum value for complexity is chosen as a compromise between the simulation costs and the quality of the mesh refinement. Table 15 summarizes the mesh characteristics for each complexity after 4 mesh refinements.

Table 15. Grid mesh characteristics for the configurations 2 and 3

Grid Mesh	Complexity	C2 number of tetrahedrons	C3 number of tetrahedrons
1	/	16,506,997	16,506,997
4	32000	4,323,662	4,326,413
8	50000	5,022,710	5,014,885
12	75000	5,676,679	5,313,915
16	100000	6,342,468	5,562,716

As an example, the Figure 38 and the Figure 39 illustrate lateral cuts in the plane of the engine for the meshes presented in Table 15. After the first step, the mesh is refined in the region of the plume and is coarse elsewhere, particularly at the box boundaries, resulting to a decrease

of the number of tetrahedrons. Each following increase of the complexity increases the number of tetrahedrons. The mesh in the plume close to the engine is more and more detailed and the fine mesh region is spreading each time the complexity is higher.

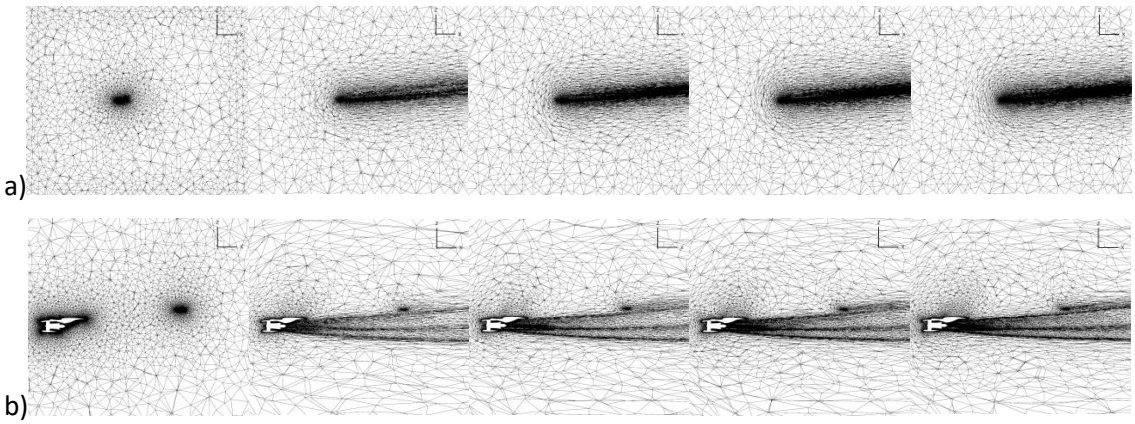

Figure 38. Side cut of meshes for the configuration 2 presented in Table 15: (a) global mesh; (b) zoom on the engine

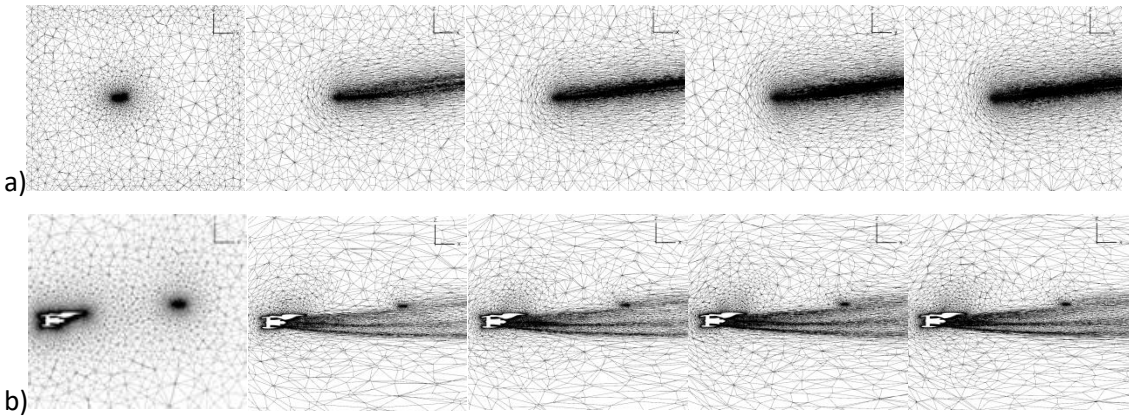

Figure 39. Side cut of meshes for the configuration 3 presented in Table 15: (a) global mesh; (b) zoom on the engine

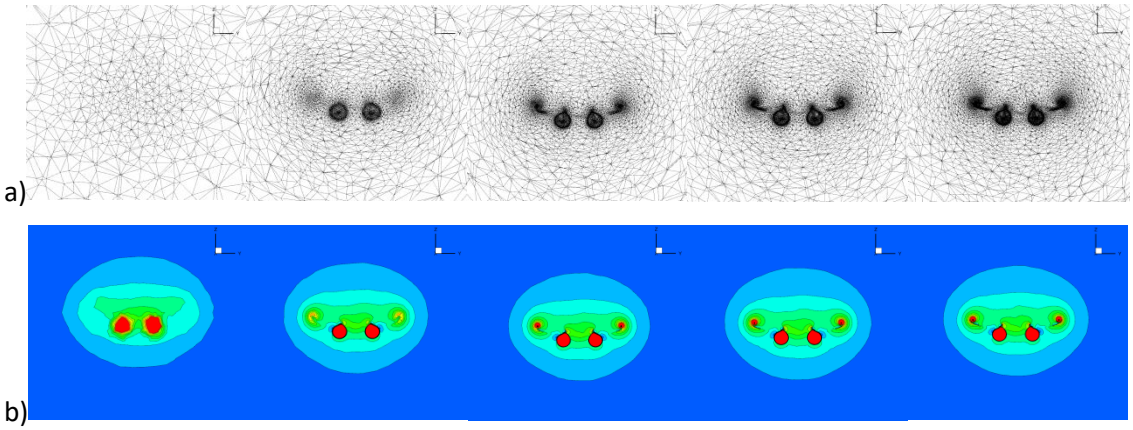

Figure 40. Cut at 1 span downstream of the wing tip for the meshes for the configuration 2 defined in Table 15: a) mesh; b) E_s field

a)

b)

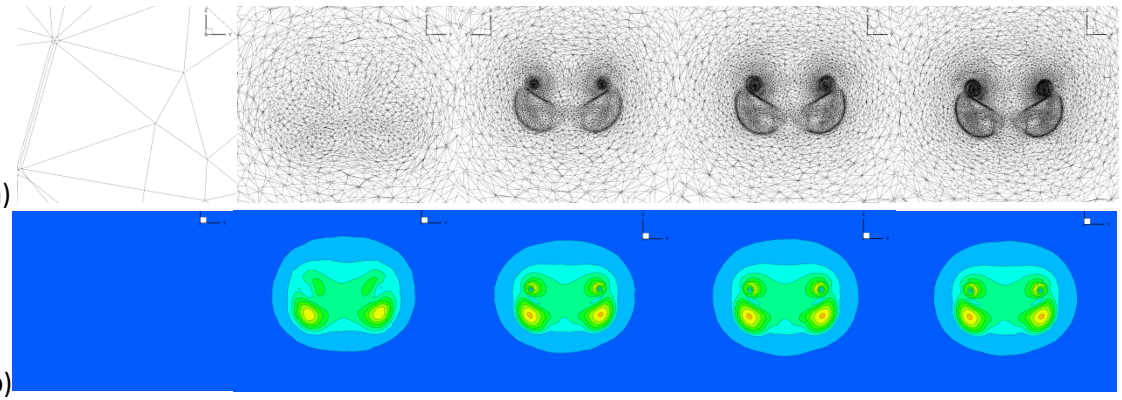

Figure 41. Cut at 8 spans downstream of the wing tip for the meshes for the configuration 2 defined in Table 15: a) mesh; b) E_s field

From Figure 40 to Figure 45 are illustrated the mesh and the E_s fields at different distance behind the plane (1 span, 8 spans and 15 spans) for both configurations. Those figures show the efficiency of this parameter to capture the wing tip vortex and its interaction with the jet-wake.

a)

b)

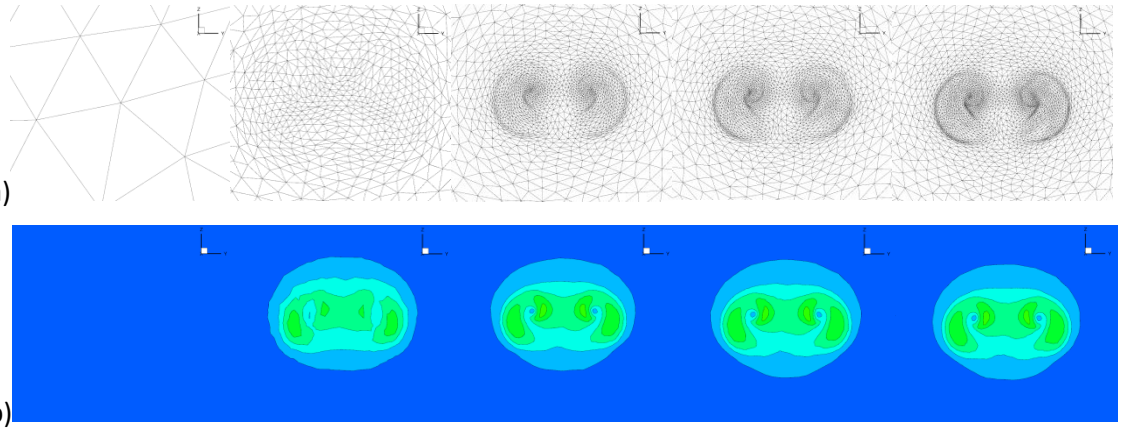

Figure 42. Cut at 15 spans downstream of the wing tip for the meshes for the configuration 2 defined in Table 15: a) mesh; b) E_s field

a)

b)

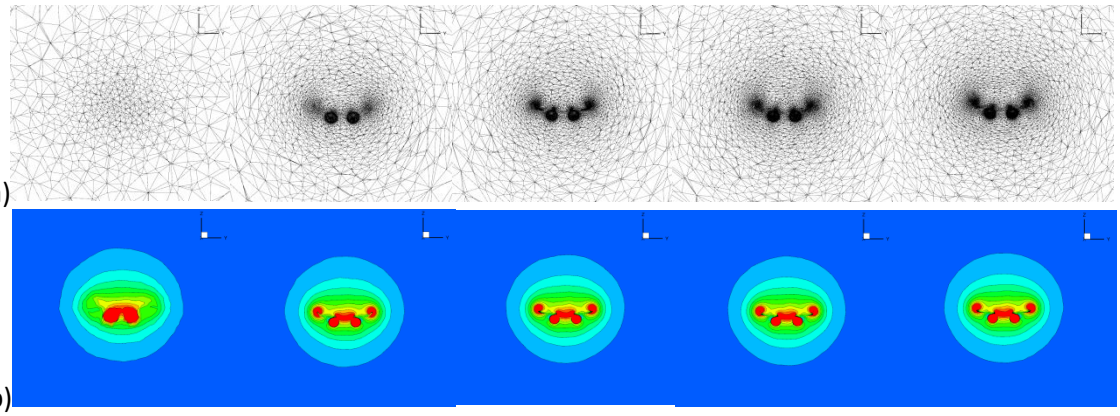

Figure 43. Cut at 1 span downstream of the wing tip for the meshes for the configuration 3 defined in Table 15: a) mesh; b) E_s field

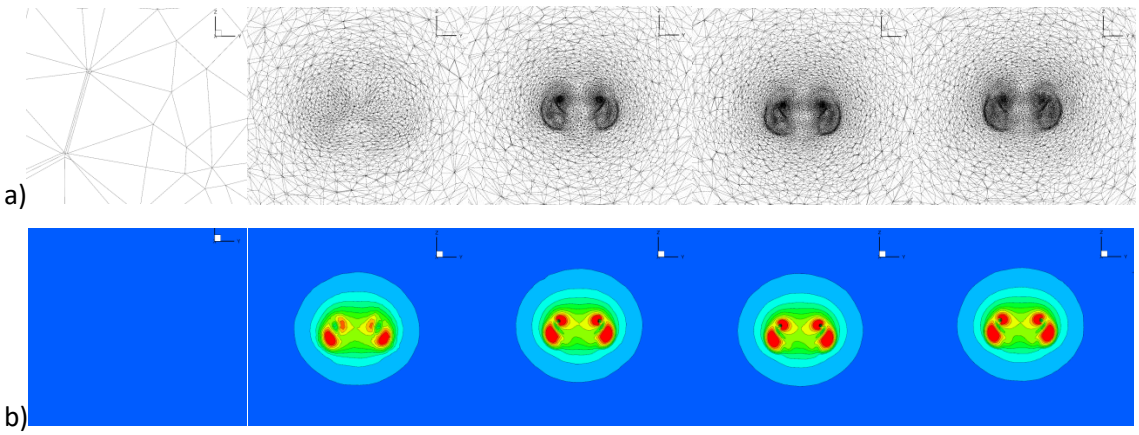

Figure 44. Cut at 8 spans downstream of the wing tip for the meshes for the configuration 3 defined in Table 15: a) mesh; b) E_s field

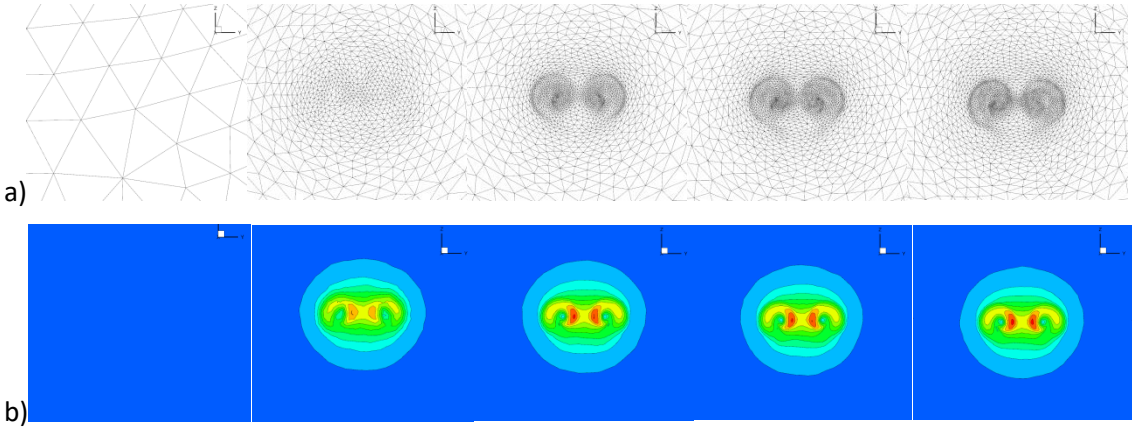

Figure 45. Cut at 15 spans downstream of the wing tip for the meshes for the configuration 3 defined in Table 15: a) mesh; b) E_s field

3.4.2. Aerodynamics

The Figure 46 presents the streamlines for the loading and climbing configurations. The wing tip vortex illustrated by the purple streamlines has an impact on both the vorticity sheet and the exhaust flow. The streamlines from the core and the bypass exits, respectively in red and orange, wrap around the wing tip vortex. The rolling-up of the exhaust flow seems more important for the climbing configuration, as illustrated in the Figure 47. Three main parameters explain the difference of the wing tip/exhaust interaction between the two configurations: the angle of attack, the upwind speed and the thrust.

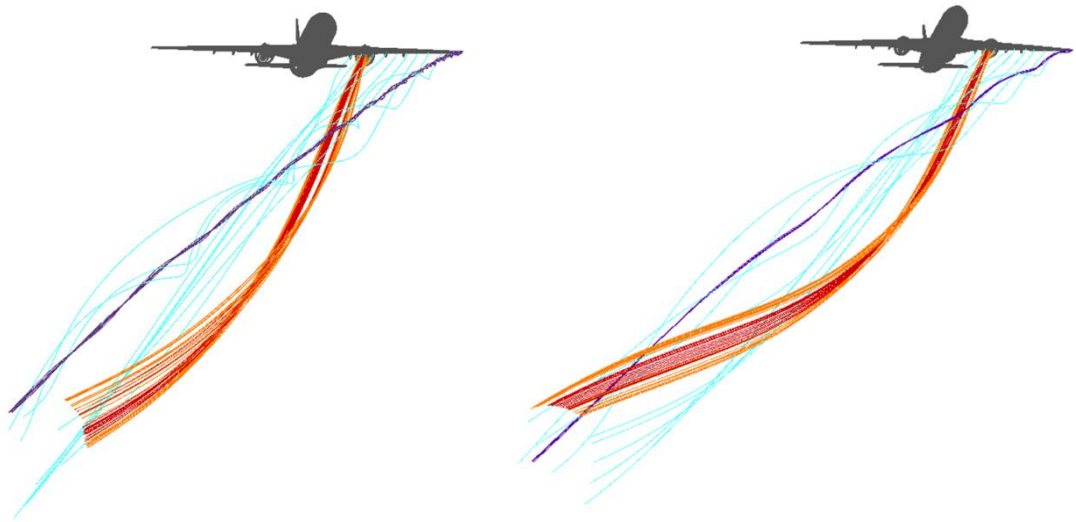

Figure 46. Streamlines for the landing (left) and climbing (right) configurations: core flow (red), bypass flow (orange), vorticity sheet (cyan) and wing tip vortex (purple)

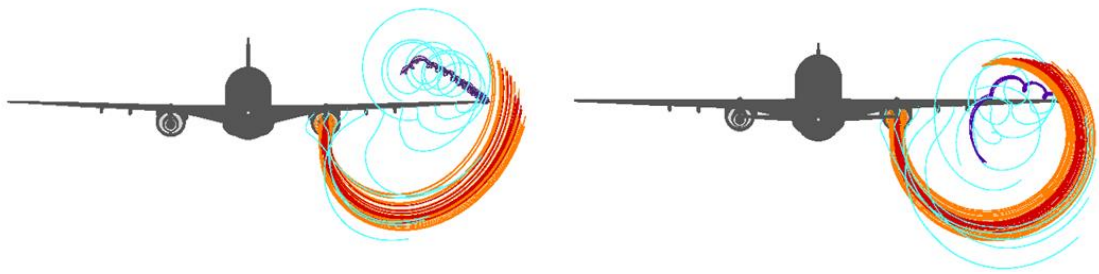

Figure 47. Streamlines for the landing (left) and climbing (right) configurations: core flow (red), bypass flow (orange), vorticity sheet (cyan) and wing tip vortex (purple). View from behind

The Figure 48 and Figure 49 present the same streamlines respectively for the landing and climbing configurations from a side view. An illustrating ground, which is not simulated, is added in the figures to represent a real situation. A green line represents the direction of the upwind flow from the wing tip. In both figures, the exhaust flow is initially following the direction of the plane and follows then the direction from the upwind flow after few spans behind the plane. The exhaust flow interacts then with the wing tip vortex which explains its raise after around 300 m for the landing configuration and 200 m for the climbing configuration. This interaction affects also the shift of the wing tip vortex. The wing tip vortex goes down from 11 m for the landing configuration and 18 m for the climbing configuration when it gets to the box boundary, corresponding to a distance of around 860 m.

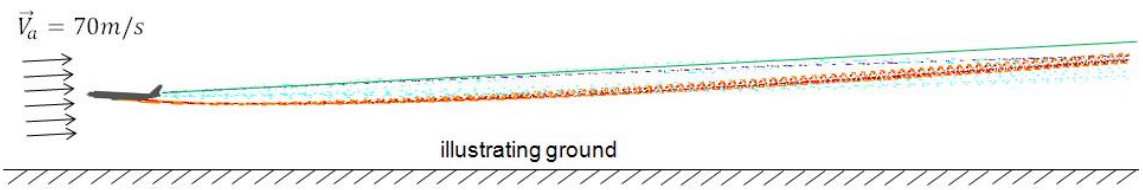

Figure 48. Streamlines for the landing configuration: core flow (red), bypass flow (orange), vorticity sheet (cyan) and wing tip vortex (purple). Side view with an imaginary illustrating ground

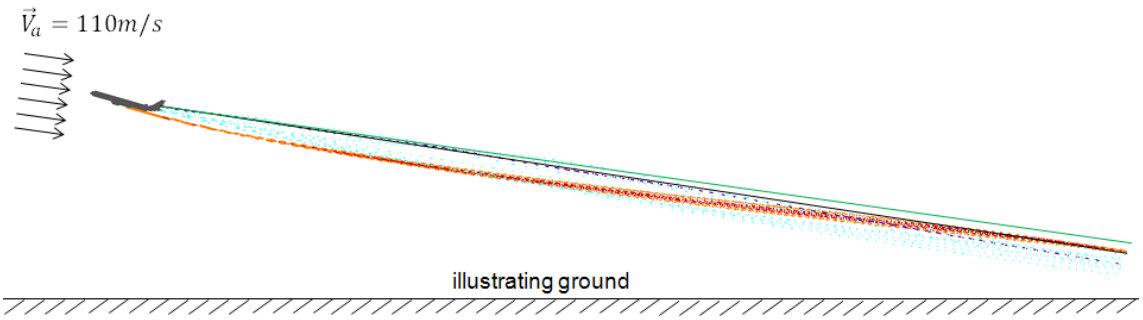

Figure 49. Streamlines for the climbing configuration: core flow (red), bypass flow (orange), vorticity sheet (cyan) and wing tip vortex (purple). Side view with an imaginary illustrating ground

The circulation Γ due to the aircraft is calculated in several planes by integration of the vortex vector $\vec{\omega}$ defined by:

$$\vec{\omega} = \overrightarrow{rot}\vec{V}. \tag{21}$$

If we consider that the upwind flow follows the $\vec{x}$ axis, the circulation Γ is then defined by [27] :

$$\Gamma = \iint_{y,z} \left(\frac{\partial V_z}{\partial y} - \frac{\partial V_y}{\partial z} \right) dydz. \tag{22}$$

The Figure 50 presents the circulation behind the aircraft for the two configurations. In both cases, some fluctuations are observed for all the meshes, and decrease with the number of mesh adaptation. Those fluctuations may be due to some interpolation errors as the circulation is calculated in planar cuts in a strongly anisotropic the mesh. Another explanation would be that both the mesh and the simulation are not perfectly adapted. Those fluctuations remain small for the late meshes, with a maximum of 2 %. For both cases, ignoring the slight fluctuations, one can observe a conservation of the circulation as the wing tip vortex is convected downstream. The circulation is around 250 m²/s² for the landing configuration and 510 m²/s² for the climbing one. For an aircraft, the theoretical circulation can be deduced from the lift force F_L:

$$\Gamma = \frac{F_L}{b\rho_a \|\vec{V}_a\|}, \tag{23}$$

with b the wing span. Another estimation is possible by assuming the aircraft in cruise regime can be approximated as an elliptically loaded wing [28][30][29]:

$$\Gamma = \frac{m_{aircraft} g}{B_0 \rho_a \|\vec{V}_a\|}, \tag{24}$$

with $m_{aircraft}$ the mass of the aircraft and B_0 the vortex spacing defined by:

$$B_0 = \frac{\pi}{4} b. \tag{25}$$

For an A350 aircraft, the total mass is respectively estimated to 200 tons and 240 tons for landing and climbing configurations. By applying the relations (24) and (25), one can obtain $\Gamma = 513\ m^2/s^2$ and $\Gamma = 457\ m^2/s^2$ respectively for the landing and climbing configurations. The circulation calculated with CEDRE simulations thus is lower for the landing configuration and higher for the climbing configuration. This result is expected as the formula (24) is an approximation for cruise regime, when lift is balancing the weight, which is not the case for landing and climbing regimes.

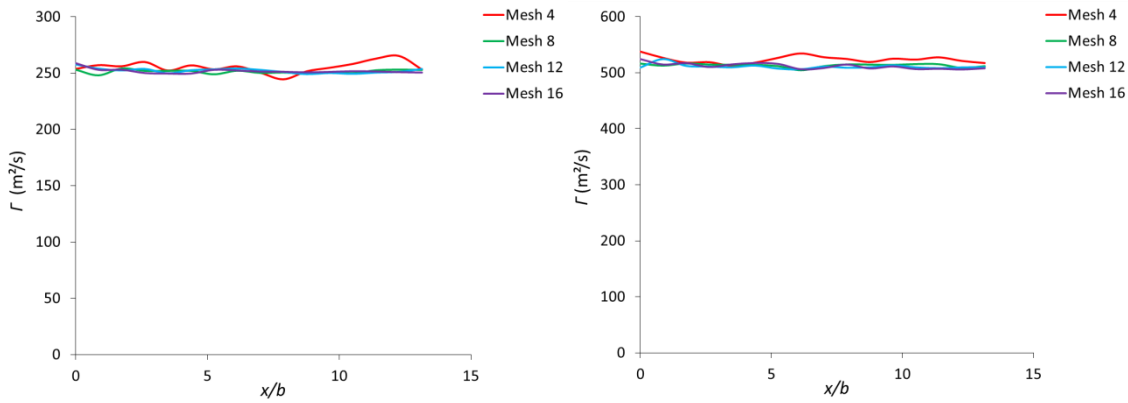

Figure 50. Circulation versus normalized distance behind the engine for the landing (left) and the climbing (right) configuration

The wing tip vortex descent velocity $V_{descent}$ can be theoretically calculated from the circulation with the following relation [30]:

$$V_{descent} = \frac{2\Gamma}{\pi^2 b}. \tag{26}$$

As the circulation is close to 250 m²/s² for the landing configuration and 510 m²/s² for the climbing configuration, the theoretical vortex descent velocity is around 0.88 m/s for the landing configuration and 1.79 m/s for the climbing configuration. Over the domain of simulation, the simulated vortex descent speeds are 0.95 m/s and 2.32 m/s for landing and climbing configurations, respectively, which compared well with the theoretical values. The evolutions of the position of the wing tip vortex center versus time for both configurations are presented in Figure 51.

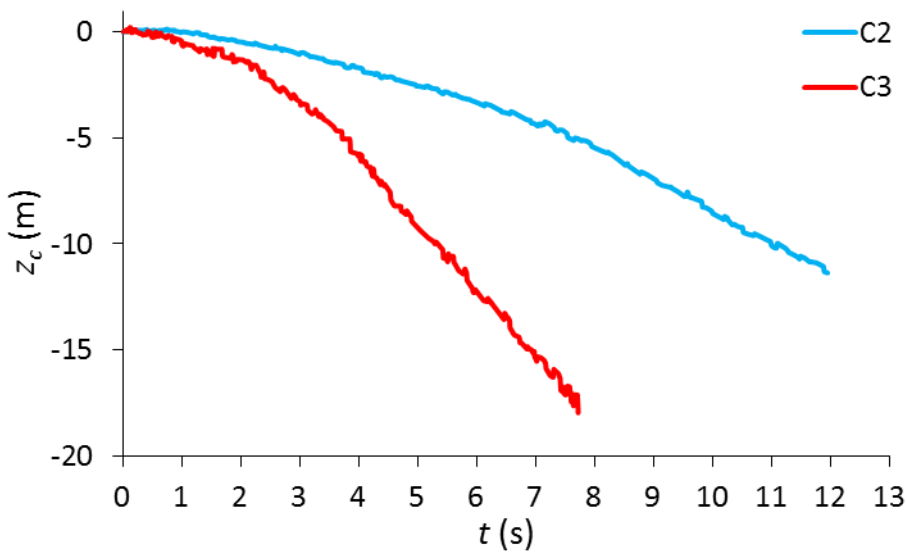

Figure 51. Vertical position for the wing tip vortex versus time for the landing (C2) and climbing (C3) configurations

Another quantity used to check the good quality of the mesh is the vortex radius. When convected downstream, this radius must remain in the same order of magnitude than the mean chord of the aircraft to be assured that the numerical dissipation due to the mesh remains negligible. For the A350 aircraft, the mean chord length of the wing is around 7 m. The evolution of the vortex radius for all complexities is presented in the Figure 52. For each case, the vortex radius is calculated in transversal cuts every meter behind the aircraft. For each planar cut, the maximum of the vorticity magnitude is spotted and corresponds to the vortex center. The radius

is calculated by measuring the distance between this vortex center and the position of the maximum of azimuthal velocity. For the initial mesh, the calculated vortex radius is strongly fluctuating and and is much higher than the mean chord, which shows that the initial mesh is not able to correctly model the wing-tip vortex transport. When $c = 32000$, the growth of the wing tip vortex is slowed down. Some fluctuations persist due to interpolation approximations. For $c = 50000$ and $c = 75000$, the wing-tip vortex radius linearly increases with the distance behind the aircraft with the same slope. At the largest distances behind the aircraft, the wing tip vortex radius is around 6 m for the landing configuration and 8 m for the climbing configuration. For both cases, the vortex radius is close to the mean chord for large distance behind the aircraft, which indicates that the vortex is not strongly dissipated by numerical effects.

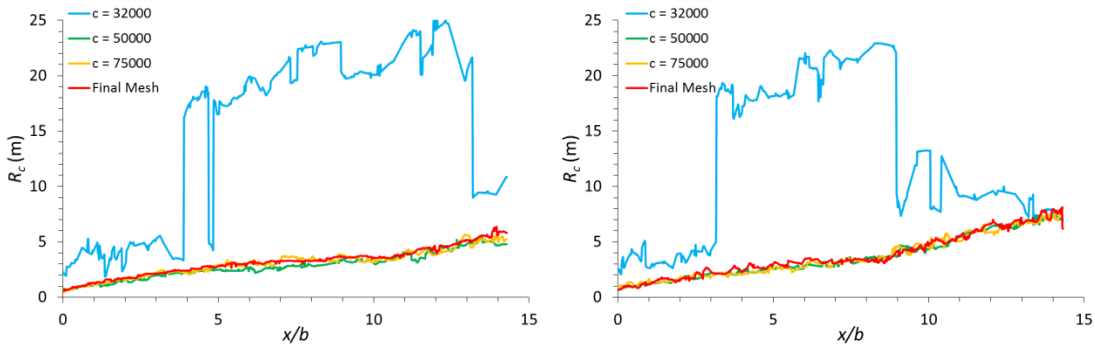

Figure 52. Wing tip vortex radius versus normalized distance behind the engine for the landing (left) and the climbing (right) configuration

As noticed in the part 3.3, it is important to calculate the characteristic time of the exhaust flow to evaluate the validity of the steady RANS simulations. The physical time from the point of view of the exhaust flow t_{core} is defined by:

$$t_{core} = \int_0^x \frac{1}{V_{core}(x)} dx. \tag{27}$$

When the exhaust flow gets to the end of the box, 10.7 s and 6.8 s have passed for respectively the landing and the climbing configurations. It is then reasonable to consider that during this time, the ambient conditions remains constant even if the plane is going up or down.

Figure 53 presents the dilution versus the physical core time on a streamline from the core to the end of the box for all configurations and for their thrust-equivalent for the engine-only configuration (all in colors) copy on the original graphic in black and white from [31] . The simulated exhaust time can be far higher for the engine-only configuration (around 300 s) than for the two other configurations due to low upwind speed (3 m/s). The dilution is higher as the thrust increases which is due to a stronger mixing. For a constant thrust, it seems that for both landing and climbing configurations, the dilution tends to follow the same trend that for their thrust-equivalent for the engine-only configuration at comparable physical core time. A simulation with a larger box to simulate higher physical core times could confirm this tendency. All simulated dilutions show a good agreement with the experimental data from [31]. It is important to note that those experimental data are extracted during the cruise phase, which shows that the dilution seems to be more impacted by the thrust than by the flight ambient conditions (e.g. Altitude, pressure, temperature).

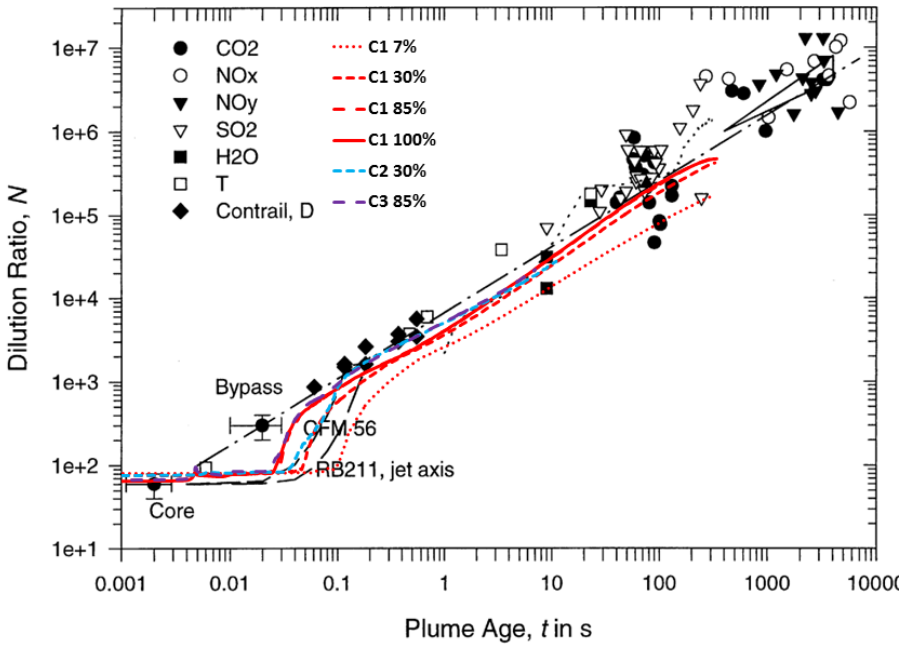

Figure 53. Dilution versus physical core time for all configurations

PART 2: AIR QUALITY MODEL LASPORT

1. Model system

Based on experiences with the application of the Lagrangian dispersion model LASAT (particle model according to the German standard VDI 3945 Part 3) at airports in Germany and Switzerland, LASPORT (LASAT for Airports) was developed in 2002 on behalf of the Federal German Airports Association (ADV) as a standard tool for emission and dispersion calculations. The program system is available as a commercial software package since 2003 and has been applied since then by various European airports and in various national and international projects.

LASPORT was approved for use by ICAO/CAEP (ICAO Environmental Report 2010) and it complies with the ICAO document 9889 (Airport Air Quality Manual).

Aircraft traffic is defined either based on general traffic information (scenario calculation) or by means of a movement journal with individual aircraft movements (monitor calculation). Monitor calculations allow a detailed study of actual aircraft traffic. Scenario calculations are well suited for prognosis calculations for which no detailed traffic information is available.

In a monitor calculation, individual emission strengths per movement and LTO phase and individual profiles can be applied: user-defined values, certification values based on the ICAO engine emission databank and LASPORT default profiles, or performance-based values and profiles derived by the integrated performance model ADAECAM (based on PIANO profiles).

Figure 54 shows the functionalities provided by LASPORT.

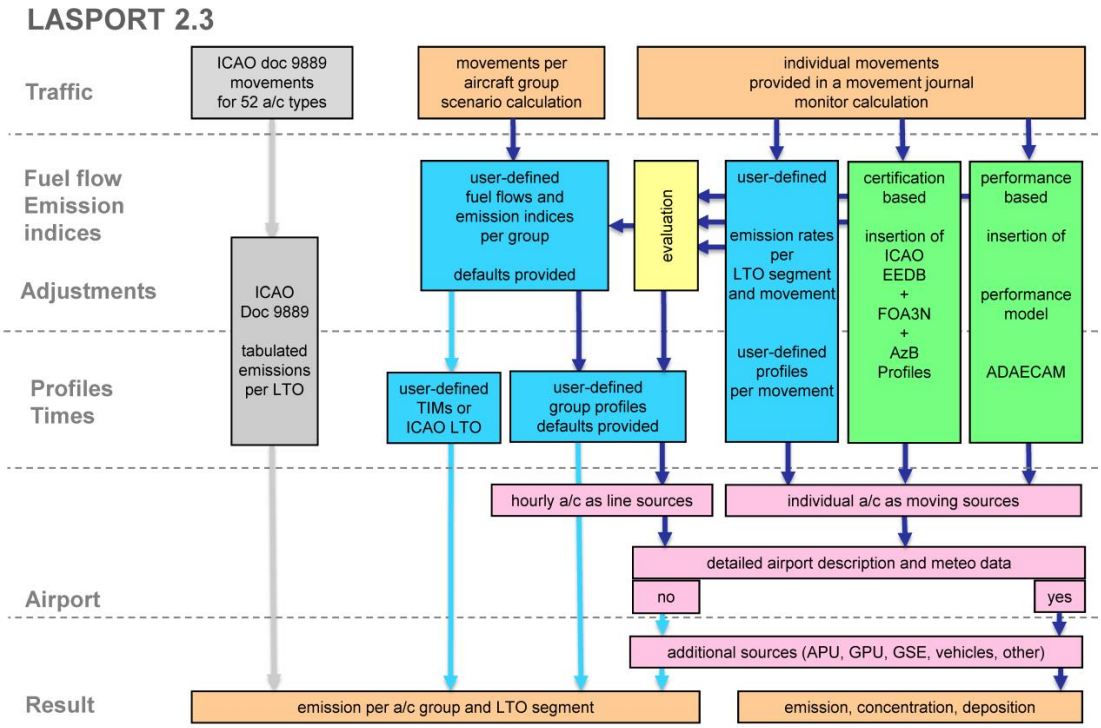

Figure 54: Functionalities provided by LASPORT.

2. Exhaust dynamics

Pollutants are emitted from aircraft engines not in a passive way, but in an exhaust that has an excess momentum and temperature with respect to the ambient air. This exhaust dynamics has a strong influence on the pollutant dispersion in the near field of the aircraft.

Different airport dispersion models have different approaches to account for the effects of exhaust dynamics. In LASPORT, exhaust dynamics can be accounted for in a quite direct way as the underlying dispersion model is a Lagrangian particle model: A directed excess velocity and velocity fluctuations is given to the emitted simulation particles, very similar to the true engine exhaust. However, details of the complex flow field cannot be modelled and thus a somewhat pragmatical approach is required that yields realistic concentrations from some distance of the engine on (some 10 m or so).

The parameters provided by the Lagrangian particle model LASAT and applied by LASPORT in default calculations to account for exhaust dynamics of aircraft main engines are:

- Sh, initial horizontal cross velocity fluctuations
- Sl, initial longitudinal velocity fluctuations
- Sv, initial vertical velocity fluctuations
- Ve, initial directed exit velocity
- Ts, decay time of Sh, Sl, Sv, Ve
- Dh, horizontal source extent
- Dv, vertical source extent
- Ss, vertical source shift

These parameters are defined as a function of aircraft category and LTO mode, where LASPORT uses 6 modes:

- AF, Approach Final, final approach to touch-down#

- AG, Approach ground, touch-down to roll-off
- ID, Idle, ground taxiing
- TG, Take-off Ground, start take-off to lift-off
- CI, Climb Initial, lift-off to thrust cut-back
- CF, Climb Final, final climb

The horizontal source extent accounts for the typical engine separations and uncertainties in the location of the taxiways. The vertical extent accounts for near field effects and to some extent for plume rise in a conservative manner. The shift accounts for the down-shift due to the influence of wing vortices in the LTO phases AF, CI, and CF. The decaying exit velocity and velocity fluctuations account for momentum and turbulence effects of the emitted exhaust plume behind the moving aircraft.

Plume rise is accounted for in a more conservative way by means of the vertical velocity fluctuations that yield an increased vertical spread of the pollutant plume instead of a lift-off of the plume from the ground.

The parameter values were set up in the past (LASPORT 2.3) by means of DOAS measurements at Dusseldorf Airport, comparisons with the 3-dimensional plume rise model PLURIS and with literature. In this project, additional experimental data sets (Zurich Airport and measurements from WP3 at Ciudad Real Airport) were used to enhance the parametrisation (LASPORT 2.4).

3. Experimental data sets

3.1. DOAS measurements at Düsseldorf Airport

Düsseldorf Airport maintains several DOAS measurement devices that are located in the vicinity of the runway thresholds. In the year 2000, a measurement campaign was carried out, recording the NO signal from individual aircraft starts.

A DOAS track was located about 350 m behind the runway threshold (red line in Figure 55). The line-integrated NO concentration was recorded every 15 seconds for individual departures from runway 05R of aircraft with known type and engine. Video recordings of the aircraft supported the measurements, in particular yielding information on the exact start position (a, b, c, d). The background concentration was subtracted by means of measurements from a second DOAS device at the opposite runway threshold. Meteorological data from a supersonic anemometer device were available in form of successive minute averages.

The measurement data were compiled to 35 formatted data sets, one for each individual departure. An example is shown in Figure 56. All data sets are available as formatted data files. The set can be used to check and calibrate the turbulence parameters that are applied in aircraft dispersion calculations to account for the dynamics of the engine exhaust at ground take-off.

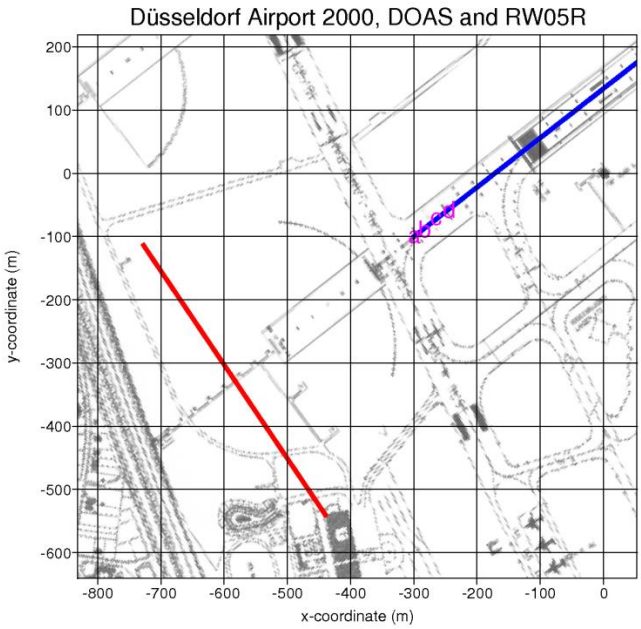

Figure 55: Düsseldorf Airport with the DOAS track (red line), the departure runway RW05R (blue line), and the different start positions a to d.

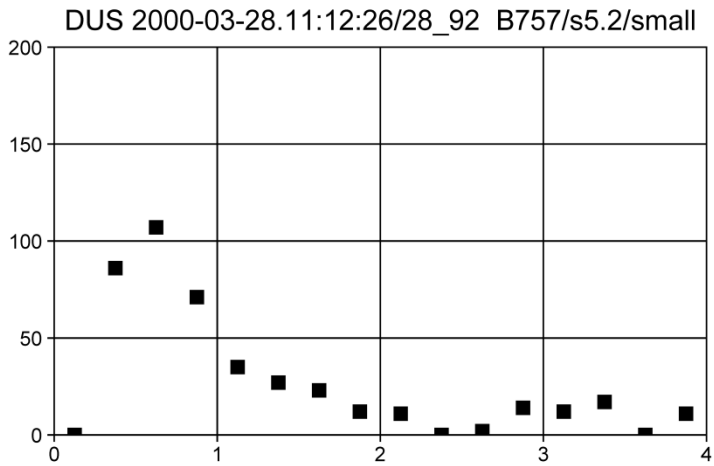

Figure 56: Measured mean NO concentration across the DOAS line. Time runs over 4 minutes after start of a B757.

3.2. Approach measurements at Zurich Airport

At distances between 1.8 km and 10.3 km from the approach runway 14 and below the arrival corridor, time resolved UFP measurements were carried out at Zurich airport in 2019 [32].

The following focusses on the results at station 101 northwest of runway 14 (see Figure 57) with an overflight height of 111m and a distance to the runway of about 1800 m. For calm wind conditions, high UFP concentration peaks were observed. Figure 58 shows part of the measured UFP time series, also indicated are the overflight times and types of the aircraft. The authors deduce that at station 101, on average, about 14 % of the measured number concentration due to aircraft can be attributed to non-volatile PM.

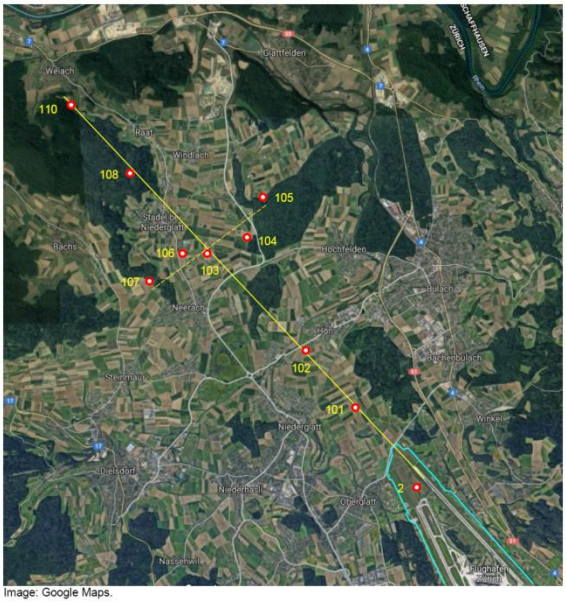

Figure 57: Locations of the measurement stations along the arrival corridor of runway 14 at Zurich airport. Figure taken from the Zurich report.

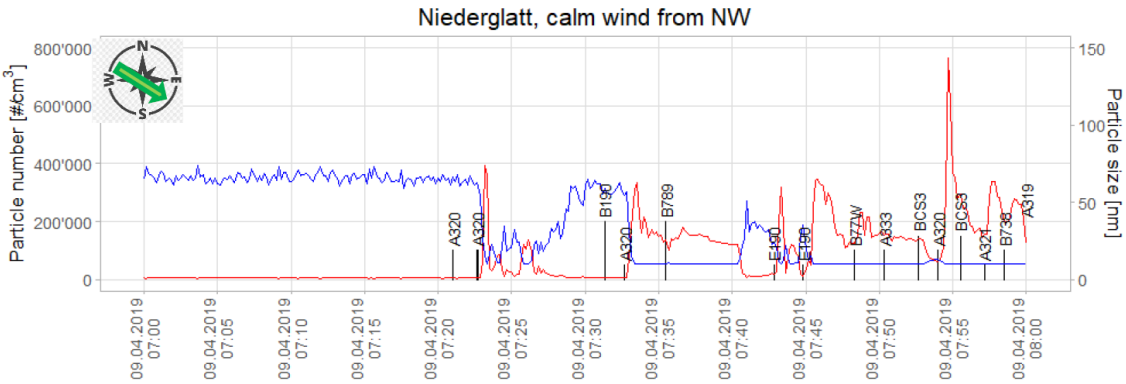

Figure 58: Measured UFP concentration and mean particle diameter at station 101, also indicated are the overflight times and aircraft types. Figure taken from the Zurich report.

For a more detailed evaluation, the following focusses on the first two overflights of 2019-04-09, which are two aircraft of type A320 with engine type CFM56-5B4/3. Figure 59 shows the measured concentration time series (green, 10-second means) and the approximate overflight times (red). The data were kindly provided by the authors.

The time difference between the two overflights is about 90 s. The first, very pronounced concentration peak with a height of about 400 000 1/cm³ and a width of about 20 s occurs about 140 s after the first overflight. It is followed by two smaller peaks with heights of about 100 000 1/cm³, widths of about 30 s, and a separation of approximately 90 to 100 s.

It is instructive to carry out some plausibility checks to better understand the observations. If the UFP puff would be emitted passively at height 111 m in calm conditions, atmospheric dispersion would increase the puff size, eventually leading to a signal at the ground. However, in this case one would expect a much smoother variation of the signal in time.

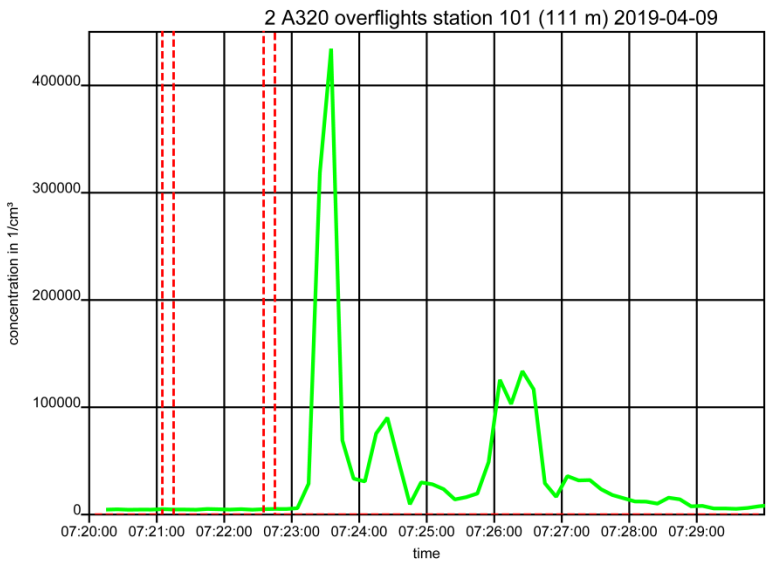

Figure 59: Measured concentrations of UFP (10-second means) in the morning of 2019-04-09 at station 101 (green). Also indicated are the overflight times (red) of the two aircraft of type A320.

Transport of the emitted puff downward by the influence of wing vortices is a more reasonable explanation, if one assumes that the vertical momentum is flipped at the ground, thereby transporting the puff quickly away again from the measurement location and causing a high but short concentration signal.

How does a peak number concentration of 400 000 1/cm³ relate to typical emission rates and plume dimensions: The distance flown by the aircraft at approach in 10 s is about 600 m. The cross section of the combined exhaust plumes of the two engines of the A320, after some mixing due to turbulence, is probably of the order of 200 m² (20 m width and 10 m height). This gives an effective volume of 120 000 m³ in which the UFP emitted during 10 seconds are distributed.

If there is negligible atmospheric dilution and if one assumes that the concentration plume is transported directly downward to the measurement device by wing vortex interaction, this would yield the highest possible signal. Using an emission index (engine UID 01P08CM105) for non-volatile UFP of 3.49e14 /kg, a fuel flow of 2 × 0.316 kg/s and a factor 7 for the ratio total/non-volatile PM, this gives an UFP number of 1.5e16 emitted in 10 s. The resulting concentration in the assumed 10 s volume is 1.5e16/120 000 = 1.25e11 1/m³ or 125 000 1/cm³. This is considerably lower than the observed first peak, even if one assumes that there is no further dilution during the 140 s of vertical transport to the ground.

The high and short shape of the first concentration peak seems different from the following two ones. In addition, the time difference between the first peak and the second or third one does not match well with the time difference of the two overflights. Possible explanations of the first pronounced concentrations peaks are thrust changes of the aircraft engines concomitant with a high emission burst, or re-suspension of UFP from the ground for the first morning vortex that touches the ground. The latter is less likely because there was some small amount of precipitation during the overflights.

3.3. Plume measurements at Ciudad Real Airport (WP3)

In course of WP3, measurements behind an A340 aircraft with installed engines were carried out at a taxiway of the airport Ciudad Real for some days in summer 2021 (mainly June 28) and some days in winter early 2022 (between January 21 and 26).

There were two stationary measurement equipments separated by 50 m (near field and far field) and the aircraft distance to the near-field equipment was changed in intervals of typically 50 m by moving the aircraft towards west on the taxiway. Hence, measured concentrations were available in steps of 50 m relative to the aircraft engine number 3.

Figure 6 shows the locations of the two stationary measurement equipments and of the operating engines 2 and 3 at different distances. The taxiway is oriented approximately 13 deg with respect to direction east/west, the aircraft nose is oriented westwards, a wind direction of 283 deg corresponds to head wind.

The aircraft engine was run in different thrust conditions, in particular at thrusts corresponding to the certification values 7 %, 30 %, and 80 % (85 % or higher was technically not feasible). In most of the cases, engine number 2 was running at the same thrust as engine 3 to avoid torque forces.

Measured trace substances include UFP, NOx, and CO_2. Also fuel flows and fuel compositions were recorded. In addition to the measured concentrations, effective emission indices of non-volatile particle mass and number were derived from the concentrations. A more extensive description and evaluation of the measurements and the large data sets taken can be found elsewhere.

Meteorological data were recorded by nearby low-cost sensors (LCS) and by the airport (CRIA). However, there were some ambiguities with respect to the definition of wind direction and averaging times (LCS) and with respect to measurement heights and granularity of the data (CRIA).

A subset of the measured data was prepared by the measurement team and provided in averaged form of an XLS file (Version 11, unfiltered average data). Details on the data preparation process can be found elsewhere. From this data set a further subset was extracted and converted for use in the model comparisons. This conversion includes:

- Addition of meteorological data from the LCS (temperature, pressure, wind speed, wind direction) and CRIA (wind speed and wind direction) ;
- Conversion of gas concentrations reported in ppmv to mass concentrations using the LCS values of temperature and pressure ;
- Addition of approximate background concentrations of particle number (3000 1/cm3 in summer, 6000 1/cm³ in winter), CO_2 (420 ppm), and NOx (20 ppb) from the LCS data ;
- Conversion of units.

The result was a formatted CSV file suitable for further processing in the context of modelling. It contains 59 data rows with the averaged results for each measurement and the following columns:

Date	Date of the measurement in format DD.MM.YYYY
t1(LOC)	Start time of the measurement (local time) in format HH:mm
t2(LOC)	End time of the measurement (local time) in format HH:mm
thrust-3(%)	Thrust of engine 3 in percent.
thrust-2(%)	Thrust of engine 2 in percent.
d-near(m)	Distance of the near field measurement equipment to engine 3
d-far(m)	Distance of the far field measurement equipment to engine 3.
T(C)	Temperature in degree Celsius
p(Pa)	Pressure in Pa.

ws-LCS(m/s)	Wind speed at 2 m height from the LCS in m/s.
wd-LCS(deg)	Derived wind direction at 2m height from the LCS in deg (0: wind from North, 270: wind from West).
ws-CRIA(m/s)	Wind speed at (assumed) 10 m height from CRIA in m/s.
wd-CRIA(deg)	Wind direction at (assumed) 10m height from CRIA in deg (0: wind from North, 270: wind from West).
FF(kg/s)	Fuel flow of one engine in kg/s.
FHC(1)	Fuel water content (mass fraction).
FSC(1)	Fuel sulfur content (mass fraction).
nvPN-EI-near(1/kg)	Number emission index of non-volatile PM derived from the near field measurement in 1/kg.
nvPM-EI-near(1/kg)	Mass emission index of non-volatile PM derived from the near field measurement in mg/kg.
nvPN-near(1/cm3)	Loss-corrected number concentration of non-volatile PM from the near field measurement in 1/cm³.
nvPM-near(ug/m3)	Loss-corrected mass concentration of non-volatile PM from the near field measurement in µg/m³.
nvPM-EGMD-near(nm)	Electric mobility diameter of non-volatile PM from the near field measurement in nm.
nvPM-EGSD-near(1)	Geometric standard deviation of the electric mobility diameters of non-volatile PM from the near field measurement.
CO2-near(mg/m3)	CO_2 concentration from the near field measurement in mg/m³.
NOX-near(ug/m3)	NOx concentration from the near field measurement in µg/m³.
nvPN-far(1/cm3)	Loss-corrected number concentration of non-volatile PM from the far field measurement in 1/cm³.
PN-far(1/cm3)	Loss-corrected total number concentration from the far field measurement in 1/cm³.
nvPM-far(ug/m3)	Loss-corrected mass concentration of non-volatile PM from the far field measurement in µg/m³.
CO2-far(mg/m3)	CO_2 concentration from the far field measurement in mg/m³.
nvPM-GMD-far(nm)	Geometric mean diameter of non-volatile PM from the far field measurement in nm.
PN-back(1/cm3)	Estimated background number concentration of PM in 1/cm³.
CO2-back(mg/m3)	Estimated background concentration of CO_2 in mg/m³.
NOX-back(ug/m3)	Estimated background concentration of NOx in µg/m³.

The following figures show some main results of the measurements. Note that the symbols of one type do not indicate simultaneous measurements, but separate measurements at separate times with separate meteorological conditions. The results are plotted separately for the summer and the winter campaign.

Data are plotted against the distance from engine 3. Circles denote results for 7% thrust, triangles results for 30%, and squares results for 80% (mnemonic: the higher the thrust, the more corners). Symbols in magenta colour denote results from the near field measurement, symbols in orange colour form the far field measurements. The symbols for the different thrust settings are slightly shifted to a smaller or larger distance for a better readability. Measurements for January 25 are depicted with smaller symbols, because this day showed strong cross winds which make the data more difficult to interpret.

In this and subsequent model evaluations, NOx was not considered because of missing measurement-based emission indices and because of mostly negative LCS background data. Here are the different titles of the different figures discussed in the previous paragraph:

- Figure 60: CO_2 concentration ;
- Figure 61: Mass concentration of non-volatile PM ;
- Figure 62: Number concentration of non-volatile PM ;
- Figure 63: Fraction of total number concentration and number concentration of non-volatile PM from the far field measurements ;
- Figure 64: Electric mobility diameter of non-volatile PM from the near field measurements.

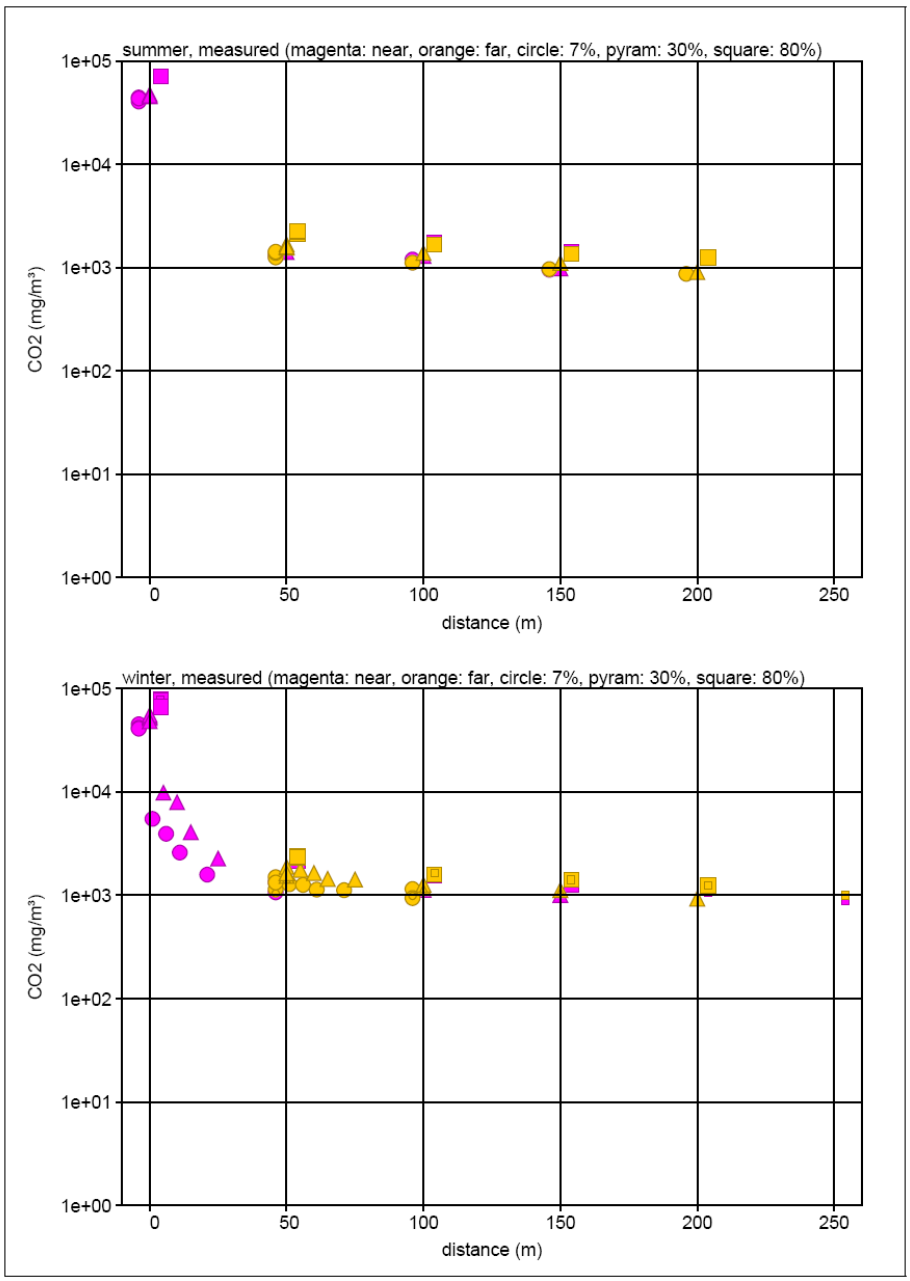

Figure 60: CO_2 concentration as a function of distance from engine 3.

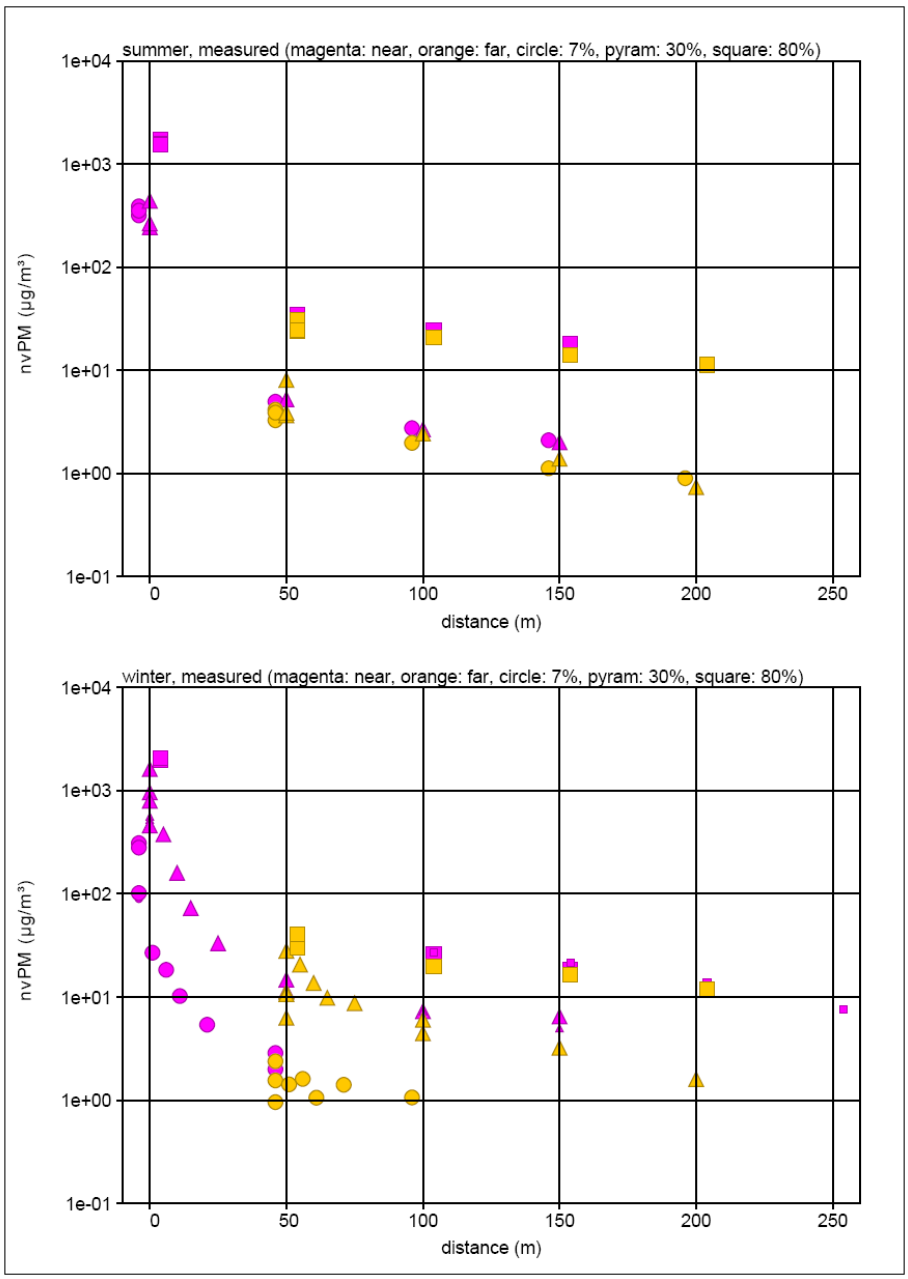

Figure 61: Mass concentration of non-volatile PM as a function of distance from engine 3.

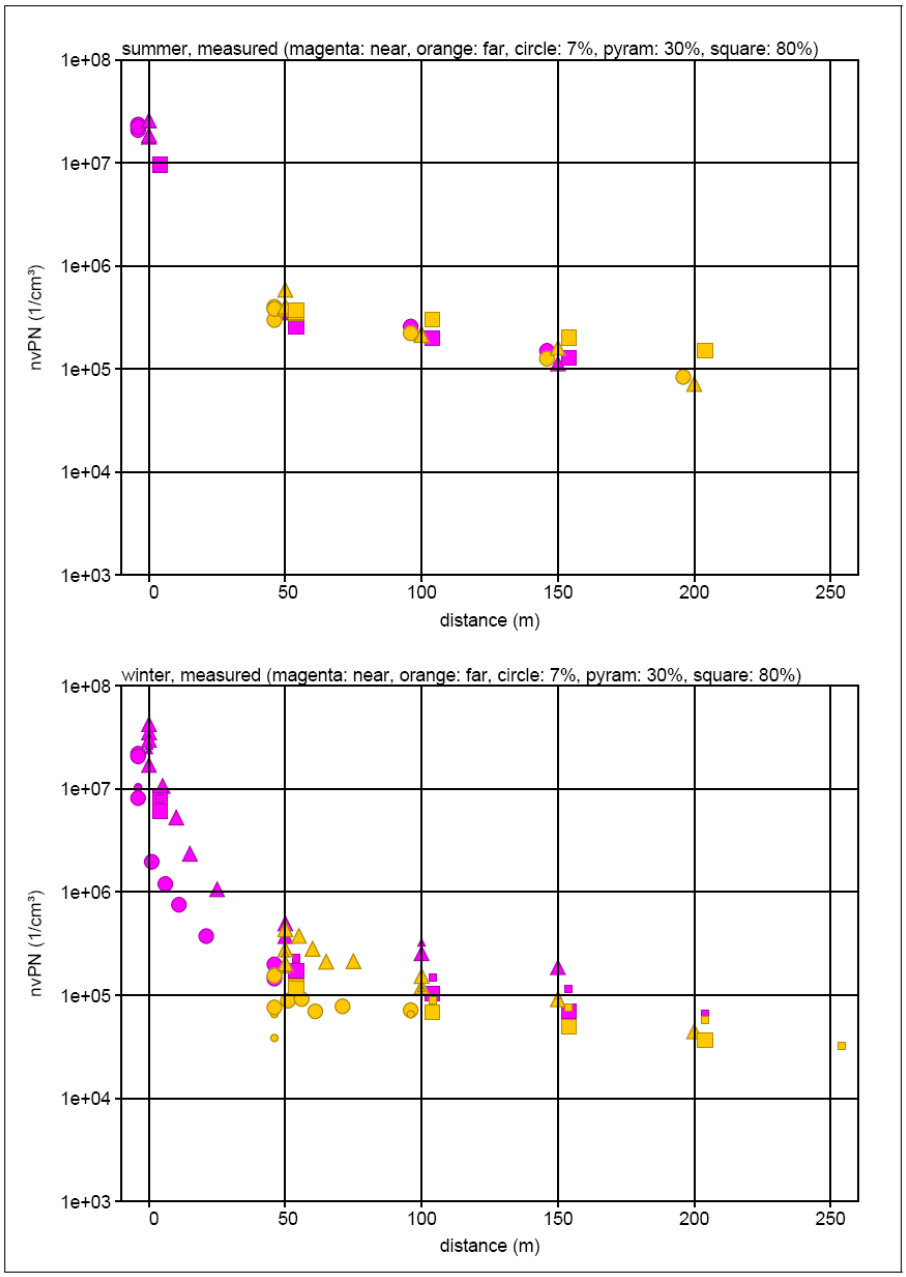

Figure 62: Number concentration of non-volatile PM as a function of distance from engine 3.

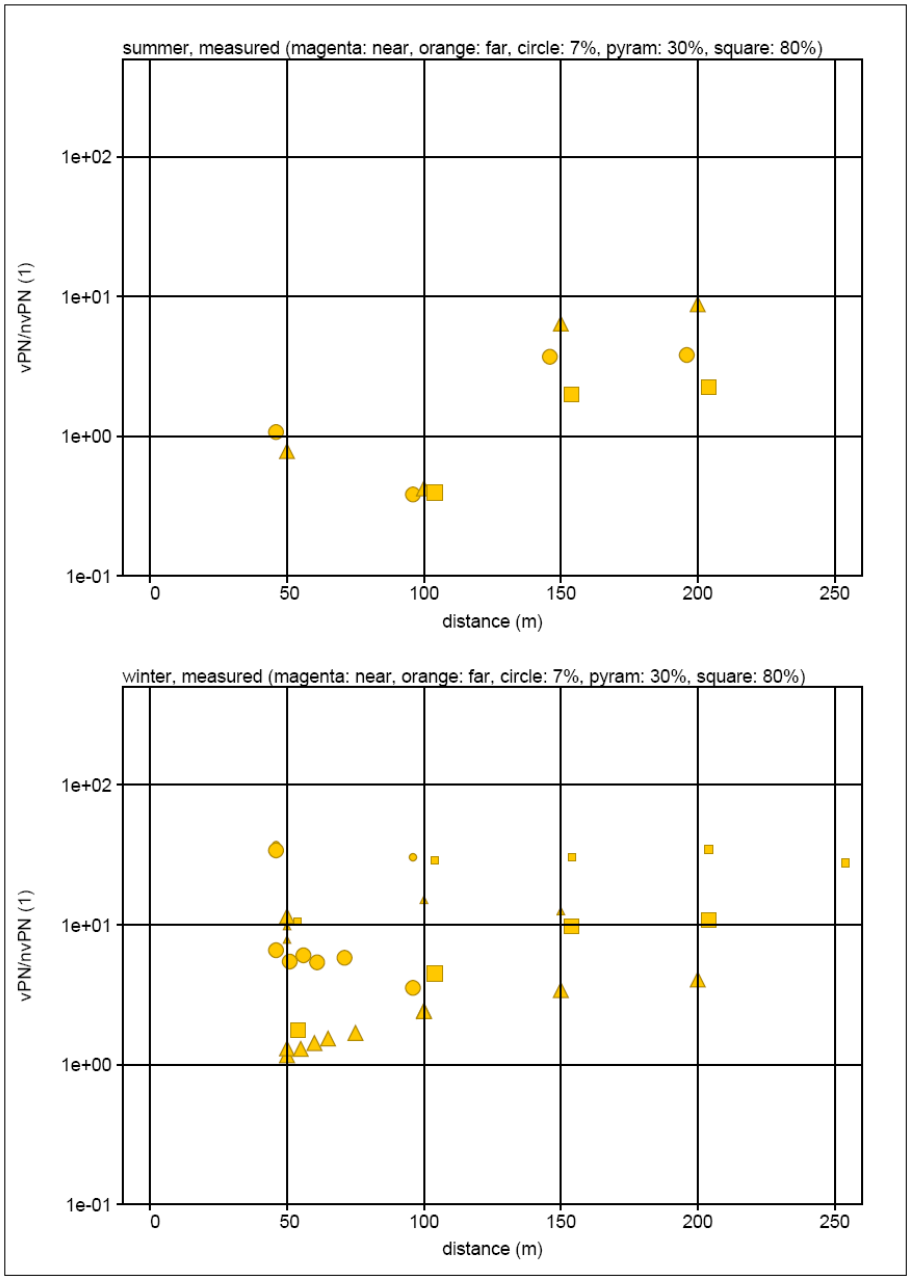

Figure 63: Fraction of total number concentration over number concentration of non-volatile PM as a function of distance from engine 3.

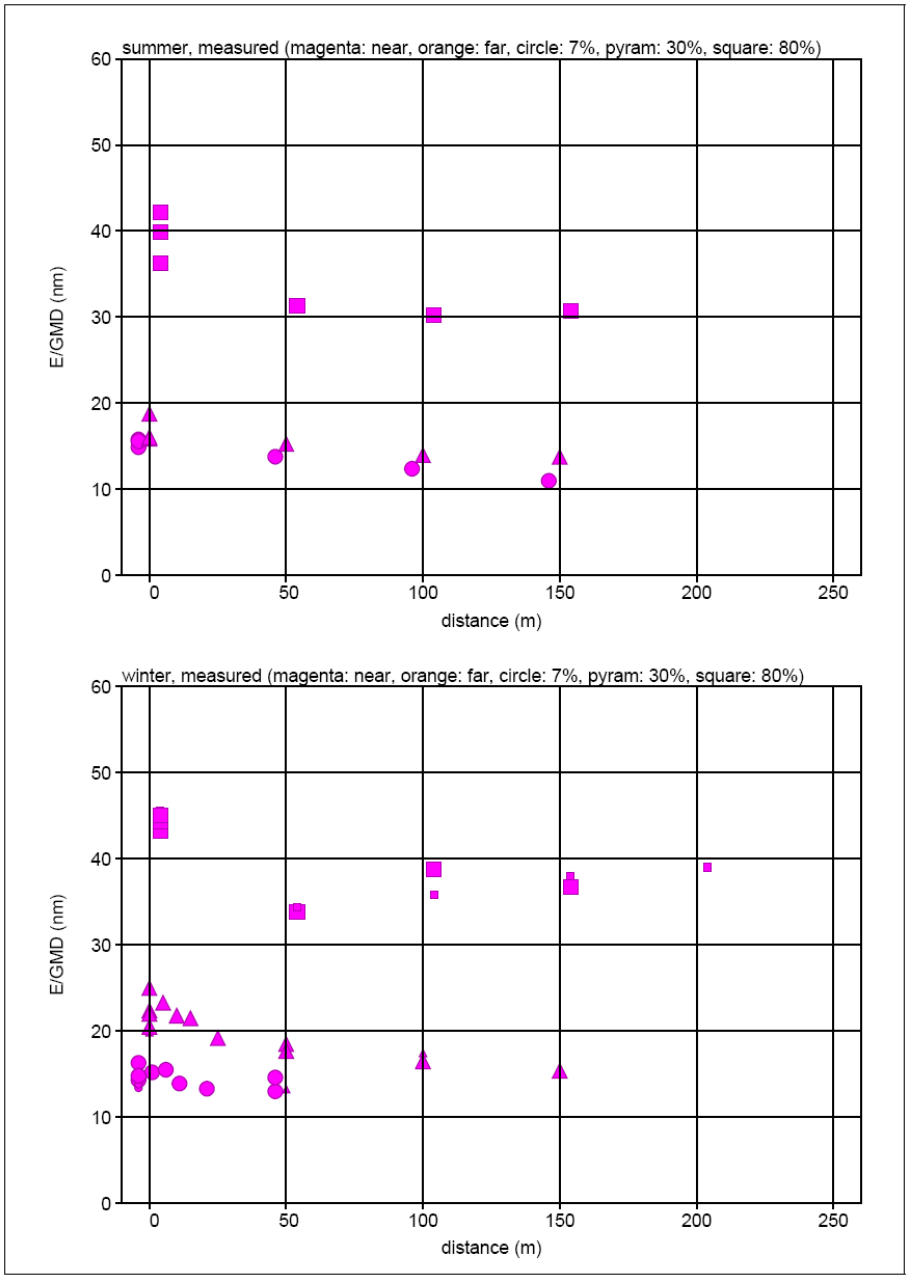

Figure 64: Electric mobility diameter of non-volatile PM as function of distance from engine 3.

4. Enhanced parametrisation of exhaust dynamics

The model parameters provided by LASAT/LASPORT to account for exhaust dynamics set certain constraints and limitations. For example, excess velocities assigned to the simulation particles decay with a fixed time constant, whereas plume rise models like PLURIS show that the velocity decay in the engine exhaust is described by a time constant that becomes larger with increasing transport time.

In addition, the available data sets do not allow to calibrate and, in addition, to validate all of the applied parameters. Hence assumptions are required based on arguments of simplicity and plausibility.

Last but not least, different models have different means and constraints to account for exhaust dynamics and model developers may have different constraints and preferences. For example, in some airport dispersion models more focus is given to the buoyant rise of engine exhaust and in other models (like LASPORT) to the dynamical excess momentum and turbulence. Both approaches can be suited to explain experimental findings such as the deviation of exhaust concentration from the usual 1/u dependence (wind speed u).

Finally, model systems may need to incorporate national standards or elements of conservatism by which concentrations are rather over-predicted than unintendedly under-predicted.

Based on a variety of tests and parameter variations, the following considerations were applied to develop an enhanced parametrisation for LASPORT:

- As in LASPORT 2.3, it is assumed that the exhaust velocity is proportional to the square root of the thrust. In a simple physical picture, where thrust is the product of exhaust mass flow and exhaust speed, this assumption is strictly valid. It allows to derive velocities and velocity fluctuations from given thrust levels to other thrust levels and from given aircraft categories to other categories ;
- The aircraft categories are extended so that large, medium, and small aircraft are not bundled into one category. The new categories for jet aircraft are J1 (large), J2 (medium, small), J3 (regional, turboprop, business, piston). As a rough estimate it is assumed that the average thrust of aircraft in category J2 is 60 % of J1 and in J3 20 % ;
- At distances of about 1 km or more, there has been no indication in the past that LASPORT 2.3 systematically over- or under-estimates long-time concentrations like annual means. For long-time means, the vertical width of the airport plume is the relevant quantity, and it is determined (with respect to exhaust dynamics) by the product of decay time and vertical velocity fluctuations. Hence this product in the enhanced parametrisation should be similar as the one in the preceding parametrisation, in particular for the dominant group of small aircraft (A319, A320, etc.) and the LTO phase ID (taxiing) ;
- The decay constant of 240 s (4 minutes) in LASPORT 2.3 seems to be on the large side. To re-model the Zurich results, a decay constant of 100 s would be sufficient ;
- The ratio of horizontal to vertical velocity fluctuations was reduced to produce a more directed plume in the initial state, with better agreement with the measurements of WP3 ;
- For final approach (AP), an average sink velocity of v = 0.9 m/s for J1 is applied. This is consistent with the findings of the model simulations with CEDRE (see Part 3.4.2).
  For an averaging time taken from the Zurich results (T = 150 s) and the decay time Ts = 120 s, this demands an initial sink velocity of 1.6 m/s. For climb (CI, CF), twice the value is applied. In the input file, the downshift is applied as relevant parameter like before. From LASPORT 2.4 on, the sink velocity is then calculated as downshift divided by decay time. For AP and CI/CF, reduced velocity fluctuations are applied to account for the reduced dispersion in the vortex motion as compared to the ground dispersion for ID, AG, and TG. For the horizontal cross fluctuations, a reduction to 50 % and for the others are reduction to 20 % is applied.
- A directed exit velocity for J1 and TG is set to 12 m/s based on comparisons with the on-wing measurements. A higher value would reduce the agreement with the DOAS results. For approach, the velocity is directed horizontally and then the vertical sink velocity is added. For climb, the directed velocity is aligned with the aircraft climb direction and then the vertical sink velocity is added. For ID, half the resulting velocity is applied to account for the fact that taxiing is on average more effected by cross winds and enhanced plume entrainment as compared to arrival and departure segments which are (at least on average) more aligned with the wind direction.

Category J1 (aircraft group Large)

AF	AG	ID	TG	CI	CF	
Sh (m/s)	0.822	0.794	0.794	3.000	1.383	1.383
Sl (m/s)	0.822	0.794	0.794	3.000	1.383	1.383
Sv (m/s)	0.164	0.397	0.397	1.500	0.277	0.277
Ve (m/s)	6.573	3.175	1.587	12.000	11.063	11.063
Ss (m)	-192.000	0.000	0.000	0.000	-384.000	-384.000
Ts (s)	120	120	120	120	120	150
Dh (m)	40	40	40	40	40	40
Dv (m)	20	20	20	20	20	20

Category J2 (aircraft groups Medium, Small)

AF	AG	ID	TG	CI	CF	
Sh (m/s)	0.636	0.615	0.615	2.324	1.071	1.071
Sl (m/s)	0.255	0.615	0.615	2.324	0.428	0.428
Sv (m/s)	0.127	0.307	0.307	1.162	0.214	0.214
Ve (m/s)	5.091	2.459	1.230	9.295	8.570	8.570
Ss (m)	-148.723		0.000	0.000	0.000	-297.445
Ts (s)	120	120	120	120	120	120
Dh (m)	30	30	30	30	30	30
Dv (m)	15	15	15	15	15	15

Category J3 (aircraft groups Regional, Business, Turboprop, Piston)

AF	AG	ID	TG	CI	CF	
Sh (m/s)	0.367	0.355	0.355	1.342	0.618	0.618
Sl (m/s)	0.147	0.355	0.355	1.342	0.247	0.247
Sv (m/s)	0.073	0.177	0.177	0.671	0.124	0.124
Ve (m/s)	2.939	1.420	0.710	5.367	4.948	4.948
Ss (m)	-42.933	0.000	0.000	0.000	-85.865	-85.865
Ts (s)	60	60	60	60	60	60
Dh (m)	20	20	20	20	20	20
Dv (m)	10	10	10	10	10	10

5. Comparison with the experimental data sets

With the enhanced parametrisation, implemented into LASPORT 2.4, the measurements were re-run.

5.1. DOAS measurements at Dusseldorf Airport

Figure 65 shows the time course of measured and modelled concentration. The time courses of all evaluated take-off events are listed in Figure 66. Some graphs indicate that the measured concentrations were influenced by other sources not accounted for in the modelling, therefore some underestimation can be expected.

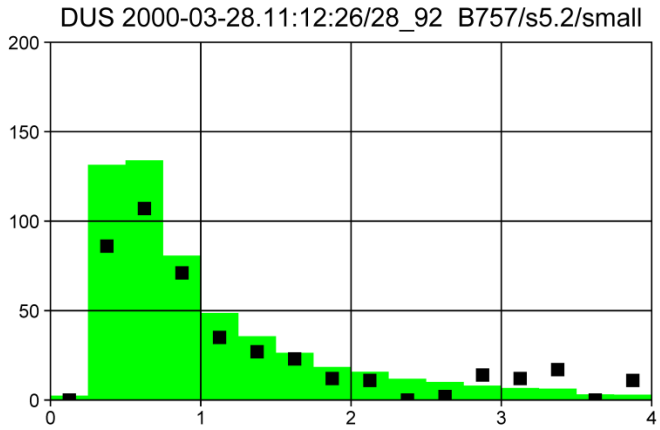

Figure 65: LASPORT 2.4: Comparison of measured (black squares) and modelled (green bars) mean NO concentration across the DOAS line. Time runs over 4 minutes after start of a B757.

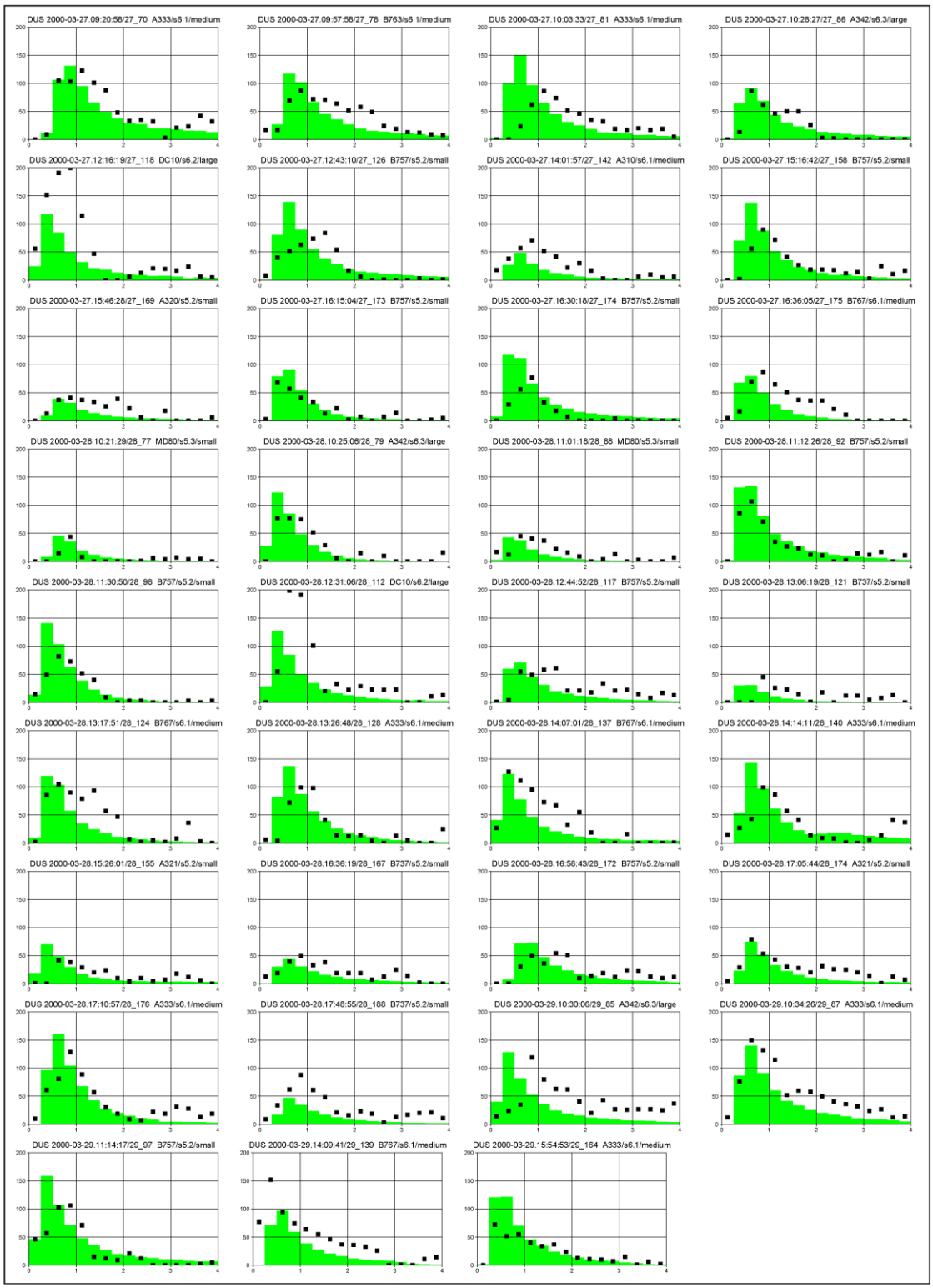

Figure 66: LASPORT 2.4: Time courses of measured (black) and modelled (green) concentration integrals for all evaluated take-off events.

5.2. Approach measurements at Zurich Airport

Figure 67 shows the measured and modelled concentration time series at station 101. The blue line denotes the model result with LASPORT 2.4. As discussed before, it seems not possible to reproduce the high first peak by standard modelling, but the other two peaks can be at reproduced at least in a qualitative way with LASPORT 2.4.

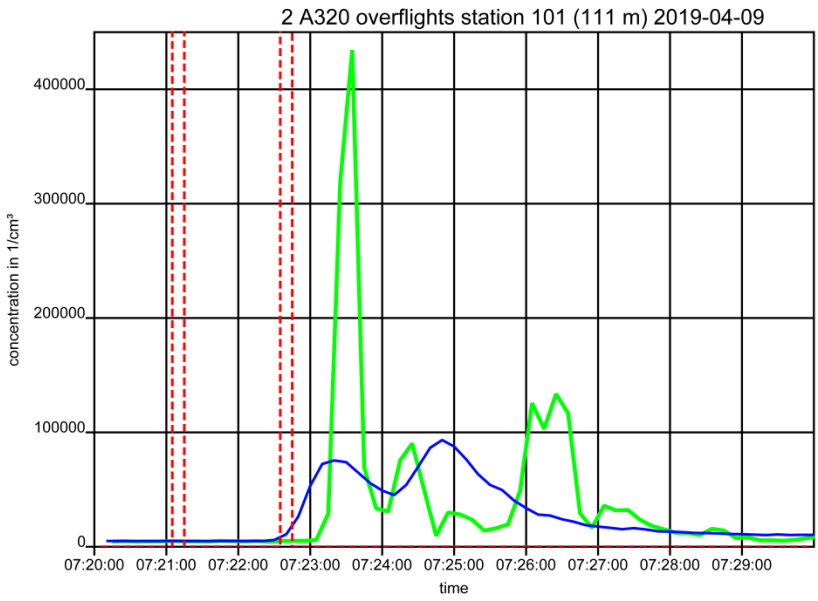

Figure 67: LASPORT 2.4: Measured and modelled UFP concentrations at monitor station 101. Green: measured. Blue: LASPORT 2.4 with dynamical downshift. Red: Indication of the two overflights over monitor station 101.

5.3. Plume measurements at Ciudad Real Airport (WP3)

The measurements at Ciudad Real were re-modelled with LASPORT. For each of the 59 measurement intervals, a separate calculation was carried out with the current meteorological conditions. The modelled concentration of the quasi-stationary plume was then recorded at the actual positions of the near field and the far field measurement equipments. To facilitate the calculation, a coordinate system aligned with the taxiway was applied and the wind direction was transformed accordingly.

The engines 2 and 3 were modelled as distinct sources with an initial extent of 3m in the horizontal and in the vertical. The emission rates were set according to the measured fuel flows and emission indices.

For the initialization of the atmospheric boundary layer model of LASPORT (profiles according to the German standard VDI 3783 Part 8), the CRIA data were applied because they seem to match better with global observation and because they are likely based on longer averaging times as compared to the LCS data. The surface roughness length was estimated with 0.1 m and the Obukhov length as a measure of atmospheric stability was set according to the standard VDI 3783 Part 8 to -36 m for the summer period (unstable stratification) and for the winter period except for January 25, and to -88 m (neutral to unstable stratification) for January 25. The more neutral value for January 25 was chosen because here the wind speed was quite high with values above 5 m/s, which is an indication for a more neutral stratification. Tests showed that the concentrations at the short distances studied here are not very sensitive to these assumptions.

For a comparison with the measurements, the values directly at the engine were not considered because LASPORT is not able to model and resolve dynamics at engine exit in an adequate way. The comparisons start at a distance of 50 m.

In the following graphs, circles denote results for 7 % thrust, triangles results for 30 %, and squares results for 80 % thrust (mnemonic: the higher the thrust, the more corners). In the plots versus distances, measured near fields results are marked in black, measured far field results in gray, and modelled results in green.

In addition, modelled and measured results are compared in scatter plots. The distance behind engine 3 is encoded by the colour (magenta: 50 m, red: 100 m, blue: 150 m, cyan: 200 m, green: 250 m). Measured near field results are indicated by a black outline of a symbol and measured far field results by a gray outline. For the winter campaign, January 25 is somewhat exceptional because there were strong cross winds. To distinguish these results from the other days of the winter campaign, the symbols for January 25 are drawn with smaller size.

Figure 68 shows the modelled and measured concentrations of CO_2 (with background subtracted) as a function of distance, Figure 69 the according scatter plots. Figure 70 and Figure 71 show the results for the mass concentration of non-volatile PM, Figure 72 and Figure 73 the results for the number concentration of non-volatile PM.

The higher exit velocities of the enhanced parametrisation in LASPORT 2.4 yield better agreement as compared to LASPORT 2.3, although it is not possible to reproduce the results for the cases with strong cross wind (January 25) as good as for the other cases with more aligned wind directions or lower wind speeds.

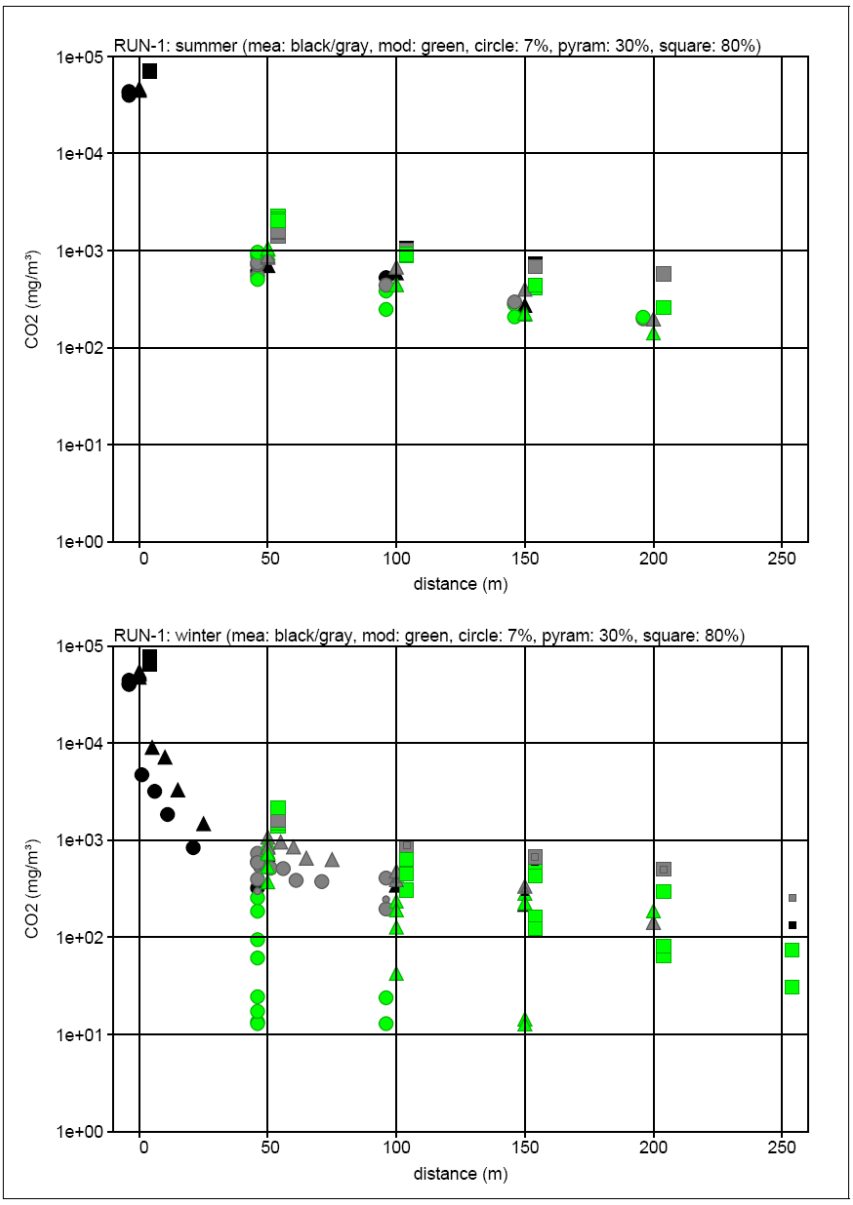

Figure 68: LASPORT 2.4: Measured (black/gray) and modelled (green) CO_2 concentration as a function of distance from engine 3 (background subtracted).

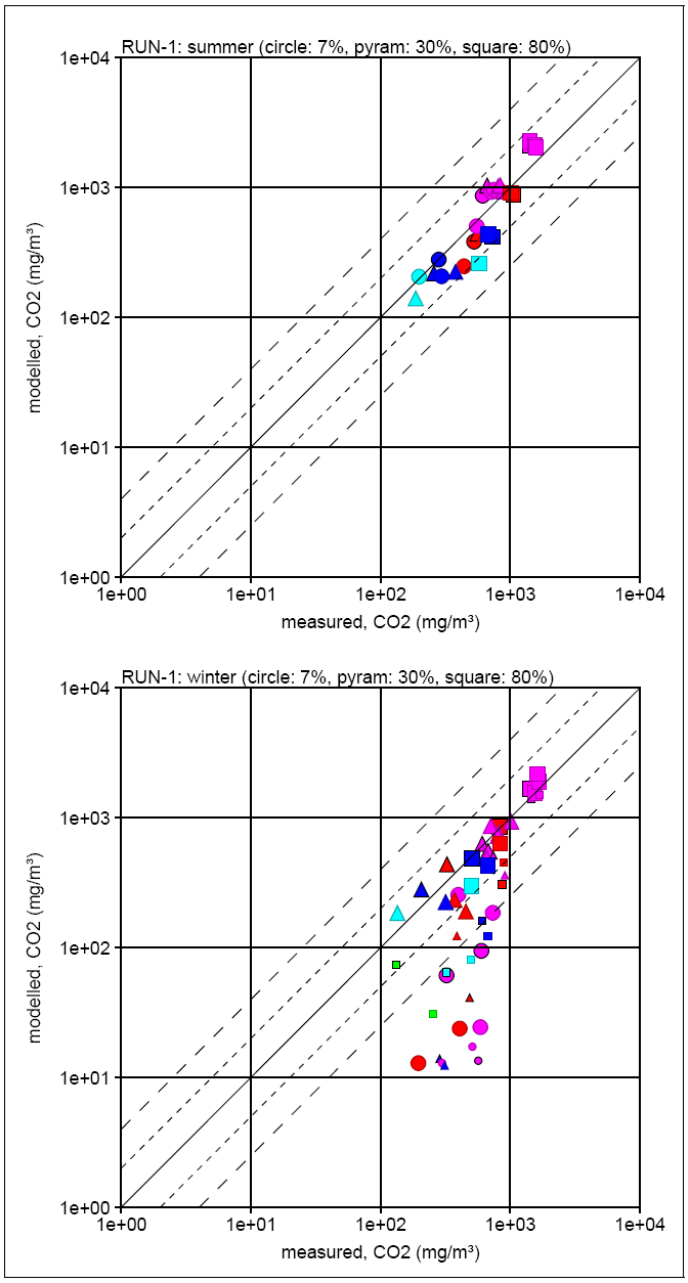

Figure 69: LASPORT 2.4: Measured versus modelled CO_2 concentration (background subtracted). The colours encode the distance to engine 3 (magenta: 50 m, red: 100 m, blue: 150 m, cyan: 200 m, green: 250 m). Small symbols denote January 25 with strong cross winds. The short- and medium-dashed lines denote a factor of 2 and 4 difference, respectively.

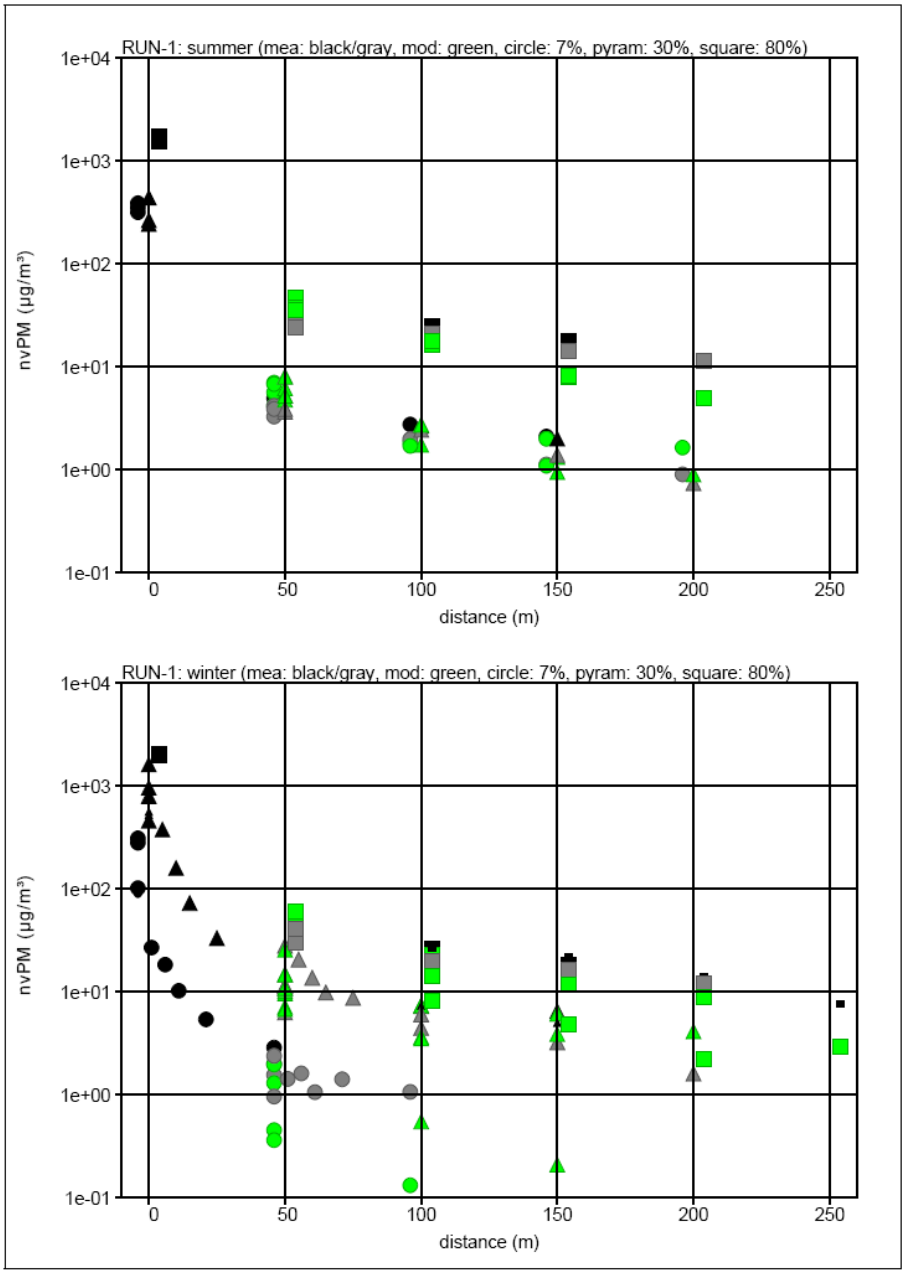

Figure 70: LASPORT 2.4: Measured (black/gray) and modelled (green) non-volatile PM mass concentration as a function of distance from engine 3 (background subtracted).

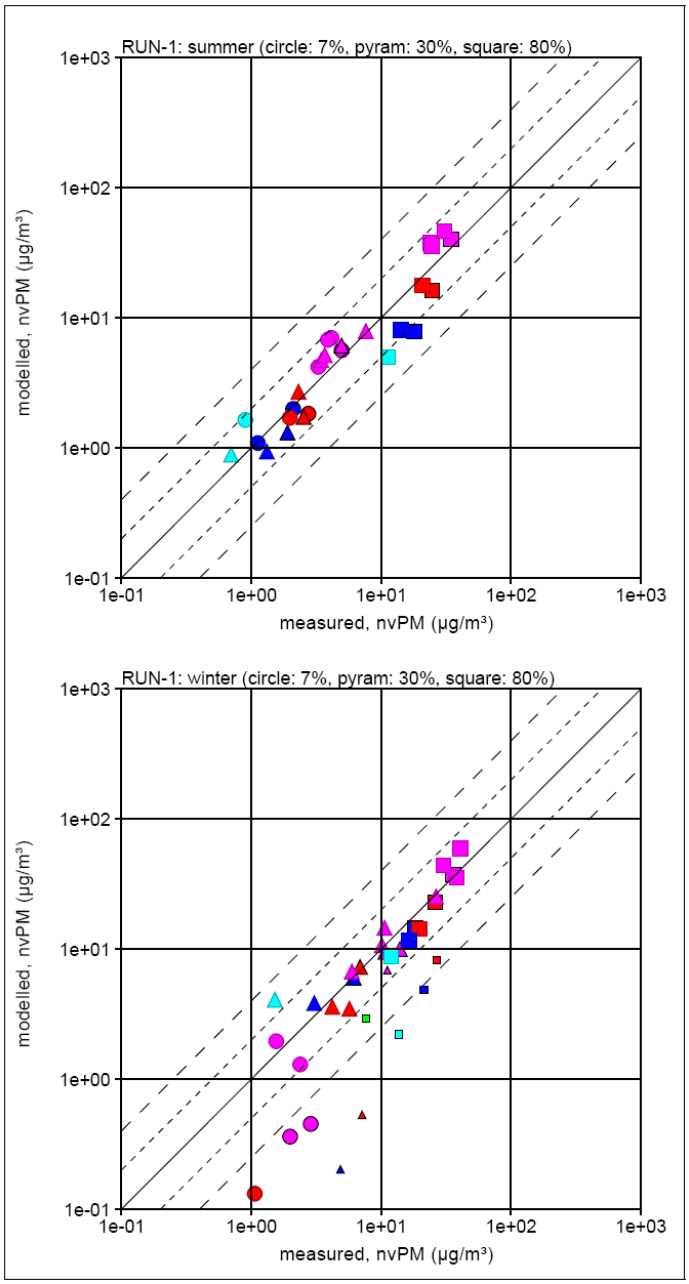

Figure 71: LASPORT 2.4: Measured versus modelled non-volatile PM mass concentration (background subtracted). The colours encode the distance to engine 3 (magenta: 50 m, red: 100 m, blue: 150 m, cyan: 200 m, green: 250 m). Small symbols denote January 25 with strong cross winds. The short- and medium-dashed lines denote a factor of 2 and 4 difference, respectively.

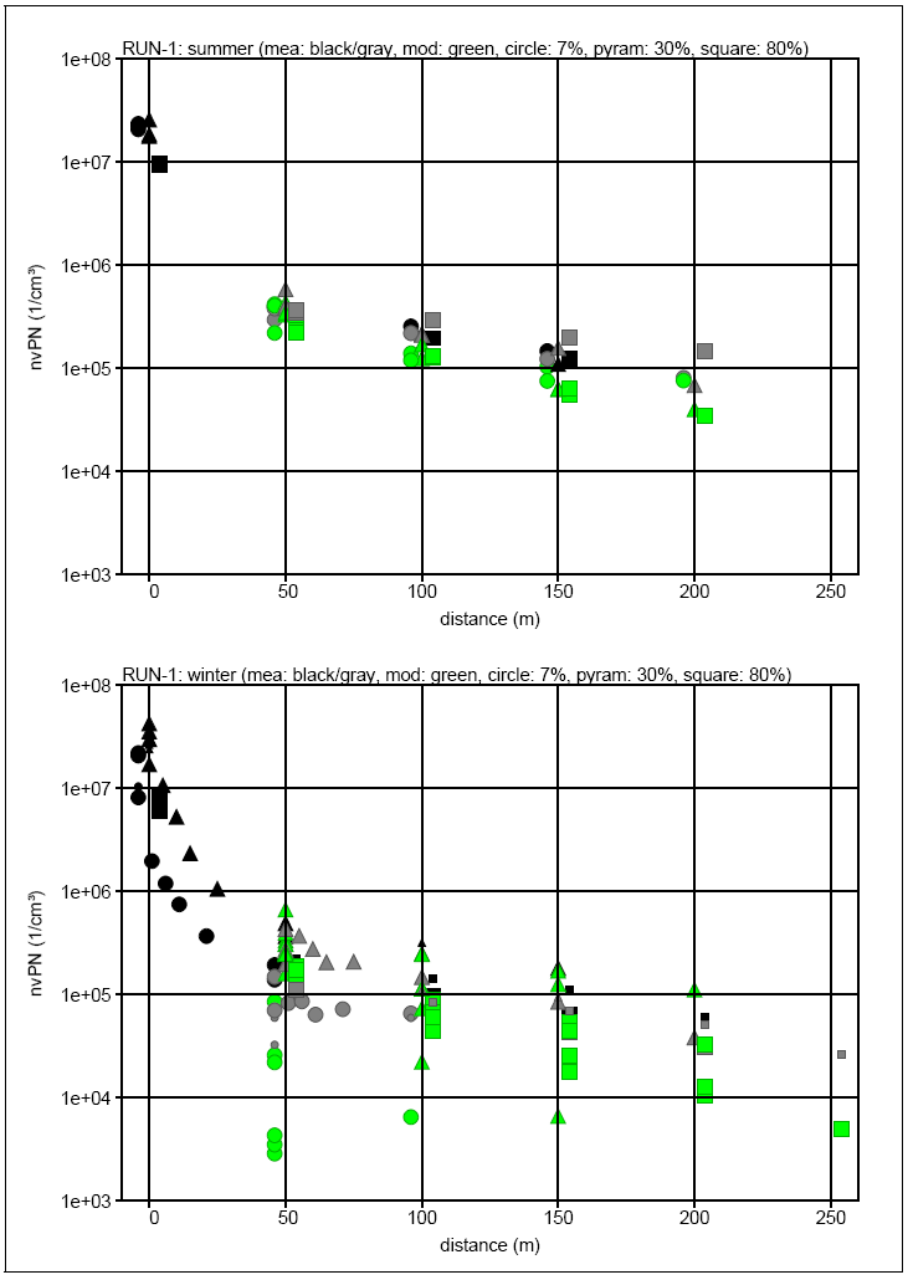

Figure 72: LASPORT 2.4: Measured (black/gray) and modelled (green) non-volatile PM number concentration as a function of distance from engine 3 (background subtracted).

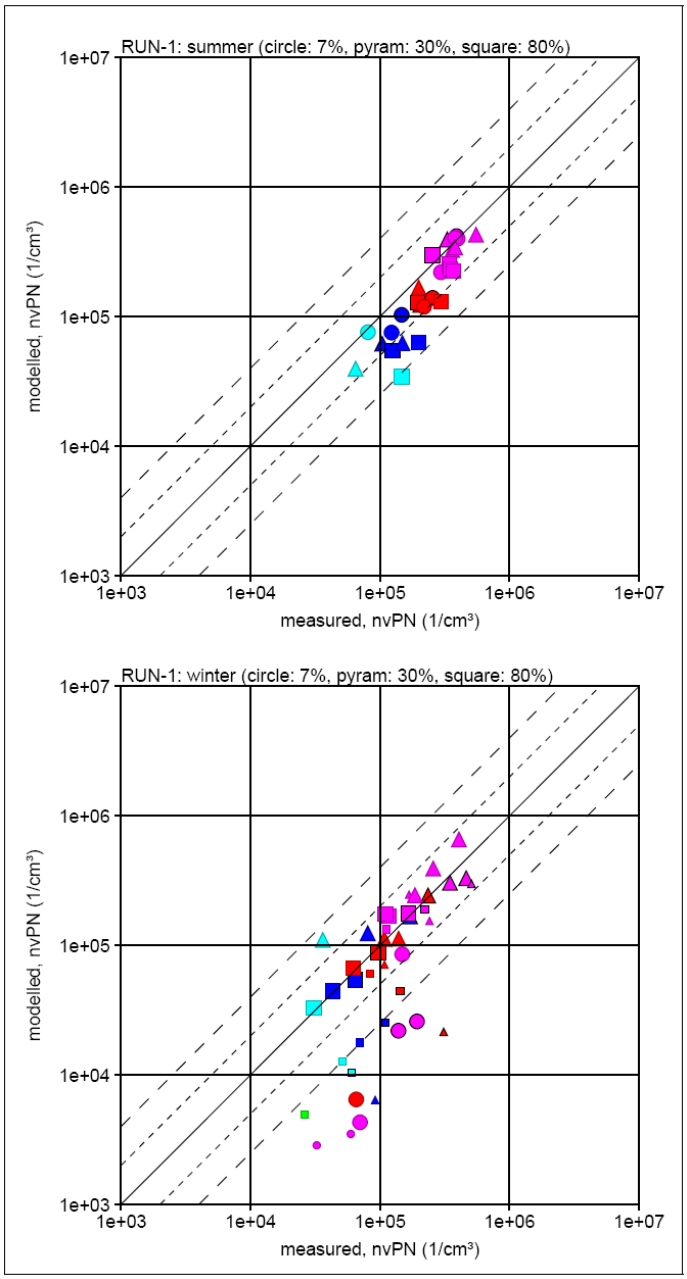

Figure 73: LASPORT 2.4: Measured versus modelled non-volatile PM number concentration (background subtracted). The colours encode the distance to engine 3 (magenta: 50 m, red: 100 m, blue: 150 m, cyan: 200 m, green: 250 m). Small symbols denote January 25 with strong cross winds. The short- and medium-dashed lines denote a factor of 2 and 4 difference, respectively.

6. Comparisons with CEDRE

This section summarizes the comparisons between exhaust plumes modelled by the CFD model CEDRE for a single engine at ground at different thrust settings and according results with LASPORT 2.4.

The case of a single engine at ground was modelled by ONERA with the CFD model CEDRE. The engine body including core and bypass flow was fully resolved and the ground was modelled as a boundary. The engine was of type modern Trent engine with maximum thrust 436.7 kN and bypass ratio 8.1. A homogeneous ambient head wind of 3 m/s, a homogeneous ambient

pressure of 101325 Pa, a homogeneous ambient temperature of 15 °C (implying stable stratification), and a homogeneous ambient CO_2 concentration of 4.e-4 (molar fraction) were assumed. Ambient turbulence was reduced to a negligible value, hence plume dispersion is solely due to exhaust dynamics. Calculation for the thrust settings 7 %, 30 %, 85 %, and 100 % maximum thrust were carried out. Further details can be found elsewhere.

As a result, the quasi-stationary 3-dimensional distributions of temperature, velocity in main wind direction, pressure, and CO_2 concentration with a spatial resolution of 0.5m were provided. Figure 74 to Figure 76 show a graphical visualisation for a horizontal and a vertical cut along the plume centre axis. The distributions show the following key features:

- At the engine plane, the distortion of ambient velocity extends much further than the distortion of temperature and concentration. This can be expected because ambient air is dragged by the engine exhaust due to shear forces ;
- The scalar quantities temperature and concentration show very similar distributions, which can be expected ;
- At 300 m behind the engine, excess velocity is about 1m/s and excess temperature is below 1 °C ;
- Up to the modelled distance of 500 m, the plume shows no clear lift-off from the ground due to buoyancy.

The parametrisations in LASPORT intent to cover the main effects of a moving aircraft at distances of some 100m and more away from the aircraft. This is the typical regime for local air quality modelling at and around an airport, where mainly concentrations over an average of at least one hour with a superposition of many individual aircraft plumes are of interest. Therefore, a comparison of such a LASPORT plume with the CFD results for a single engine is difficult. For this purpose, the default values of the initial horizontal and vertical extent of the plume cross section were reduced to a typical engine diameter of 2.5 m to provide a more meaningful comparison.

In addition, ambient turbulence was reduced to a minimum like it was the case in the CFD runs. Hence, plume dispersion is only due to the initial spread and the effects of parametrised exhaust dynamics. For the emission, a unit emission rate of 1 g/s was used. Figure 77 shows the quasi-stationary LASPORT 2.4 concentration distributions.

Further comparisons between the CEDRE and LASPORT plumes were based on the plume widths of the 2-dimensional concentration cuts. The plume width is defined as the square root of the second central moment of the distribution. Figure 78 shows the spreads at the distances 100 m, 200 m, and 300 m.

LASPORT 2.4 produces similar vertical plume widths as compared to LASPORT 2.3 and smaller horizontal plume widths. This is intended (enhanced parametrisation of exhaust dynamics) to yield a better agreement with the measurements of WP3.

The vertical plume widths of LASPORT 2.4 and CEDRE are similar and LASPORT 2.4 yields horizontally narrower plumes than CEDRE. Using a much larger horizontal plume width in LASPORT would reduce the good agreement with the measurements of WP3.

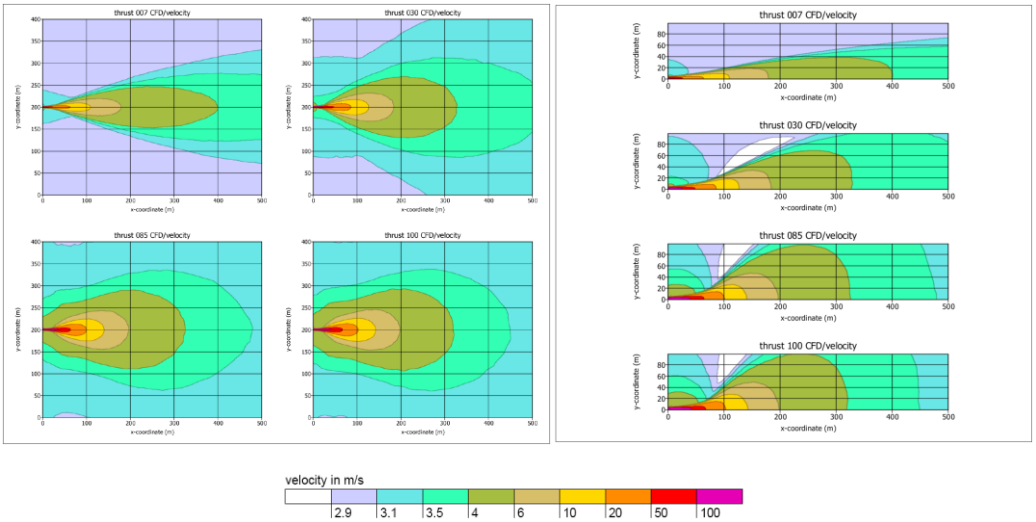

Figure 74: CEDRE, velocity in main wind direction for the thrust settings 7 %, 30 %, 85 %, 100 %. Left: horizontal cuts through the plume axis. Right: vertical cuts through the plume axis.

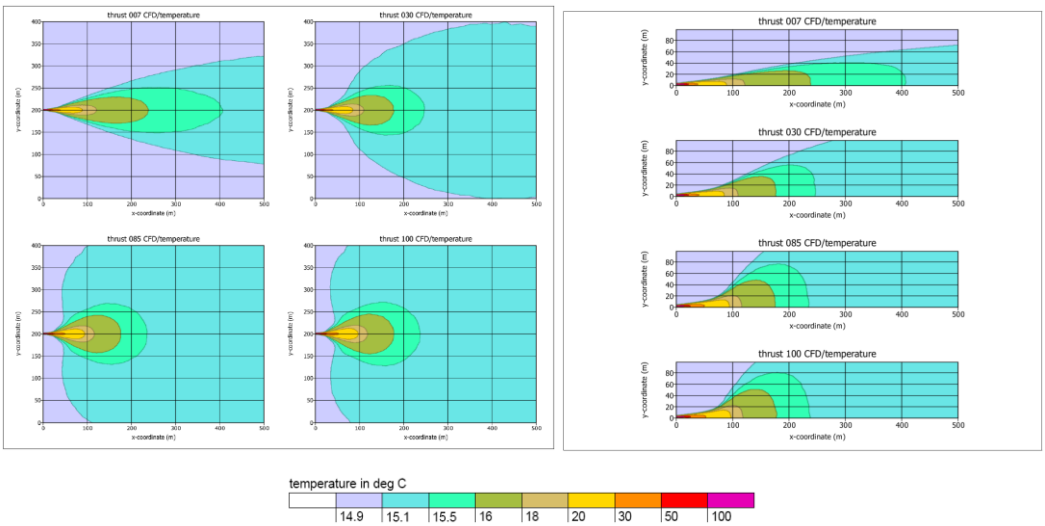

Figure 75: CEDRE, temperature for the thrust settings 7 %, 30 %, 85 %, 100% . Left: horizontal cuts through the plume axis. Right: vertical cuts through the plume axis.

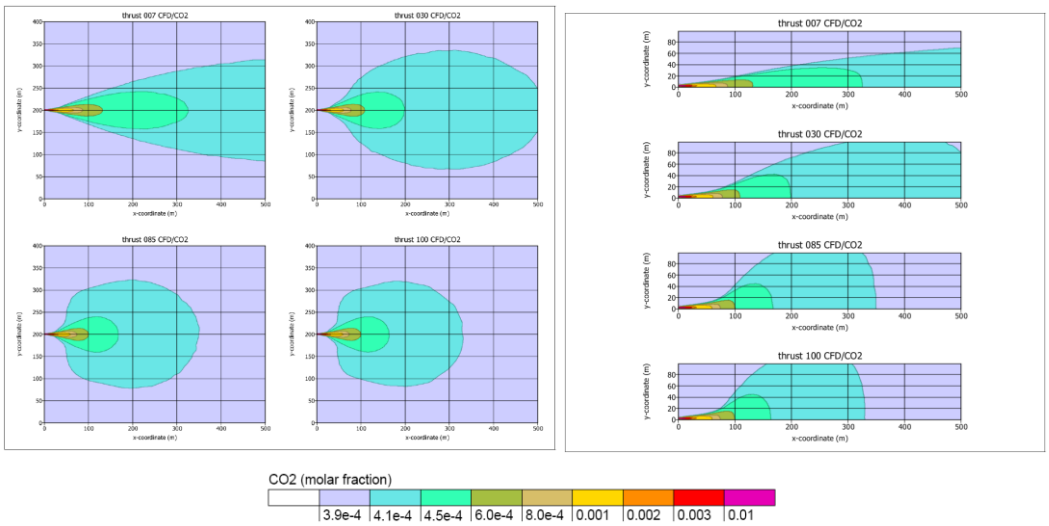

Figure 76: CEDRE, CO_2 concentration for the thrust settings 7 %, 30 %, 85 %, 100 %. Left: horizontal cuts through the plume axis. Right: vertical cuts through the plume axis.

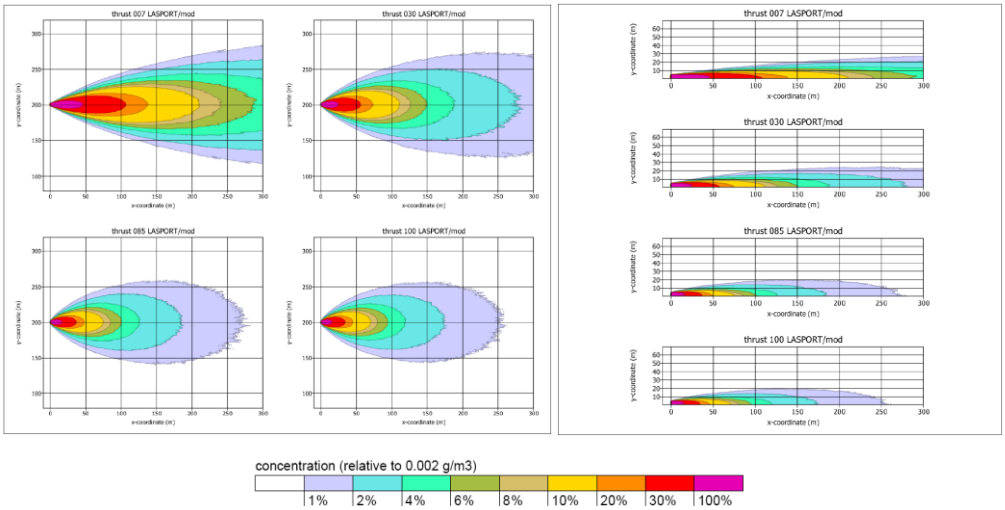

Figure 77: LASPORT 2.4, concentration for the thrust settings 7 %, 30 %, 85 %, 100 %. Left: horizontal cuts through the plume axis. Right: vertical cuts through the plume axis.

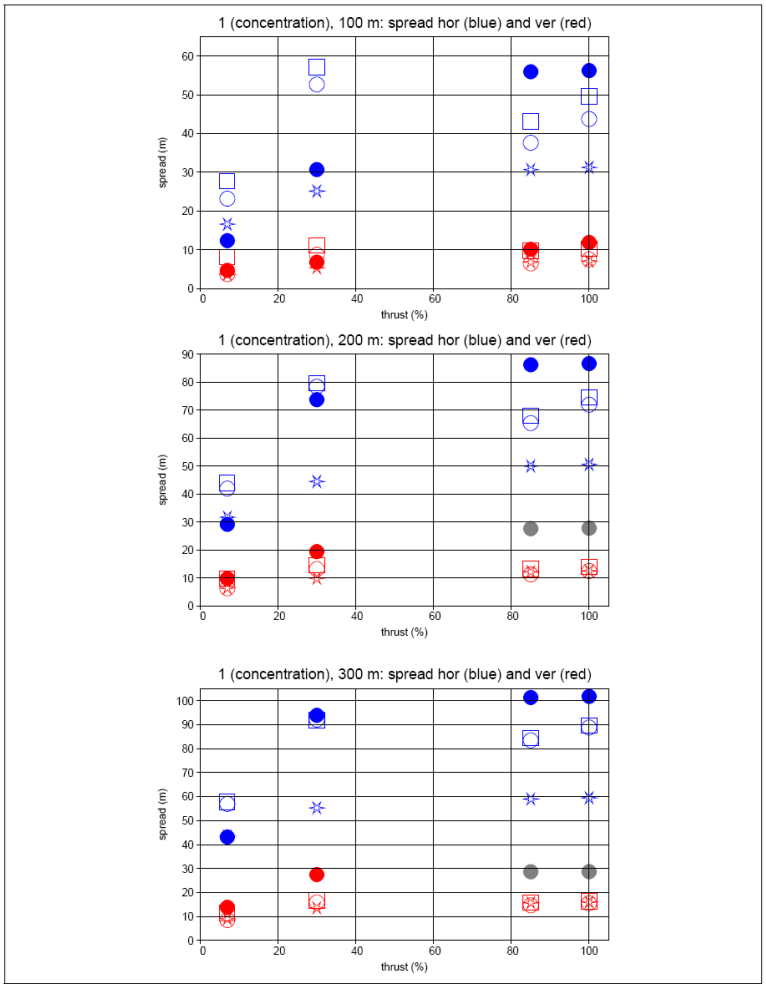

Figure 78: Plume spreads at 100 m, 200 m, and 300 m behind the engine.
Red: vertical spread. Blue: horizontal spread.
Solid circles: CEDRE results.
Gray circles: Vertical spreads of the CEDRE result that are affected by the limited vertical data space.
Open circles: LASPORT 2.3 results with reduced initial spread.
Open squares: LASPORT 2.3 results with default initial spread.
Open stars: LASPORT 2.4 results with reduced initial spread.

7. Conclusions

Simulations of a single modern Trent engine at rest were performed with CEDRE for different thrusts corresponding to the LTO phases. Sensibility studies on ambient temperature showed no impact on the dilution behind the engine and on the plume spread. The comparison with WP3 data set showed a good trend for the dilution factor at 7 % thrust. For higher thrusts, a good tendency is observed at 50 m. However, for larger distances, the model gives a higher dilution than what was observed during the experimental campaign.

The simulations of the complete aircraft during take-off and approach were then performed. The interaction between the wing-tip vortex and the exhaust flow was analysed for both cases and compared with analytical models. The wing tip descent velocity has been calculated from both simulations and used as input for the latest version of LASPORT. The calculations with CEDRE, LASPORT, and the measurements at Zurich Airport revealed consistent key values for the down-shift of exhaust emissions.

The measurements of WP3 allowed detailed comparisons with the model system LASPORT and to improve its parametrisation of exhaust dynamics. It was shown that measured concentrations of CO_2 and mass and number of non-volatile PM could be reproduced by LASPORT quite well for the studied distance range of 50 m to 250 m behind the aircraft for all power settings. Differences were often smaller than a factor of 2 and mostly smaller than a factor of 4. Larger deviations occurred for situations with strong cross winds, here more detailed local meteorological data would be required for modelling.

The comparisons considered only a small subset of the large data set produced in WP3. Further data evaluations and further comparisons with LASPORT will be carried out in the future. The summer data seem well suited to provide a gold standard for near-field model validations (no dominant background emissions, well defined emission rates, high fidelity concentration data, moderate or small wind speeds).

The enhanced parametrisation of exhaust dynamics was cross-checked with other validation data sets (DOAS measurements at Dusseldorf Airport, approach measurements at Zurich Airport).

Comparisons with results of CEDRE for a plume from a single engine in a non-dispersive environment revealed similar vertical plume extents and smaller horizontal plume widths with LASPORT.

The enhanced parametrisation of exhaust dynamics was implemented into version 2.4 and were subsequently applied in the airport dispersion calculations of WP6.

8. References

[1] Refloch A., Courbet A., Murrone A., Villedieu P., Laurent C., Gilbank P., Troyes J., Tesse L., Chaineray G., Dargaud J-B., Quemerais E. and Vuillot F., Cedre Software, Aerospace Lab, no. 2, 2011.

[2] Menter F. R., Two-equation eddy-viscosity turbulence models for engineering applications, *AIAA journal*, vol. 32, no. 8, pp. 1598-1605, 1994.

[3] Menter F. R., Kuntz M. and Langtry R., Ten Years of Industrial Experience with the SST Turbulence Model, *Turbulence, Heat and Mass Transfer* 4, ed: K. Hanjalic, Y. Nagano, and M. Tummers, Begell House, Inc., 2003, pp. 625-632

[4] Kärcher B., Hirschberg M. and Fabian P., Small-scale chemical evolution of aircraft exhaust species at cruising, *J. Geophys. Res*, vol. 101, 1996

[5] Kärcher B., Peter T., Biermann U. and Schumann U., The Initial Composition of Jet Condensation Trails, *J. Atmospheric Sci*., vol. 53, pp. 3066-3083, 1

[6] Chmielarski V., Ghedhaïfi W., Montreuil E. and Loseille A., Comparison between RANS and hybrid RANS/LES simulations of Jet/Vortex interaction, AIAA AVIATION Forum, 17-21 June 2019, Dallas, Texas

[7] Garnier F., Beaudoin C., Woods P. and Louisnard N., Engine emission alteration in the near field of an aircraft, *Atmos. Env. Geophys*. Res. Lett., vol. 31, no. 12, pp. 1767-1781, 1997

[8] Ghedhaïfi W., Bienner A., Megherbi R., Montreuil E., Terrenoire E., Vancassel X. and Loseille A., Influence of atmospheric conditions on contrail formation: 3D simulation versus Schmidt-Appleman criterion. ISABE 2019 -24th ISABE Conference, Sep 2019, Canberra, Australia

[9] Montreuil E., Ghedhaïfi W., Chmielarski V., Vuillot F., Gand F. and Loseille A., Numerical Simulation of contrail formation on the Common Research Model wing/body/engine configuration, AIAA AVIATION Forum June 25-29, 2018, Atlanta, Georgia

[10] Loseille A., Alauzet F., Dervieux A. and Frey P., Achievement of second order mesh convergence for discontinuous flows with adapted unstructured mesh adaptation, in AIAA conference, 2007

[11] Khou J-C., Modélisation des traînées de condensation par interaction entre l'aérodynamique, la cinétique chimique et la microphysique. Mécanique des fluides [physics.class-ph]. Université Pierre et Marie Curie - Paris VI, 2016. Français

[12] Allan B. J., Plane J. M. C., Coe H. and Shillito J., Observations of NO_3 concentration profiles in the troposphere, *Journal of Geophysical Research Atmospheres*, vol. 107, 2002

[13] Chang W., Bhave P., Brown S., Riemer N., Stutz J. and Dabdub D., Heterogeneous Atmospheric Chemistry, Ambient Measurements, and Model Calculations of N2O5: A Review. *Aerosol Science and Technology*. 45, pp. 665-695. 2011

[14] Geyer A., Alicke B., Ackermann R., Martinez M., Harder H., Brune W., di Carlo P., Williams E., Jobson T., Hall S., Shetter R. and Stutz J., Direct observations of daytime NO_3: Implications for urban boundary layer chemistry, *Journal of Geophysical Research Atmospheres*, vol. 108, 2003

[15] Hanke M., Umann B., Uecker J., Arnold F. and Bunz H., Atmospheric measurements of gas-phase HNO_3 and SO_2 using chemical ionization mass spectrometry during the MINATROC field campaign 2000 on Monte Cimone, *Atmos. Chem. Phys*., vol. 3, pp. 417–436, 2003

[16] Lelièvre C. P., Magnani G., Ramaroson R., Gouriou F., Talbaut M., Fréjafon E., Schuermann G., Schaefer K., Cornier I., Emeis S., Vannier F., Paux E., Copalle A. and Perros P., Air quality and engine emission at Paris CDG airport during AIRPUR field campaign. Air Pollution XIV. Proceedings of the Fourteen International Conference on Air Pollution. 2006

[17] Rai R., Rajput M., Agrawal M. and Agrawal S. B., Gaseous air pollutants: a review on current and future trends of emissions and impact on agriculture, *Journal of Scientific Research*, vol. 55, pp. 77-102, 2011

[18] Ehhalt D. H. and Heidt L. E., The Concentration of Molecular H_2 and CH_4 in the Stratosphere, *Pure and Applied Geophysics (PAGEOPH)*, vol. 106-108. 1973

[19] Li M., Karu E., Brenninkmeijer C., Fischer H., Lelieveld J. and Williams J., Tropospheric OH and stratospheric OH and Cl concentrations determined from CH4, CH3Cl, and SF6 measurements, npj *Clim Atmos Sci* 1, 29, 2018

[20] Holland F., Hofzumahaus A., Schafer J., Kraus A. and Patz H-W, Measurements of OH and HO_2 radical concentrations and photolysis frequencies during BERLIOZ, *Journal of Geophysical Research*, vol. 108, n° D4, 8246, 2003

[21] Altshuller A. P., Ambient Air Hydroxyl Radical Concentrations: Measurements and Model Predictions, *JAPCA*, 39:5, pp. 704-708, 1989

[22] Das M. and Aneja V. P., Analysis of Gaseous Hydrogen Peroxide Concentrations in Raleigh, North Carolina, *Air & Waste*, 44:2, pp. 176-183, 1993

[23] Bellin P. and Spengler J. D., Indoor and Outdoor Carbon Monoxide Measurements at an Airport, *Journal of the Air Pollution Control Association*, 30:4, pp 392-394, 198

[24] Xueref-Remy I., Dieudonné E., Vuillemin C., Lopez M., Lac C., Schmidt M., Delmotte M., Chevallier F., Ravetta F., Perrussel O., Ciais P., Bréon F-M., Broquet G., Ramonet M., Gerard

Spain T.and Ampe C., Diurnal, synoptic and seasonal variability of atmospheric CO_2 in Paris megacity area, *Atmos. Chem. Phys*., vol. 18, pp. 3335-3362, 2018

[25] Asoliman I. M., Ehab M., Mahrous A. M., El-Sayed A. F. and Emeara M.S., Performance Analysis of High Bypass Turbofan Engine Trent 1000-A*. 2018

[26] https://en.climate-data.org/europe/spain/castile-la-mancha/ciudad-real-1669/t/november-11/

[27] Rossow VJ., Lift-generated vortex wakes of subsonic transport aircraft. *Prog. Aerosp. Sci*., vol. 35, pp. 507–660, 1999

[28] Gerz T., Holzapfel F. and Darracq D., Commercial aircraft wake vortices. *Prog. Aerosp. Sci*., vol. 38, pp. 181–208, 2002

[29] Jacquin L., Fabre D. and Geoffroy P., The properties of a transport aircraft wake in the extended near field: an experimental study, Presented at AIAA Aerosp. Sci. Meet. Exhib., 39th, Reno, NV, AIAA Pap. 2001-1038, 2001

[30] Paoli R. and Shariff K., Contrail Modeling and Simulation, *Annu. Rev. Fluid Mech*, vol. 48, pp. 393-427, 2016

[31] Schumann U., Schlager H., Arnold F., Baumann R., Haschberger P. and Klemm O., Dilution of aircraft exhaust plumes at cruise altitudes, *Atmospheric Environment*, vol 32, Issue 18, pp 3097-3103, 1998

[32] Fleuti E., Ruf Ch., Maraini S., Ultrafine particle concentrations, Zurich approach runway 14, 2019, Flughafen Zürich AG